Structure and Dynamics of a Turbulent Puff in Pipe Flow(Dissertation_全文)

AUTHOR(S):

Shimizu, Masaki

Structure and Dynamics of a Turbulent Puff in Pipe Flow

Masaki Shimizu

3/2009

Contents

Chapter 1

Introduction

The problem why the flow state in a pipe changes from laminar to turbulence is one of the most fundamental one in fluid dynamics but has puzzled physicists ever since the prominently experience of Reynolds (1883). He measured two kinds of critical parameters. One is the lower critical Reynolds number below which the steady Hagen-Poiseuille flow always recovers against any initial disturbance of arbitrary magnitude but above which a non-trivial flow (other than the Hagen-Poiseuille flow) can be excited and survive for ever from some initial condition. The other one is the upper critical Reynolds number above which the steady Hagen-Poiseuille flow is unstable for some infinitesimal disturbances, implying that unavoidable disturbances prevent us to maintain the Hagen-Poiseuille flow in real experiments. The latter Reynolds number is now commonly believed to be infinitely large on the basis of subsequent laboratory experiments as well as the linear stability analysis (Phenninger 1961, Salwen *et al.* 1980). The prediction of the former one, on the other hand, is difficult and unsolved primarily because it is a nonlinear phenomenon. Experimentally, the lower critical Reynolds number is known to be about 2000.

Reynolds (1883) also found that spatial intermittent turbulence appaers quasi-periodically near critical Reynolds number. This state was examined in detail by Wygnanski *et al.* (1973) and they called the localized-turbulent region puff. A puff can be observed for $2000 < Re_m < 3000$. (Re_m is based on the cross-sectional mean velocity U, the pipe diameter D and the kinematic viscosity ν.) A puff has a sharp upstream bundary which separates the laminar region and turbulent one, and the turbulent level become weak gradually downstream. The length of a puff changes temporally depending on the Reynolds number. For $Re_m \simeq 2200$ the length hardly change and this state of flow is called a 'equilibrium puff' particularly. The length of it is about 20 D and it propagate downstream at the speed near mean velocity U. For $Re_m > 2200$ the length become large temporally. Wygnanski *et al.* (1973) conclued that puffs were generated when large disturbunces were introduced into the inlet. But these are also generated by adding perturbation to fully developed Hagen-Poiseuille flow and the range of Re_m for which puffs can exist depends on the type and strength of the perturbation to used (Darbyshire and Mullin (1995)).

The purpose of our studies is to investigate the structure of puffs and to reveal the dynamics of them using direct numerical simulation (DNS). There have been only limited number of DNS studies of puffs (Leonard and Reynolds (1985), Nikitin (1994), Shan *et al.* (1999), Priymak and Miyazaki (1998,2004), Reuter and Rempfer (2004), and Wills and Kerswell (2007,2008)) and no study which describes about the mechanism to sustain turbulence. The reason of limited

number of DNS works may come from the difficulty to use cylindrical coordinate. Because of the apparent singularity on the central axis in the cylindrical coordinate system, the usual Chebyshev expansion, in which each term is not analytic on the pipe centerline, may deteriorate the accuracy in the radial direction. In the present study we employ Zernike circular polynomials for the radial expansion, which are analytic on the centerline.[Bhatia and Born (1954), Matsushima and Marcus (1995), Verkley (1997)] On the other hand some experimental works have been done but Bandyopadhyay (1986)'s work is the only one which describes the mechanism. He showed that wake-like vortecies were created at the upstream boundary of a puff and a puff is container of these vortecies.

The plan of this paper is as follows. In chapter 2, we describe how the state of flow depends on Reynolds numeber. Adding perturbation to Hagen-Poiseuille flow, puffs are created over a range of Reynolds number. We realize puffs from initial value problem and puff states and fully turbulent state apper cyclically. Chapter 3 is the main part of this paper. We investigate in detail about the equilibrium puff (which does not show the cycle above). The mechanism of self susteining of puffs are described here. At the upstream boundary of a puff large velocity gap exists between the fast laminar flow from upstream region and the slow-streak near the wall which comes from inside of a puff, and a vortex layer which is so large to occur Kelvin-Helmholtz instability is created. A puff susteins itself since disturbunces are created continuously by the roll-ups of the vortex sheet from the instability. This result consistents with the report of Bandyopadhyay (1986) and the roll-ups are investigated quantitatively. In chaper 3, the method of DNS is represented. Spectral method is used for DNS. The peculiarity point here is to use the Zernike circular polinomials which overcome the difficulty to deal with the coordinate singularity at the pole.

Chapter 2

Structure of a turbulent puff in pipe flow

The flow in a circular pipe of radius a driven by a constant and uniform axial force is investigated over a range of Reynolds numbers, including the critical value for laminar-turbulent transition. The Navier-Stokes equation for an incompressible viscous fluid is solved numerically by a spectral method as the initial value problem with the no-slip boundary condition on the pipe wall and periodic boundary conditions with period $16\pi a$ in the axial direction. The initial condition is given by the Hagen-Poiseuille flow (corresponding to the external force) superimposed with perturbations of finite amplitude. The long-term behaviour of the flow is qualitatively different depending on the Reynolds number $Re = Ua/\nu$, where U is the centerline velocity of the above Hagen-Poiseuille flow and ν is the kinematic viscosity of the fluid. For intermediate Reynolds numbers ($3300 \leq Re \leq 4000$) we find a locally turbulent region, called a "puff", which is advected downstream with velocity close to the mean axial velocity. The velocity fluctuations in the puff change quasi-periodically in time. The upstream boundary, called the "trailing edge" of the puff, sharply divides the laminar and turbulent regions. The mean shape of the trailing edge is determined by the least-squares method using the cross-axial velocity fluctuations in the puff. This will be useful as a reference when the flow structure and/or generation mechanism of a turbulent puff are analysed.

2.1 Introduction

The study of circular pipe flows has a long history. Osborne Reynolds (1883) was the first to discover experimentally that the flow state changes qualitatively from laminar to turbulent at a non-dimensional physical quantity, which is now called the Reynolds number (see section 2.1 for definition) after him, of about 2000. His discovery of the transition of flow state triggered subsequent research into flow instability. Linear stability analysis has been applied to obtain theoretically the critical Reynolds number for many basic flows, including the plane Poiseuille flow and duct flows with various cross-sections. Ironically, however, it turned out that steady fully developed axisymmetric flow in a tube is linearly stable for all Reynolds numbers. Therefore the above critical value cannot be explained by linear stability theory. Correspondingly, subsequent corroborations of the Reynolds experiment showed that the transition of flow state in pipe flow may not occur even at much larger Reynolds numbers up to 10^5.[Pfenninger (1961)]

There are at least two different factors to consider for the explanation of a critical Reynolds number 2000. One is the deviation of the base flow from the steady fully developed Hagen-Poiseuille flow. The velocity profile near the entrance of a circular pipe is much different from the steady Hagen-Poiseuille flow which is established only far downstream. A stability analysis of the inlet flow predicts a finite value of the critical Reynolds number.[Tatsumi (1952)] Another factor is the finiteness of the disturbance magnitude. Instead of the *linear* critical Reynolds number which is the minimal value of the Reynolds number for which the steady flow can be unstable for arbitrary infinitesimal disturbances, we consider the *nonlinear* critical Reynolds number below which the steady laminar flow will be eventually recovered, however large the initial disturbance. There is no systematic method to determine the nonlinear critical Reynolds number because the principle of superposition does not hold as linear stability analysis. The lower limit of the nonlinear critical Reynolds number 81.49 obtained by a bound theory[Joseph and Carmi (1969)] is much smaller than the experimental value of 2000. One practical method to estimate the nonlinear critical Reynolds number is to find a non-trivial solution (i.e., different from the Hagen-Poiseuille flow) at a smallest possible Reynolds number. The travelling-wave solutions in pipe flow[Faisst and Eckhardt (2003), Wedin and Kerswell (2004)] , and the travelling-wave solutions and unstable periodic flows discovered in plane Couette flow[Nagata (1997), Kawahara and Kida (2001), Viswanath(2007)] are possible candidates. Around the critical Reynolds number there appears an axially localized turbulent state, called a "puff", which moves downstream with velocity close to the mean axial velocity. This localized coherent structure may be a good candidate of the unstable periodic flow which may give the nonlinear critical Reynolds number. To realize a puff as a non-trivial solution at the smallest possible Reynolds number is one of the primary motivations of the present study.

To date there have been fewer numerical studies of pipe flow than of channel flow, although the contrary is true for experimental studies. The reason can be primarily attributed to the geometry (the cylindrical coordinate system) required to describe the flow in a circular pipe. Because of the apparent singularity on the central axis in the cylindrical coordinate system, the usual Chebyshev expansion, in which each term is not analytic on the pipe centerline, may deteriorate the accuracy in the radial direction. In the present study we employ Zernike circular polynomials for the radial expansion, which are analytic on the centerline.[Bhatia and Born (1954), Matsushima and Marcus (1995), Verkley (1997)]

In their direct numerical simulation (DNS) of the flow with a constant axial velocity, Shan *et al.* (1999) realized a turbulent puff at $Re_m = 2200$ by creating suction and blowing in radial velocity at the pipe wall for an initial period of time. Here $Re_m = 2a\langle u_z\rangle_{r\theta}/\nu$ is the Reynolds number based on the mean axial velocity $\langle u_z\rangle_{r\theta}$ (independent of z because of incompressibility) averaged over the cross-sectional (r, θ)-plane, the pipe diameter $2a$ and the kinematic viscosity ν of fluid. Priymak and Miyazaki (2004) realized by DNS an equilibrium puff (the axial length of the puff being invariant in time) for $2200 \leq Re_m \leq 2350$ by taking a developed turbulent state as the initial condition. They obtained a mean axial velocity profile that compared well with the experimental results of Wygnanski *et al.* (1975) Willis and Kerswell (2007) observed an equilibrium puff at $Re_m = 1900$ in DNS by imposing a local body force for a finite time. Unlike these previous works we produce the turbulent puff by starting with an appropriate initial condition.

This paper is organized as follows. The basic equations and our DNS method, including the numerical scheme and the initial condition, are introduced in §2. The results of DNS for

various Reynolds numbers are described in §3 with special attention to the turbulent puff. A puff is generated by adding a sufficiently large initial perturbation to the Hagen-Poiseuille flow. The puff is not in statistical equilibrium, but repeats its generation and destruction process. The shape of the trailing edge of the puff is defined and the mean flow structure is obtained relative to the trailing edge. Concluding remarks are given in §4.

2.2 Formulation

2.2.1 Basic equations

We consider the flow of an incompressible viscous fluid driven by a constant external body force $f\widehat{z}$ (where $\widehat{\ }$ denotes the unit vector) in a straight circular pipe of radius a. The cylindrical polar coordinate system (r, θ, z) is introduced to describe the velocity field $\boldsymbol{u}(r, \theta, z; t)$, with the z axis taken on the pipe centerline, r the radial coordinate and θ the azimuthal angle. We apply no-slip on the stationary pipe wall and periodic boundary conditions in velocity and pressure in the axial (z) direction with period aL.

Then the governing equations of the flow are given by the Navier-Stokes equation

$$\frac{\partial \boldsymbol{u}}{\partial t} + (\boldsymbol{u} \cdot \nabla)\boldsymbol{u} = -\nabla p + \frac{1}{Re}\nabla^2 \boldsymbol{u} + \frac{4}{Re}\widehat{z}, \tag{2.1}$$

the continuity equation

$$\nabla \cdot \boldsymbol{u} = 0, \tag{2.2}$$

together with the no-slip boundary condition

$$\boldsymbol{u}(1, \theta, z; t) = 0, \tag{2.3}$$

and the periodic boundary conditions

$$\boldsymbol{u}(r, \theta, z + L; t) = \boldsymbol{u}(r, \theta, z; t). \tag{2.4}$$

Here, all the physical quantities have been non-dimensionalized using a for length, $U = fa^2/4\nu$ for velocity (the centerline velocity of the Hagen-Poiseuille flow driven by $f\widehat{z}$), ρU^2 for the pressure, ρ being the density of fluid and ν the kinematic viscosity. One important non-dimensional control parameter in this system is the Reynolds number $Re \equiv Ua/\nu$ $(= fa^3/4\nu^2)$. The last term on the right-hand side of (2.1) is the body force.

The curl of (2.1) leads to the vorticity equation

$$\frac{\partial \omega}{\partial t} = \nabla \times (\boldsymbol{u} \times \omega) + \frac{1}{Re}\nabla^2 \omega, \tag{2.5}$$

where $\omega \equiv \nabla \times \boldsymbol{u}$ is the vorticity field.

We express the solenoidal field $\boldsymbol{u}$ as

$$\boldsymbol{u} = \nabla \times (\psi\widehat{z}) + \nabla \times (\nabla \times (\phi\widehat{z})), \tag{2.6}$$

where ψ and ϕ are toroidal and poloidal functions, respectively. These scalar functions have "gauge freedom". That is, the addition of an arbitrary function of z to ψ and/or a cross-axial

harmonic function (i.e. a null-mode of $\nabla_\perp^2 \equiv \nabla^2 - \partial^2/\partial z^2$) to ϕ does not change the velocity field defined by (2.6). We can uniquely define the scalar functions by imposing these boundary conditions:

$$\int_0^{2\pi} \psi|_{r=1}\, \mathrm{d}\theta = 0, \tag{2.7a}$$

$$\phi|_{r=1} = 0. \tag{2.7b}$$

The no-slip boundary conditions on the pipe wall (2.3) implies:

$$\left.\frac{\partial \psi}{\partial \theta}\right|_{r=1} + \left. r\frac{\partial^2 \phi}{\partial r \partial z}\right|_{r=1} = 0, \tag{2.8a}$$

$$\left. r\frac{\partial \psi}{\partial r}\right|_{r=1} = 0, \tag{2.8b}$$

$$\left.\left(r\frac{\partial}{\partial r}\right)^2 \phi\right|_{r=1} = 0, \tag{2.8c}$$

where (2.7b) has been used in the derivation of (2.8b) and (2.8c). The periodic condition in the axial direction (2.4) implies:

$$\psi(\boldsymbol{r} + L\widehat{z}; t) = \psi(\boldsymbol{r}; t), \tag{2.9a}$$

$$\phi(\boldsymbol{r} + L\widehat{z}; t) = \phi(\boldsymbol{r}; t). \tag{2.9b}$$

The governing equation for ψ is derived taking the axial component of the vorticity equation (2.5):

$$\nabla_\perp^2 \left(\nabla^2 - Re\frac{\partial}{\partial t}\right)\psi = Re(\nabla \times \boldsymbol{N}) \cdot \widehat{z}, \tag{2.10}$$

where $\boldsymbol{N} = \boldsymbol{u} \times \boldsymbol{\omega}$ is the nonlinear term. Similarly, by taking the axial component of the curl of (2.5), we obtain the governing equation for ϕ as

$$\nabla_\perp^2 \left(\nabla^2 - Re\frac{\partial}{\partial t}\right)\nabla^2 \phi = -Re\,(\nabla \times (\nabla \times \boldsymbol{N})) \cdot \widehat{z}. \tag{2.11}$$

Furthermore, the radial component of (2.5) on the pipe wall, by using (2.8a)–(2.8c), yields

$$\left. r\frac{\partial^2}{\partial r \partial z}\nabla_\perp^2 \psi\right|_{r=1} - \frac{\partial}{\partial \theta}\left(r\frac{\partial}{\partial r}\right)^2 \left.\nabla_\perp^2 \phi\right|_{r=1} = 0. \tag{2.12}$$

With this additional boundary condition, the governing equations (2.10) and (2.11) for the scalar functions are equivalent to the vorticity equation (2.5).[Marqués (1990)]

The equation for the mean velocity is obtained by integrating the axial component of Navier-Stokes equation (2.1) over the periodic domain ($0 \le r \le 1, 0 \le \theta \le 2\pi, 0 \le z \le L$) as

$$-\frac{1}{\pi L}\int_0^L \int_0^{2\pi} \frac{\partial}{\partial t}\left(r\frac{\partial}{\partial r}\right)\phi|_{r=1}\mathrm{d}\theta\mathrm{d}z = -\frac{1}{\pi LRe}\int_0^L \int_0^{2\pi} \left(r\frac{\partial}{\partial r}\right)^3 \phi|_{r=1}\mathrm{d}\theta\mathrm{d}z + \frac{4}{Re}. \tag{2.13}$$

Thus we have rewritten the system of governing equations (2.1)–(2.4) for the velocity and pressure fields into the equivalent ones (2.7)–(2.13) for the two scalar functions ψ and ϕ.

2.2.2 Numerical Scheme

We solve the set of evolution equations (2.7)–(2.13) for the toroidal and poloidal functions derived in the preceding section numerically by a spectral method.

Since the scalar functions, ψ and ϕ, are periodic in the azimuthal and axial coordinates, it is natural to use the Fourier basis for these two variables. In the radial coordinate we employ the Zernike polynomials $\Phi_n^m(r)$ for the expansion basis to satisfy the so-called pole condition at the origin $r = 0$.[Bhatia and Born (1954), Matsushima and Marcus (1995), Verkley (1997)] We approximate the scalar functions by a finite series expansion as

$$\begin{aligned}\begin{pmatrix}\psi(r,\theta,z;t)\\ \phi(r,\theta,z;t)\end{pmatrix} &= \sum_{k=-K}^{K}\sum_{m=-M}^{M}\begin{pmatrix}\widetilde{\psi}^{mk}(r;t)\\ \widetilde{\phi}^{mk}(r;t)\end{pmatrix}\exp[\mathrm{i}(m\theta+(2\pi/L)kz)]\\ &= \sum_{k=-K}^{K}\sum_{m=-M}^{M}\sum_{\substack{n=|m|\\ n+m=\text{even}}}^{N}\begin{pmatrix}\widehat{\psi}_n^{mk}(t)\\ \widehat{\phi}_n^{mk}(t)\end{pmatrix}\Phi_n^m(r)\exp[\mathrm{i}(m\theta+(2\pi/L)kz)],\end{aligned} \tag{2.14}$$

where K, M and N ($\geq M$) are positive integers. $\Phi_n^m(r)$ is a polynomial composed of $r^{|m|}, r^{|m|+2}, \cdots, r^n$ terms and satisfies orthogonality relation,

$$\int_0^1 \Phi_n^m(r)\Phi_{n'}^m(r)r\mathrm{d}r = \delta_{nn'}. \tag{2.15}$$

Note that the reality conditions of ψ and ϕ require $\widetilde{\psi}^{mk} = (\widetilde{\psi}^{-m-k})^*$ and $\widetilde{\phi}^{mk} = (\widetilde{\phi}^{-m-k})^*$, where $*$ denotes the complex conjugate. We take $(N, M, K) = (100, 21, 170)$. The grid spacing ($(\Delta r)_n$, $n = 0, 1, \cdots, \frac{1}{2}N + 1$), or the Gauss-Radau quadrature points, in the radial direction is non-uniform and is a decreasing function of r, where $(\Delta r)_0 = 0.023$ at the pipe centerline and $(\Delta r)_{\frac{1}{2}N+1} = 0.0007$ at the pipe wall. The smallest resolved wavelengths in the azimuthal direction are $2\pi(\Delta r)_0/M = 0.007$ at the pipe centerline and $2\pi/M = 0.30$ at the pipe wall. The smallest resolved wavelength in the axial direction is uniform, taking $L/K = 0.30$. With these choices the expansion coefficients of the scalar functions drop by at least 2 orders of magnitude with mode order n, m or k. These resolutions are sufficient for the present purpose.

The evolution equations for the expansion coefficients, $\widehat{\psi}_n^{mk}(t)$ and $\widehat{\phi}_n^{mk}(t)$, are derived by multiplying (2.10) and (2.11) by $\Phi_n^m(r)\exp[-\mathrm{i}(m\theta+(2\pi/L)kz)]$ and integrating over the periodic domain. For time integration we employ the second-order Adams-Bashforth scheme for the nonlinear term and the Crank-Nicolson scheme for the viscous term. Then we obtain a set of simultaneous linear equations for $\widehat{\psi}_n^{mk}(t)$ and $\widehat{\phi}_n^{mk}(t)$ with source terms given by those at previous two time steps $t - \Delta t$ and $t - 2\Delta t$, where Δt is the time increment. We take $\Delta t = 0.005$. We derive five more linear equations for $\widehat{\psi}_n^{mk}(t)$ and $\widehat{\phi}_n^{mk}(t)$, in the same way as above, from the boundary conditions (2.8a)–(2.8c) and (2.12) and the evolution equation for the mean axial velocity (2.13). The complete set of simultaneous equations is solved by the τ method to update $\widehat{\psi}_n^{mk}(t)$ and $\widehat{\phi}_n^{mk}(t)$. The detailed numerical scheme will be published elsewhere.

2.2.3 Initial conditions

Because the flow is driven by a constant force $4/Re$, the Hagen-Poiseuille flow $\boldsymbol{u} = (1 - r^2)\widehat{\boldsymbol{z}}$ is established as the steady laminar state. Small amplitude disturbances will decay since the

Hagen-Poiseuille flow is linearly stable at all Reynolds numbers. The choices of amplitude and shape of the disturbance are essential to obtain a non-trivial flow state. For simplicity we assume disturbances composed of the minimum number of modes required to develop turbulent states. Since the disturbances must be three dimensional, we choose two primary modes in the azimuthal and axial directions with comparable length scale, i.e. $(m,k) = (1,0)$ and $(0,8)$. Note that the wave length in the axial direction L/k with $L = 16\pi$ and $k = 8$ coincides with the pipe circumference 2π. In addition we impose a minor mode with $(m,k) = (0,1)$ and small magnitude to destroy undesired periodicity shorter than the system size L in the axial direction. Also the complex conjugates of these modes are applied to $(m,k) = (-1,0), (0,-8)$ and $(0,-1)$.

Each mode satisfies the relevant boundary conditions with a minimum number of Zernike polynomials of lowest order. For the $(m,k) = (1,0)$ mode we have $\psi = D\psi = 0$ ($D \equiv r\partial/\partial r$) from (2.8a) and (2.8b), and $\phi = D^2\phi = D^2(D^2/r^2 - 1/r^2)\phi = 0$ from (2.7b), (2.8c) and (2.12). For $(m,k) = (0,8)$ and $(m,k) = (0,1)$ we have $\psi = D\psi = 0$ from (2.7a) and (2.8b), and $\phi = D\phi = D^2\phi = 0$ from (2.7b), (2.8a) and (2.8c). Then the functional forms of these modes are given by

$$\widetilde{\psi}^{10}(r) = A^{10}(1-r^2)^2 r, \qquad \widetilde{\phi}^{10}(r) = B^{10}(1-r^2)(1-5r^2/7+r^4/7)r, \qquad (16a,b)$$

$$\widetilde{\psi}^{08}(r) = A^{08}(1-r^2)^2, \qquad \widetilde{\phi}^{08}(r) = B^{08}(1-r^2)^3, \qquad (16c,d)$$

$$\widetilde{\psi}^{01}(r) = A^{01}(1-r^2)^2, \qquad \widetilde{\phi}^{01}(r) = B^{01}(1-r^2)^3. \qquad (16e,f)$$

Although the amplitudes of the disturbances are complex in general, we apply real disturbances assuming that the phase may not be important. We take $A^{10} = B^{10} = A^{08} = B^{08} = 0.01$ for primary modes $(1,0)$ and $(0,8)$, and $A^{01} = B^{01} = 0.0001$ for minor mode $(0,1)$. This assumed disturbance is set to be about 20% in magnitude of u_z at the pipe centerline compared with the reference Hagen-Poiseuille flow composed of a single mode $\widetilde{\phi}^{00}(r) = (1-r^2)(3-r^2)/16$. The above amplitude of the primary modes 0.01 was chosen observing that there was a transition to turbulence at 0.008 but not at 0.007 for $Re = 4000$.

2.3 Flow Characteristics in a Pipe

2.3.1 Reynolds number dependence

We present here the characteristics of pipe flow obtained by the numerical method described in the preceding section. The initial condition as well as the numerical parameters except for the Reynolds number are common for all the cases.

The global behaviour of the flow state, monitored by the temporal variations of the mean axial velocity $\langle u_z \rangle_{r\theta}(t)$, is shown in Fig. 2.1 for several Reynolds numbers. The mean velocity is 0.5 for Hagen-Poiseuille flow. Next to each curve we show the Reynolds number Re based on the external force. In addition, to those curves that do not return to the Hagen-Poiseuille flow we show the Reynolds number $Re_{\rm m}(t)$ ($= 2\langle u_z \rangle_{r\theta}(t) Re$) at time $t = 2000$ in brackets (see §1 for definition of $Re_{\rm m}$). It is seen that the flow states may be classified into three groups: (i) For smaller Reynolds numbers $Re < 3000$ the initial perturbation initially grows but then decays to the steady Hagen-Poiseuille flow; (ii) For larger Reynolds numbers $Re > 6000$, on the other hand, the mean velocity approaches constant values different from that for the Hagen-Poiseuille

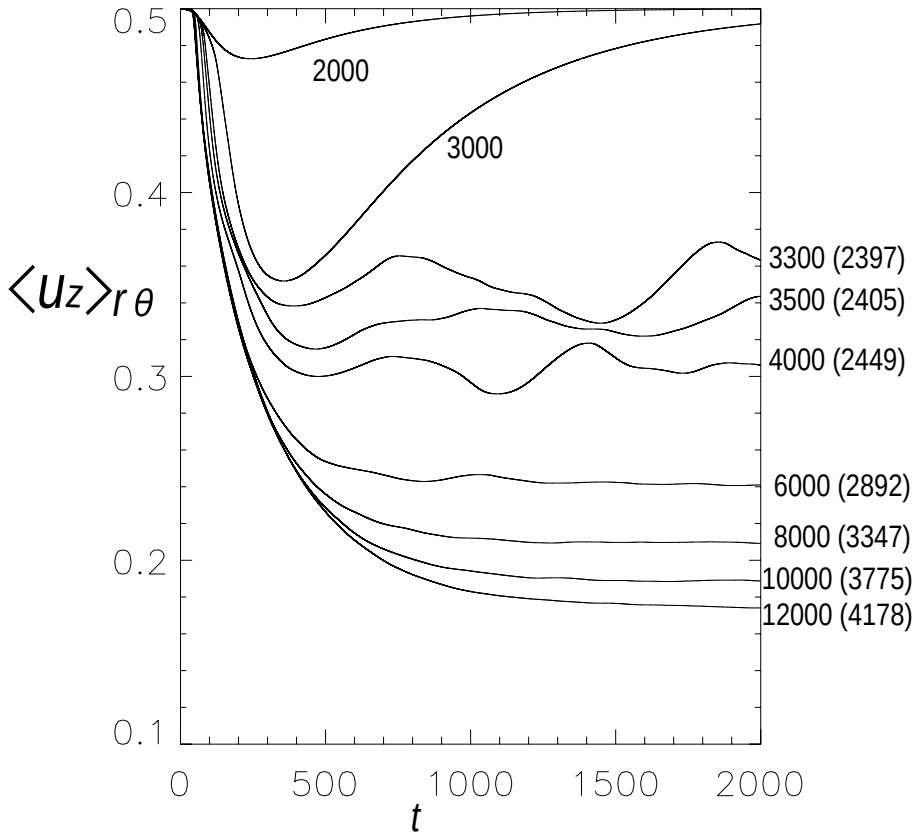

Figure 2.1: Time variation of mean axial velocity $\langle u_z \rangle_{r\theta}(t)$. The numbers next to each curve indicate the Reynolds numbers Re and Re_m, the latter being in the brackets.

flow. Although the instantaneous flow structures vary violently in space and time (figures omitted), the variations of $\langle u_z \rangle_{r\theta}(t)$ from their time averages are below 1% in magnitude at large times. Thus these turbulent flows seem to be approximately in a statistically equilibrium state; (iii) For intermediate Reynolds numbers, Re = 3300, 3500 and 4000, the mean velocity changes significantly in time (nearly 10% in amplitude), in contrast to the above two cases. The mean velocity changes roughly periodically in time. As we shall discuss in the next subsection, a localized turbulent state called a "puff" is observed at these Reynolds numbers. As reported by Rubin *et al.* (1980), and more recently by Hof *et al.* (2006), puffs are observed experimentally when sufficiently large disturbances are applied to the Hagen-Poiseuille base flow. Here we show puffs by DNS at these intermediate Reynolds numbers. Puffs are not in a statistical equilibrium state, and the generation and destruction of puffs continuously repeat.

2.3.2 Appearance of turbulent puffs

In this subsection we focus our attention to the turbulent puffs observed at intermediate Reynolds numbers. We take the case of Re = 3500 as a typical example. In Fig. 2.2(c), we show the temporal variation of the mean axial velocity $\langle u_z \rangle_{r\theta}(t)$ for Re = 3500 extended in time

beyond the corresponding result in Fig. 2.1. It is seen that the mean axial velocity changes in time with large amplitude. The magnitude of variation is as large as 10% of the mean value, which is in contrast with the steady case (at smaller Reynolds numbers) and the developed turbulent case (at larger Reynolds numbers), where the fluctuations are much smaller. The oscillation is not regular and appears to have a characteristic period about 1000 time units. As will be seen below, the mean velocity takes larger values when a puff is generated.

In order to see the spatial inhomogeneity of the velocity fluctuations we show in Fig. 2.2(a) the axial velocity field on the pipe centerline, where time increases vertically every 10 time units. The abscissa covers the computational domain length, $L = 16\pi$ (≈ 50.3). The velocity magnitude is represented by gray scale, with light gray for higher speeds and dark gray for lower speeds. The straight lines of equal contrast with upward slope from left to right imply that some structures in the velocity field move downstream with a nearly constant speed. Since the system is periodic in the axial coordinate, a structure which exits from the right end reenters from the left. Such passings take place many times during the period presented. By comparing (a) and (c) we see that the mean axial velocity takes larger or smaller values as structures appear or disappear.

The structure of the velocity fluctuation can be seen more clearly in a frame moving with the structure. In Fig. 2.2(b), we replot each instantaneous velocity field in Fig. 2.2(a) by shifting it downstream with a constant velocity so that the sharp contrast is quasi-stationary. The convection velocity was determined by trial and error to be 0.325. We see in this figure several interesting characteristics of the flow. First, high speed regions appear and disappear repeatedly with a period of about 1000 time units. Second, the axial velocity increases gradually downstream over most of the high speed region and decreases abruptly at its downstream end. Third, the position of a sharp jump changes very little in this moving frame, implying that it moves downstream with nearly constant speed 0.325 in the fixed frame. Fourth, another group of straight lines of constant contrast with upward slope from left to right is observed indicating downstream convection with a nearly constant speed about 0.2–0.3. As will be seen below, the velocity fluctuations are larger in darker regions just downstream of the sharp jump of the axial velocity. This region is called the turbulent puff, and the jump at the upstream end of puff is called the trailing edge. The velocity fluctuation in the puff weakens in magnitude gradually toward downstream so that the puff boundary in the downstream side, called the leading edge, is not clear.

Now we examine the flow structure in more detail. In Fig. 2.3, we show a two-dimensional cross-section of the axial velocity during the period between 3800 and 5600 which includes one cycle of a strong variation in the velocity (see the second gray band from the bottom in Fig. 2.2(c)). Here we plot, in a plane of azimuthal angles $\theta = 0$ and π passing through the pipe centerline $r = 0$, the fluctuation component, $u_z(r, \theta, z, t) - \langle u_z \rangle_{\theta,z}(r, t)$, of the axial velocity. (For the spatio-temporal mean axial velocity $\langle u_z \rangle_{\theta zt}(r)$ see Fig. 2.7 below.) Lighter gray indicates higher values. The abscissa (z-axis) is shifted in the same manner as in Fig. 2.2(b). We observe a small turbulent region, where the shade of gray changes significantly, in the middle of the figure at $t = 3800$, when the mean axial velocity is increasing in time (see Fig. 2.2(c)). This turbulent region expands both in the radial and axial directions. A clear separation of the laminar and turbulent regions is established at $t = 4000$ and 4200 when the mean axial velocity takes larger values. This sharp border is the trailing edge of the puff. The turbulent region further spreads downstream (and hits the trailing edge of itself because of the periodic boundary conditions)

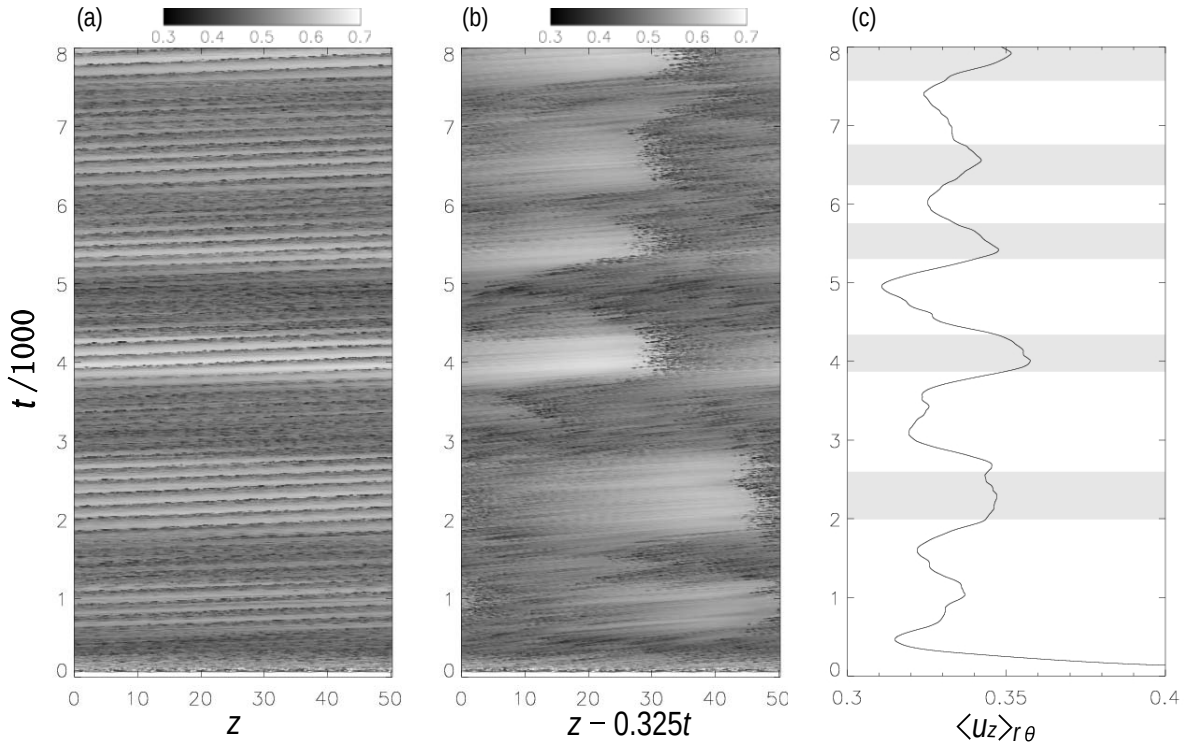

Figure 2.2: The spatio-temporal variation of the axial velocity u_z on the pipe centerline is shown in (a) on the (z,t)-plane and (b) on the $(z-0.325t,t)$-plane. (c) Temporal variation of the mean axial velocity $\langle u_z\rangle_{r\theta}(t)$. Five gray bands indicate the puff-existing periods used to define the shape of the trailing edge in §2.3.3. $Re = 3500$.

by $t = 4600$ and 4800. At this time the turbulence has spread throughout the computational domain. At $t = 5000$ a small laminar region appears at the left-end of the figure. This laminar region expands in the axial direction, reducing the turbulent region, until $t = 5400$ when another sharp trailing edge is generated at $t = 4000$. Thereafter the process repeats.

In Fig. 2.4 we plot the spatio-temporal evolution of the cross-axial component $(u_r^2 + u_\theta^2)^{1/2}$ of the velocity fluctuation. Again, lighter gray indicates higher values. Since the (θ, z) mean velocity is zero in this component, i.e. $\langle u_r \rangle_{\theta z} = 0$ and $\langle u_\theta \rangle_{\theta z} = 0$, the shade of gray represents directly the magnitude of fluctuation, unlike the axial component shown in Fig. 2.3. It is seen that the spatial variation is finer than that of the axial component (cf. Fig. 2.3) although the fluctuation magnitude changes similarly in the two components both in space and in time. In the next subsection this cross-axial component is used to define the sharp boundary of the puff.

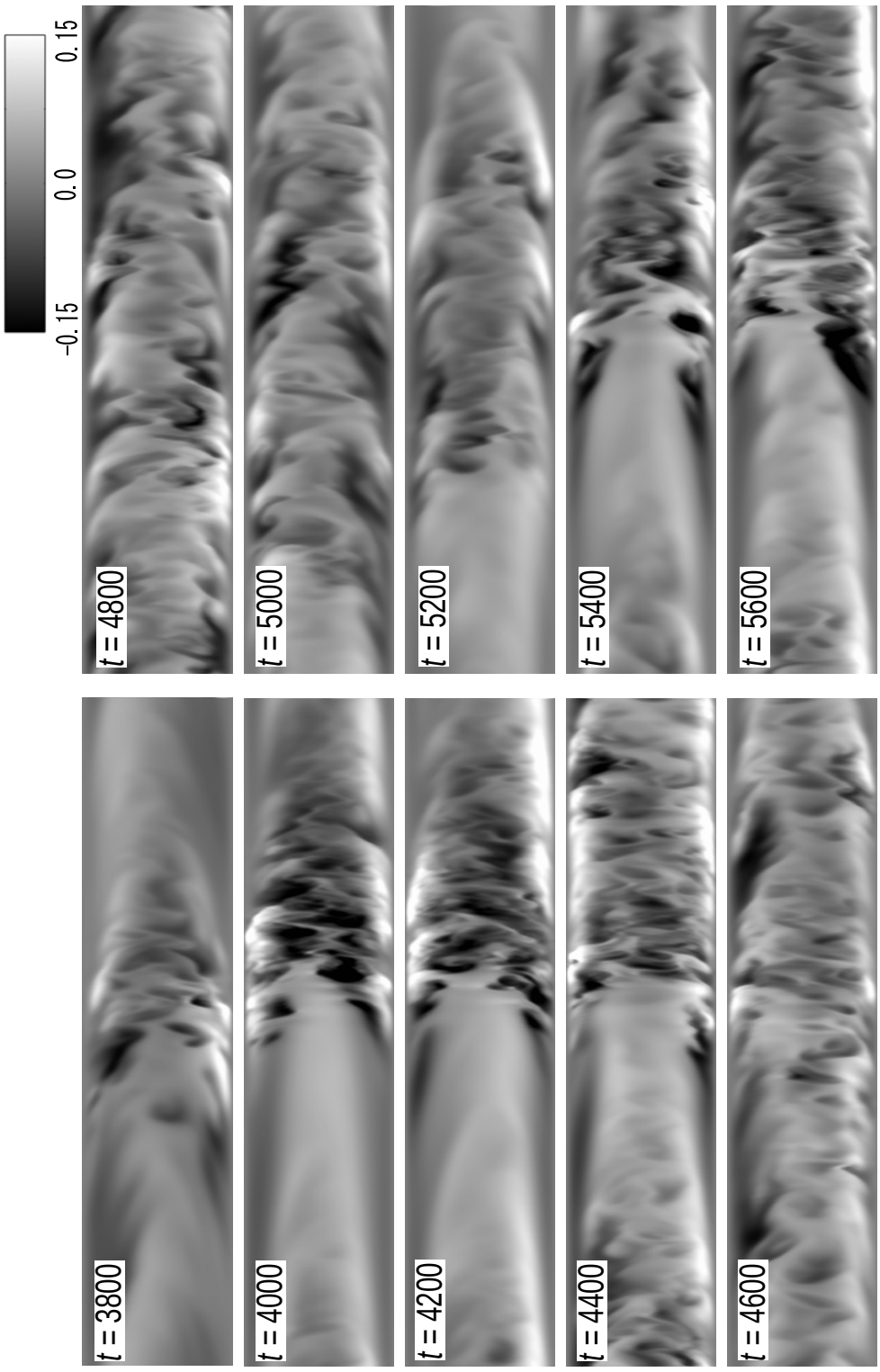

Figure 2.3: The spatio-temporal structure of the axial velocity shown on a plane ($\theta = 0$ and π) through the pipe centerline. The distribution of $u_z(r, \theta, z, t) - \langle u_z \rangle_{\theta z}(r, t)$ is plotted in gray scale with lighter gray for larger values. The ordinate, the radial direction, covers 2 in length. The abscissa, the axial direction, covers 16π and is shifted as in Fig. 2.2(b), so that the position of the puff may be as stationary as possible. $Re = 3500$.

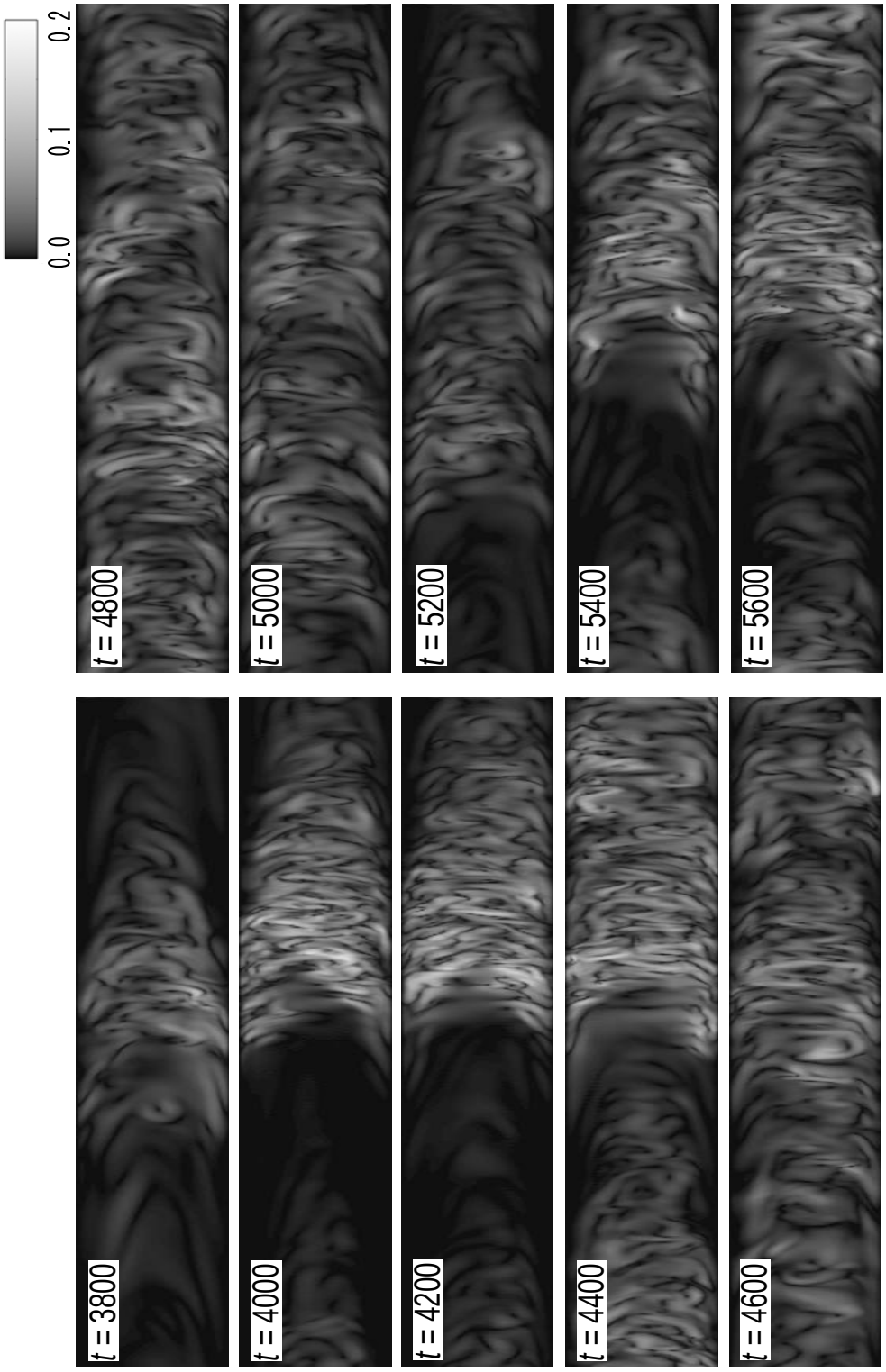

Figure 2.4: Same as Fig. 2.3 for the magnitude of cross-axial velocity $u_\perp = (u_r^2 + u_\theta^2)^{1/2}$.

2.3.3 Mean structure of the turbulent puff

We have seen in the preceding section that a turbulent puff is repeatedly generated and destroyed in a pipe at intermediate Reynolds numbers. Here we construct the mean structure of the turbulent puff, useful as a reference to investigate the dynamics of the puff.

Since the trailing edge of puff is relatively sharp, we are tempted to statistically estimate the shape from the velocity fluctuations in the puff. Here we consider the cross-axial velocity field $u_\perp = (u_r^2 + u_\theta^2)^{1/2}$. The instantaneous shape of the trailing edge is not smooth, but changes irregularly in time. For a better estimation of the mean puff shape, we use fluctuations when a puff is stably excited, that is when the mean axial velocity is larger (see Fig. 2.2(c)).

By noting that the velocity fluctuation decreases in magnitude downstream in a puff and that there is a sharp jump at the trailing edge, we compare, for a given position (r, θ) at a time t, the cross-axial velocity fluctuation $u_\perp(r, \theta, z)$ with a piecewise linear function having a discontinuity at $z = c(r, \theta, t)$, i.e.,

$$u_\perp = \begin{cases} a(z + L - c) + b & (0 \le z < c), \\ a(z - c) + b & (c \le z \le L) \end{cases} \tag{2.17}$$

over $0 \le z \le L$ by the least-squares method. Here L $(= 16\pi)$ is the spatial period in the axial direction, and $a(r, \theta, t)$, $b(r, \theta, t)$ and $c(r, \theta, t)$ are fitting parameters (see Fig. 2.5). The parameter $c(r, \theta, t)$ is averaged over θ. We then obtain the azimuthally averaged instantaneous shape $z = \overline{c}(r, t) + z_0$ of the trailing edge up to an arbitrary constant z_0. We have calculated such instantaneous shapes for 245 samples over five puff-existing periods, i.e. $[2000, 2590]$, $[3880, 4330]$, $[5310, 5750]$, $[6250, 6750]$, $[7580, 8000]$ every 10 time units. These periods are shown with gray bands in Fig. 2.2(c). The mean shape $\overline{\overline{c}}(r)$ is obtained from these 245 samples by applying least-squares again using z_0 as an adjustable parameter (Fig. 2.6). We denote the position of the trailing edge on the pipe centerline by Z_{TE}.

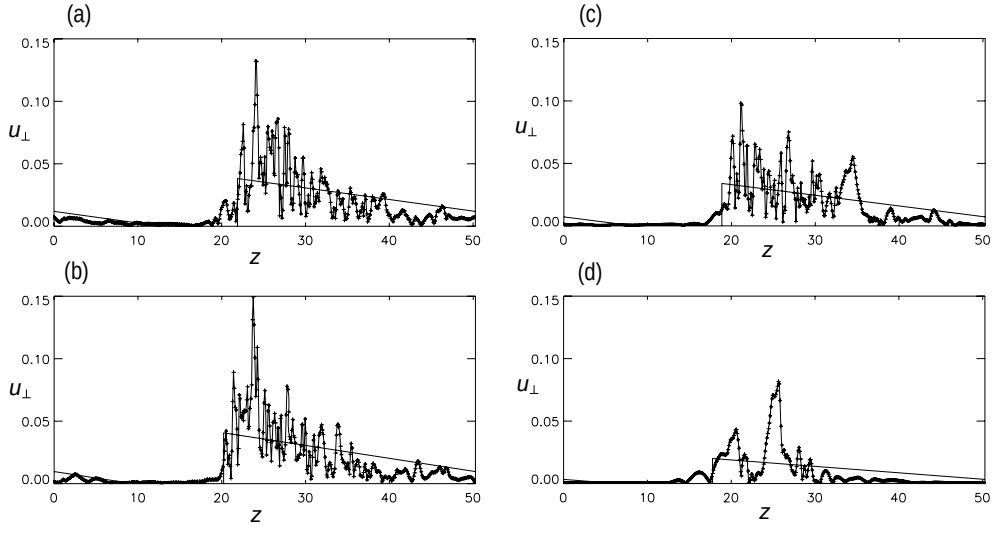

Figure 2.5: Examples of least-squares fitting of the trailing edge of a puff. The spatial distribution of the cross-axial velocity fluctuation $u_\perp = (u_r^2 + u_\theta^2)^{1/2}$ is compared with a piecewise linear function (2.17). (a) $r = 0$, (b) 0.3, (c) 0.6, (d) 0.9. $\theta = 0$, $t = 4000$, $Re = 3500$.

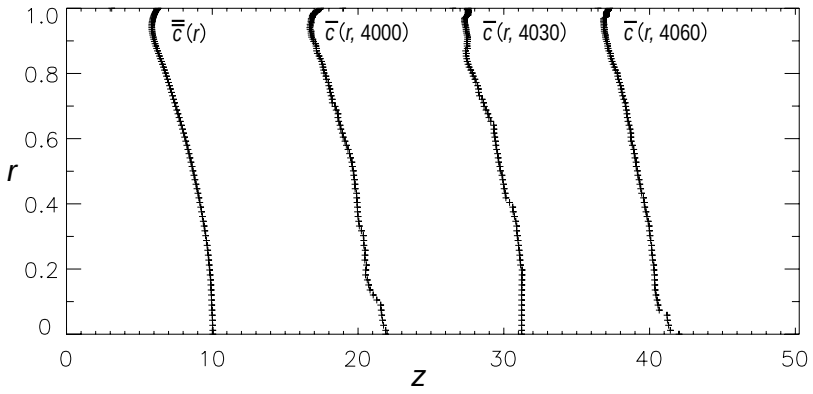

Figure 2.6: Mean shape $\overline{\overline{c}}(r)$ of the trailing edge of a puff obtained by the least-squares method using 245 instantaneous azimuthally averaged shapes, $\overline{c}(r,t)$. Here the position Z_{TE} of the trailing edge on the pipe centerline is set at $z = 10$, while the axial locations of the others are arbitrary.

Now that the mean shape of the trailing edge of a puff is determined, the velocity distribution associated with the puff can be constructed. The mean velocity field obtained by the use of the above 245 data is shown in Fig. 2.7 for (a) the excess of $\langle u_z \rangle_{\theta t}$ from $\langle u_z \rangle_{\theta z t}$, (b) the radial flux $2\pi r \langle u_r \rangle_{\theta t}$, (c) the cross-axial velocity fluctuation $\langle u_\perp \rangle_{\theta t}$, and (d) the streamlines of the mean velocity field relative to a moving frame with mean puff velocity 0.325. In (a) and (b) the positive regions are shaded. A thick solid line in each figure indicates the trailing edge of the puff. It is seen in (a) that the axial velocity u_z is larger or smaller than the advective velocity of the puff in the central or near-wall regions upstream of the trailing edge of the puff, and vice versa downstream of the trailing edge. The jump in u_z across the trailing edge is of $O(0.1)$. The radial component of velocity u_r (Fig 2.7(b)) shows flow towards the wall upstream near the trailing edge of the puff and towards to the center in the puff (see Fig 2.7(d)).

The cross-axial velocity in Fig 2.7(c) shows a clear contrast in magnitude across the trailing edge. Whereas the fluctuation is very weak in the upstream side, it is strong in the downstream side with decreasing intensity downstream. Such a simple and monotonical behaviour of the cross-axial velocity field justifies the choice of this quantity to estimate the shape of the trailing edge as described above. The structure of the azimuthally averaged velocity field is most conveniently seen in the streamlines of Fig. 2.7 (d). Most prominent is the existence of a circular motion upstream near the wall, downstream inside of the pipe and around the trailing edge. Since the advection velocity of the puff is close to the mean axial velocity of the flow, the net flux across the trailing edge is small, on average.

It is interesting to compare the present results with those obtained experimentally by Wygnanski *et al.* (1975). They identified the trailing edge of a puff using the experimental measurements of $\log|\partial u_z/\partial t| + \log|\partial u_r/\partial t|$ in a wind tunnel. This quantity fluctuates around the mean value. The position of trailing edge was defined as the last cross-point with the mean value. In this method the puffs in different snapshots were adjusted *locally* near the trailing edge, whereas in our present method they are adjusted *globally* over the puff. As a result, their mean fields are less smeared than are ours; their intensity of velocity fluctuations decreases downstream more rapidly, there is an additional eddy near the trailing edge of their puff, and so on. Similar

to Wygnanski *et al.* (1975), a mean field was obtained numerically by Priymak and Miyazaki (2004) using the same local adjustment of the trailing edge. The mean field obtained by Shan *et al.* (1999) was closer to ours, likely because their definition of the trailing edge was less local (their trailing edge was defined by a level of velocity fluctuation).

The radial distribution of mean axial velocity is shown in Fig. 2.8 around the trailing edge of the puff as well as the average taken over the whole domain. Upstream of the trailing edge ($z = Z_{TE} - 10$) it is close to the laminar profile, whereas downstream ($z = Z_{TE} + 10$) it resembles the turbulent distributions. On the trailing edge ($z = Z_{TE}$) the axial velocity is close to the turbulent profile in the near-wall region, and to the laminar one in the interior. The shapes of the velocity profiles are qualitatively similar to those of Wygnanski *et al.* (1975), Shan *et al.* (1999) and Priymak and Miyazaki (2004), although our definition of the trailing edge is different.

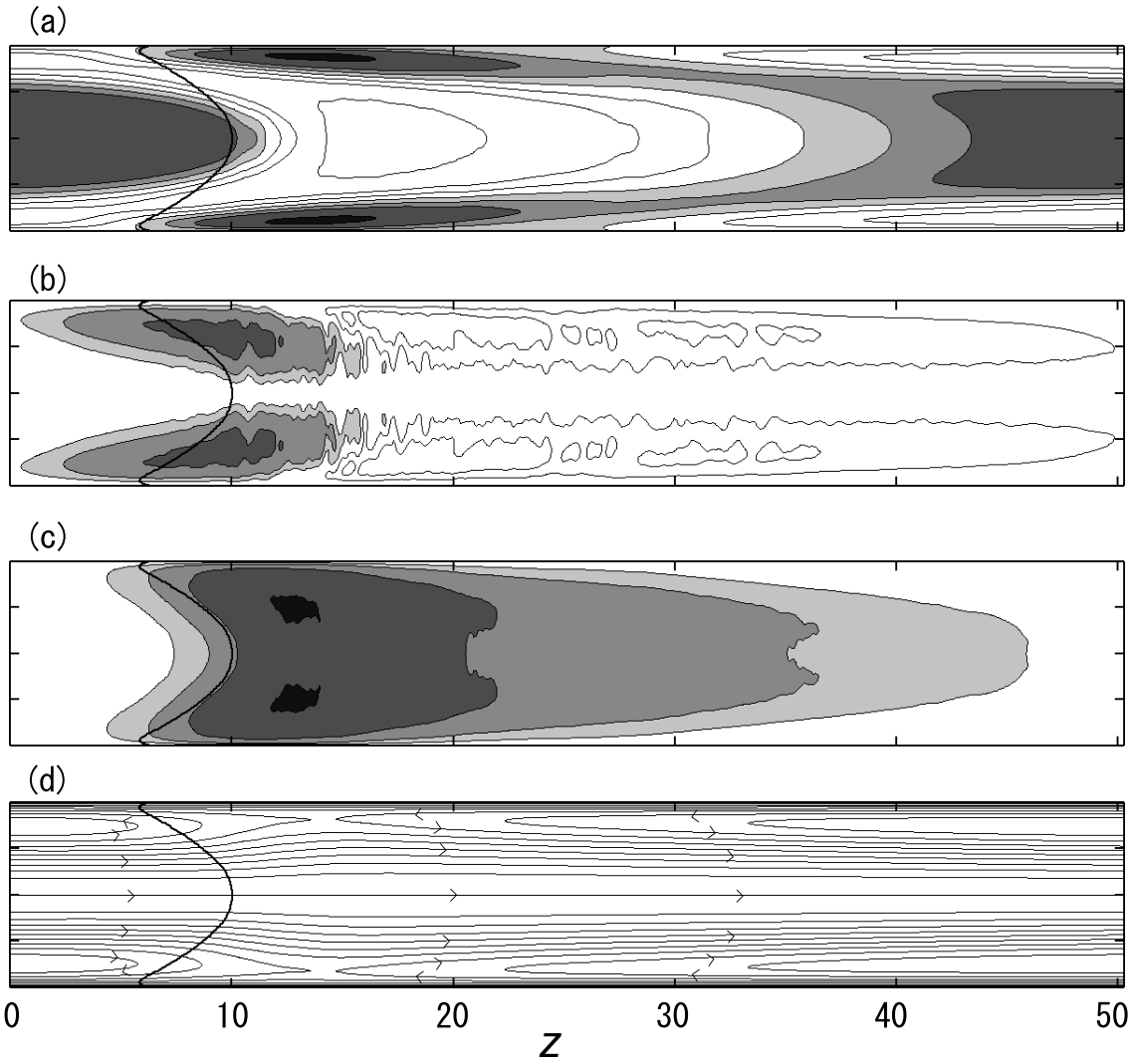

Figure 2.7: Mean velocity field associated with a puff. A thick curve in each figure indicates the trailing edge of the puff, the center of which is positioned at $z = 10$ ($\equiv Z_{TE}$). The horizontal length of the domain shown here is 16π in the axial direction, whereas the vertical length is 2 in the radial direction. (a) $\langle u_z \rangle_{\theta t} - \langle u_z \rangle_{\theta z t}$ (see the solid line of Fig. 2.8 for $\langle u_z \rangle_{\theta z t}$), (b) $2\pi r \langle u_r \rangle_{\theta t}$, (c) $\langle u_\perp \rangle_{\theta t}$, (d) Streamlines of azimuthally averaged mean velocity field in a frame moving with velocity 0.325. Contour levels are -0.05, -0.025, -0.0125, 0, 0.0125, 0.025, 0.05 in (a), -0.003, -0.001, 0.001, 0.003, 0.009 in (b), and 0.005, 0.01, 0.02, 0.04 in (c). The positive parts are shaded in (a) and (b).

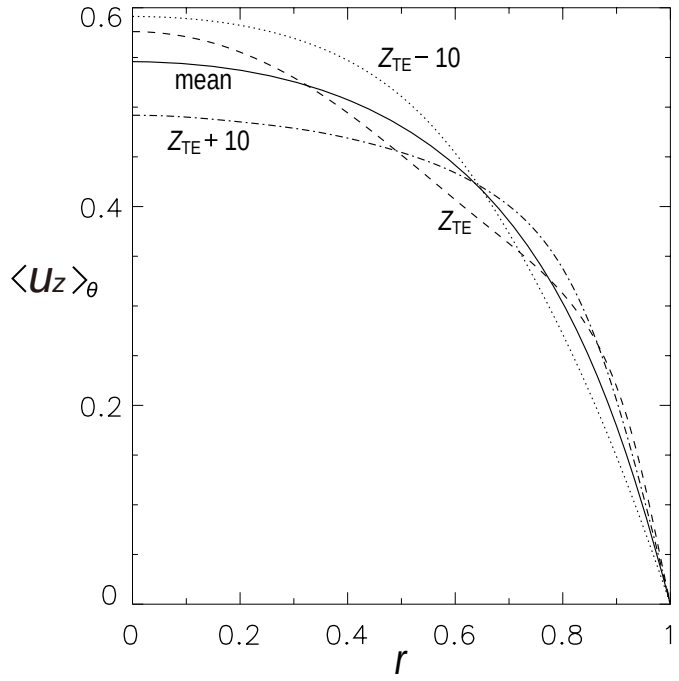

Figure 2.8: Radial distribution of azimuthally averaged axial velocity $\langle u_z \rangle_\theta(r, z)$. The dashed line, dotted line and dot-dashed line are for $z = Z_{TE}$, $Z_{TE} - 10$ and $Z_{TE} + 10$, respectively, where Z_{TE} indicates the position of trailing edge at the tube center line ($r = 0$). The solid line is the mean axial velocity $\langle u_z \rangle_{\theta z}(r)$ averaged also over z.

2.4 Concluding remarks

Since the steady Hagen-Poiseuille flow in a circular pipe is linearly stable for any value of *Re*, it is difficult to find in DNS an appropriate initial condition which leads to a turbulent puff near the critical Reynolds number. In fact, in many previous DNS an artificial forcing[Shan *et al.* (1999), Willis and Kerswell (2007)] was imposed during an initial period or a fully-developed turbulent state was used as the initial condition [Priymak and Miyazaki (2004)]. In this paper we succeeded in creating a turbulent puff by starting with the Hagen-Poiseuille flow superimposed with perturbations of finite amplitude.

Another point to be stressed is our application of a spectral method in the cylindrical coordinate system. A numerical scheme of high accuracy and low numerical dissipation such as the spectral method is desirable to predict accurately complicated structures in turbulence. The commonly-used Chebyshev polynomials for expansions in the radial direction suffer from the singularity in the cylindrical coordinate representation on the pipe centerline and deteriorate the numerical accuracy. In this paper we used Zernike polynomials,[Bhatia and Born (1954), Matsushima and Marcus (1995), Verkley (1997)] which automatically avoid the singularity and predicts the velocity field with high accuracy.

The turbulent puffs we have observed in the present DNS have finite life-times; they appear and disappear repeatedly. It is seen from Fig. 2.2 that the life-time of the puff is about $500a/U$ and that the period of appearance is about $1000a/U$. The reason for this quasi-periodic behaviour is not clear. One possible reason is the effect of spatial periodicity in computa-

tion. As seen in Fig. 2.3, the axial length of a turbulent puff increases in time. Because of spatial periodicity of the flow field, a puff collides with its image in the next neighbouring periodic domain when the axial length of the puff reaches the spatial period. Then the sharpness of the trailing edge disappears and the level of velocity fluctuations is lowered. The mechanism of this destruction is not known. By inspection we see that a growing puff occupies the whole domain L ($= 16\pi$) in $500a/U$ and we estimate the speed of the expansion of the axial length of the puff as $0.1U$. This speed is comparable with that observed experimentally at $Re_m \simeq 2300$.[Azuma and Araga (2001)] As another possible reason for the generation-and-destruction behaviour is a self-sustaining process similar to that in wall-bounded shear flows.[Hamilton *et al.* (1995), Waleffe (1997)] Further analysis of the numerical data is required to examine this scenario.

We have determined the shape of the sharp boundary (the trailing edge) of a puff by the least-squares method using the cross-axial fluctuations in the puff. This boundary may be useful for a reference when we consider the flow dynamics associated with a puff, such as the generation and destruction of a puff. This research is now underway.

Chapter 3

A driving mechanism of a turbulent puff in pipe flow

A turbulent puff is numerically realized in a circular pipe flow driven by a constant uniform external force. The periodic boundary condition is imposed in the axial direction with period of 16π pipe radius. The Reynolds number based on the pipe radius, the centerline velocity of the Hagen-Poiseuille flow corresponding to the external force is 3000. Starting with the Hagen-Poiseuille flow superposed by a disturbance of finite amplitude, an equilibrium puff of about 11π pipe radius in length emerges and advects with nearly the mean flow velocity. Turbulence in the puff generates a number of low-speed streaks accompanied with streamwise vortices along the pipe wall. These low-speed streaks move upstream relative to the puff, across the trailing edge and create strong thin vortex layers, arched above the streaks, together with the laminar flow coming from upstream. The vortex layers, the thickness of which is typically a few times smaller than the width, are unstable to roll up, through the Kelvin-Helmholtz instability, to induce velocity fluctuations which propagate downstream faster than the puff itself and enhance the turbulent activity in it. This self-sustenance cycle of an equilibrium puff is numerically verified.

3.1 Introduction

In the study of laminar/turbulent transition of a circular pipe flow driven by a constant external force Reynolds (1883) proposed and measured two critical parameters. One is the lower critical Reynolds number below which the steady Hagen-Poiseuille flow always recovers against any initial disturbance of arbitrary magnitude but above which a non-trivial flow (other than the Hagen-Poiseuille flow) can be excited and survive for ever from some initial condition. The other is the upper critical Reynolds number above which the steady Hagen-Poiseuille flow is unstable for some infinitesimal disturbances, implying that unavoidable disturbances prevent us to maintain the Hagen-Poiseuille flow in real experiments. The latter Reynolds number is now commonly believed to be infinitely large on the basis of subsequent laboratory experiments as well as the linear stability analysis (Phenninger 1961, Salwen *et al.* 1980). The prediction of the former one, on the other hand, is difficult and unsolved primarily because it is a nonlinear

phenomenon. Experimentally, the lower critical Reynolds number is known to be about 2000 which is slightly smaller than 2300, the value that Reynolds (1883) obtained.

One approach to determine the lower critical Reynolds number is to search a non-trivial solution of the Navier-Stokes equation for the Reynolds number as small as possible. The travelling-wave solutions (Faisst and Eckhardt 2003, Wedin and Kerswell 2004, Kerswell 2005) and the unstable periodic flows, like the one discovered in the Couette system (Nagata 1997, Kawahara and Kida 2001, Viswanath 2007), are promising candidates.

As already noticed in Reynolds' experiments (1883), the flow can be partially laminar and partially turbulent around the lower critical Reynolds number. A number of localized turbulent regions, called the turbulent puff, appear and disappear intermittently. Depending on the Reynolds number, the size of a puff may increase, decrease, or hardly change with time (Wygnanski and Champagne 1973, Wygnanski *et al.* 1975). That puff of which the size hardly changes is called the equilibrium puff. As a prototype of turbulent puffs the equilibrium puff has been studied by many authors both experimentally (Bandyopadhyay 1986, Darbyshire and Mullin 1995, Azuma and Araga 2001, Hof *et al.* 2004) and numerically (Shan *et al.* 1999, Priymak and Miyazaki 1994, 2004, Wilis and Kerswell 2007) to find the basic properties such as the advection velocity of a puff as well as the turbulence characteristics in the puff. Most of turbulent activity is produced near the upstream laminar/turbulent interface. Bandyopadhyay (1986) discovered the wake-like structures excited periodically in time and stressed that the axi-symmetric Kelvin-Helmholtz instability never takes place.

There are two different ways to realize the steady Hagen-Poiseuille flow at smaller Reynolds numbers below the critical and also the statistically stationary turbulent flows above the critical. One is to drive the flow by a constant forcing (e.g. gravity) along the pipe axis. The other is to drain the fluid from the downstream end of a long-but-finite pipe with a constant flux (Darbyhire and Mullin 1995). The former may be the simplest and natural way to perform in laboratory, and is the most popular and traditional method since Reynolds (1883). The flow flux (the mean axial velocity over cross-sections of the pipe) may change in time when the flow becomes unsteady though it is invariant in time when the Hagen-Poiseuille flow is realized. In the latter, on the other hand, the flow flux is always fixed to a given value. Both of these two different forcing systems is useful for us to reveal the physics of the most sensitive state, i.e. the flow around the laminar/turbulent transition.

Compared with the channel flow between two parallel plates, the numerical study of pipe flow is considerably few primarily because the circular geometry makes it more difficult. The direct numerical simulation (DNS) of the Navier-Stokes equation was conducted for fully developed turbulence in a pipe by Eggels *et al.* (1994). Concerning the turbulent puff, Priymak and Miyazaki (1994, 2004) conducted the DNS to realize an equilibrium puff by employing a turbulent state as the initial condition and analysed the structure and the advection velocity of a puff.They noticed that the minimum admissible period in the axial direction to realize a puff is about 16π pipe radius. Another detailed numerical study was performed by Shan *et al.* (1999) in which the puff was not in equilibrium but its size increased in time. Recently, Shimizu and Kida (2008) developed a spectral code to simulate the pipe flow with higher accuracy by using the Zernike polynomials in the radial direction (Bhatia and Born 1954, Matsushima and Marcus 1995, Verkley 1997). This paper will be referred to SK08 in the following.

The main purpose of this chapter is to numerically realize an equilibrium puff and to investigate the generation and sustenance mechanism of it. In the next section (section 2), after

introducing the flow system to be studied and the numerical method to solve it, we describe the characteristics of a turbulent puff obtained by DNS. We define the leading edge and the trailing edge of a puff in terms of the axial velocity distribution on the pipe axis, and calculate the advection velocity and size of the puff, as well as the propagation velocity of fluctuations. Then, in section 3, we propose a self-sustenance cycle of a turbulent puff. The roll-up of vortex layers taking place near-upstream of the trailing edge by the Kelvin-Helmholtz instability plays a primary role in enhancement of the turbulent activity in a puff through cooperative interactions with the low-speed streaks and the turbulence itself. Finally, the concluding remarks are given in section 4.

3.2 Turbulent puff

3.2.1 Numerical method

We investigate by DNS the motion of an incompressible viscous fluid in a straight stationary circular pipe of infinite length, which is driven by a time-independent uniform body force. The flow is assumed to obey the Navier-Stokes equation with non-slip boundary conditions on the pipe wall. The periodic boundary condition is imposed for the velocity field in the axial direction. Throughout this paper all the physical quantities are non-dimensionalized in terms of the pipe radius a, the centerline velocity U of the Hagen-Poiseuille flow (which would be realized by the external body force), and the kinematic viscosity ν of fluid. This system then has a single non-dimensional parameter, $Re = Ua/\nu$, called the Reynolds number. The flow state is characterized by Re only, apart from the initial condition, if the period in the axial direction is sufficiently large.

In SK08 we saw that the flow state in a pipe is different after a long time, depending on the Reynolds number; either the laminar, the intermittent, or the turbulent states (see Fig. 1 of SK08). For smaller Reynolds numbers ($Re \leq 3000$), after a transient time the flow eventually approaches a laminar state, i,e. the steady Hagen-Poiseuille flow. For larger Reynolds numbers ($Re \geq 6000$), on the other hand, unsteady variations of the flow field spread throughout the computational domain and seems to continue for ever with the mean properties, such as the mean axial velocity and the r.m.s. of the velocity variations, being almost stationary (the standard deviation is typically less than a few tens percents). This is the turbulent state. Furthermore, for intermediate Reynolds numbers ($3300 \leq Re \leq 4000$, or $2397 \leq Re_m \leq 2449$, where $Re_m = 2a\langle u_z\rangle_{r\theta}/\nu$ is the Reynolds number based on the mean axial velocity $\langle u_z\rangle_{r\theta}$ averaged over the cross-sectional (r,θ) place) the flow state is somewhat complicated; the flow field is unsteady and the fluctuation level is non-uniform in space, and a localized region with relatively large fluctuation, called a turbulent puff, moves downstream with nearly the same speed as the mean flow. Such a turbulent puff seems never to die out. This is called the intermittent state. These numbers of transition Reynolds number are consistent with other works; 2200 (Shan *et al.* 1999), 2200 and 2350 (Priymak and Miyazaki 1994), and 1900 (Willis and Kerswell 2007).

Since the numerical method is described in SK08, we do not repeat it here, but give only necessary information for the present paper. The cylindrical polar coordinate system (r,θ,z) is introduced to describe the flow with the z-axis on the pipe axis. The velocity field is expressed by the toroidal/poloidal representation. The toroidal and poloidal functions are expanded by the Fourier series in the axial (z) and azimuthal (θ) directions and by the Zernike polynomials $\Phi_n^m(r)$ in the radial (r) direction (Bhatia and Born 1954, Matsushima and Marcus 1995, Verkley 1997). For example, the toroidal function ψ is expanded as

$$\psi(r,\theta,z,t) = \sum_{k=-K}^{K}\sum_{m=-M}^{M}\sum_{n=|m|}^{N}\widehat{\psi}_n^{mk}(t)\Phi_n^m(r)\exp[\mathrm{i}(m\theta + (2\pi/L)kz)],$$

where the last summation is taken for $n+m =$ even. Integers N, M and K indicate the numbers of truncation modes, and L is the period in the axial direction. Note that the Zernike polynomials guarantee the analyticity of the expanded functions at the pipe axis $r = 0$. The evolution equations for the expansion coefficients $\widehat{\psi}_n^{mk}(t)$ and the corresponding ones for the poloidal function,

are derived from the Navier-Stokes equation. For time integration we employ the second-order Adams-Bashforth scheme for the nonlinear term and the Crank-Nicolson scheme for the viscous term. The τ-method is employed to satisfy the boundary conditions.

The axial period is set at $L = 16\pi$ (≈ 50) which is close to the minimal admissible value for which a turbulent puff is excited and sustained (see Priymak and Miyazaki 2004, SK08). The initial condition is prepared in the same way as in SK08 except for the amplitude of disturbance being doubled. The initial disturbance is spread uniformly over the entire periodic domain. With the number of truncation modes $(N, M, K) = (80, 31, 511)$ and time increment $\Delta t = 0.005$ we perform DNS over $0 < t \leq 3000$ for the Reynolds number $Re = 3000$. For the present DNS of uniform forcing the mean wall friction $\langle \tau_w \rangle_{\theta z}(t)$ averaged over the whole pipe wall is equal to $2/Re$ in the mean (with respect to time) if the flow is statistically stationary in time, where $\tau_w \equiv (1/Re)\partial u_z/\partial r|_{r=1}$. Here, $\langle \cdots \rangle_{\theta z}$ stands for the average over θ and z. The local wall-friction $\langle \tau_w \rangle_\theta (z, t)$ takes a minimum (about 80% of the mean) at the middle of the laminar region, and a maximum (about 130 – 170% of the mean) in the middle of the puff. The mean friction velocity and length are $u_\tau = \sqrt{2/Re}$ and $l_\tau = \sqrt{1/2Re}$, respectively. For $Re = 3000$ the friction length l_τ takes 0.0129, so that the circumference of the circular pipe is 487 ($= 2\pi/0.0129$) times l_τ. The grid spacing (or the Gauss-Radau quadrature points) in the radial direction is non-uniform; it is a decreasing function of r, taking $(\Delta r)_0 = 0.029 = 2.2 l_\tau$ on the pipe axis and $(\Delta r)_{\frac{1}{2}N+1} = 0.0010 = 0.081 l_\tau$ at the pipe wall. The minimum resolved wavelength in θ is $2\pi(\Delta r)_0/M = 0.45 l_\tau$ on the pipe axis and $2\pi/M = 15.7 l_\tau$ at the pipe wall. The minimum resolved wavelength in the axial direction is uniform, taking $L/K = 7.6 l_\tau$. The total integration time is $3000 = 77\, u_\tau^{-1}$.

In figure 3.1 we plot the temporal evolution of the spatial mean axial velocity $\langle u_z(r, \theta, z; t) \rangle_{r\theta}(t)$ (which is independent of z) with a solid line over $0 \leq t \leq 3000$. Note that the value 0.5 of the mean axial velocity corresponds to the one for the Hagen-Poiseuille flow. The deviation from 0.5 is therefore an indication that the flow is different from the Hagen-Poiseuille flow. It is seen that after a transient initial period ($t < 500$), $\langle u_z \rangle_{r\theta}(t)$ seems to vary around a mean value, thus the flow is in a statistically stationary turbulent state. The temporal mean $\overline{u}_z$ of $\langle u_z \rangle_{r,\theta}(t)$ averaged over period $2000 \leq t \leq 3000$ is 0.371 with standard deviation of 0.005. The mean mass-flux Reynolds number is then $Re_m = 2226$.

The dashed line in this figure represents the results obtained in SK08 for nearly the same initial condition (e.g. 20% difference in u_z on the pipe centerline) as the present one but with different number of modes $(N, M, K) = (100, 21, 170)$. The mean axial velocity approaches 0.5, implying that the flow returns to the Hagen-Poiseuille flow. This surprising result is a manifestation of the sensitivity of flow states on numerical parameters in laminar/turbulent transition region of the Reynolds number. It has been long recognized both experimentally and numerically (e.g. Wygnanski and Champagne 1973, Darbyshire and Mullin 1995, Faisst and Eckhardt 2004) that the intermittent state is indefinite and subtle; for a given Reynolds number different intermittent states can emerge if either the initial condition or the numerical parameters (such as the number of truncation modes, the time increment, the spatial period L, etc.) are different. There is no guarantee therefore that the present turbulent state will not decay to the laminar flow after a long time. Keeping it in mind, we here investigate the present turbulent flow.

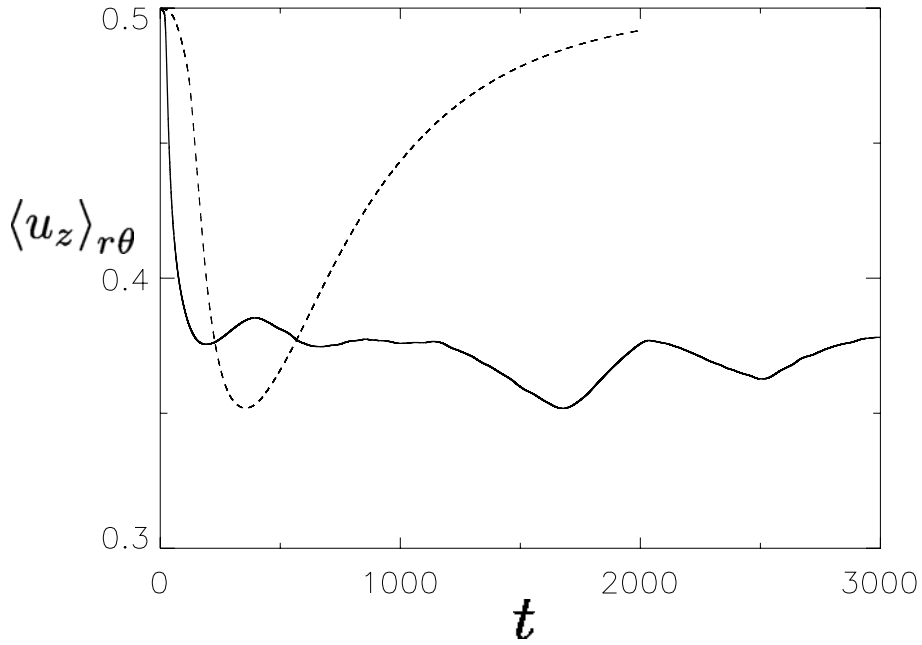

Figure 3.1: Time variation of spatial mean axial velocity. A solid and a dashed lines respectively represent runs for resolutions $(N, M, K) = (80, 31, 511)$ and $(100, 21, 170)$ with nearly the same initial condition. $Re = 3000$.

3.2.2 Instantaneous structure

In order to see the characteristics of a turbulent puff we show, in figures 3.2–3.6, several cross-sections of the velocity field at a particular time $t = 2000$. In these figures, for the purpose of convenience, the origin ($z = 0$) of the axial coordinate is set at the place where the azimuthal-mean wall friction takes the minimal value at this time instant (see figure 3.7 below).

The solid line in figure 3.2 represents the axial distribution of the axial component $u_{zc}(z,t)$ of velocity on the pipe axis at time $t = 2000$. A rapid drop of the velocity at the upstream front (z_T, see equation (3.1)) and gradual recovery accompanied with damping oscillation toward downstream are the most prominent characteristic features of a turbulent puff, which have been used by many authors to identify the puff. The leading edge (the downstream front) of a puff is obscure in contrast to the clear trailing edge (the upstream front). It is not easy therefore to define the precise size and position of a puff. There have been several practical methods proposed in literature to delineate the domain of a puff, e.g. by 10% fluctuation level of u_z for both the trailing and leading edges (Shan *et al.* 1999) or by a given threshold to $(\partial u_z/\partial t)^2(\partial u_r/\partial t)^2$ for the trailing edge (Wygnansky *et al.* 1975). Here, we propose a new simple method to define the boundary of a puff. To do it we compare the axial velocity $u_{zc}(z,t)$ on the pipe axis with a piecewise linear function of the axial coordinate as

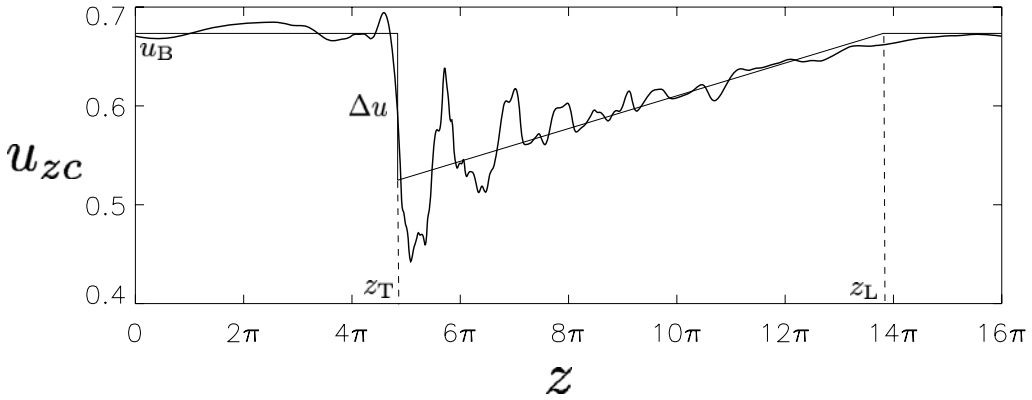

Figure 3.2: Axial velocity on the pipe axis. The axial distribution of $u_{zc}(z,t)$ is drawn with a thick curve over the whole computational domain at $t = 2000$. The broken line represents the least-squares fit of $u_{zc}(z,t)$ with equation (3.1). Here, z_L defines the leading edge of the puff, z_T the trailing edge, u_B the background velocity, and Δu the velocity jump at the trailing edge.

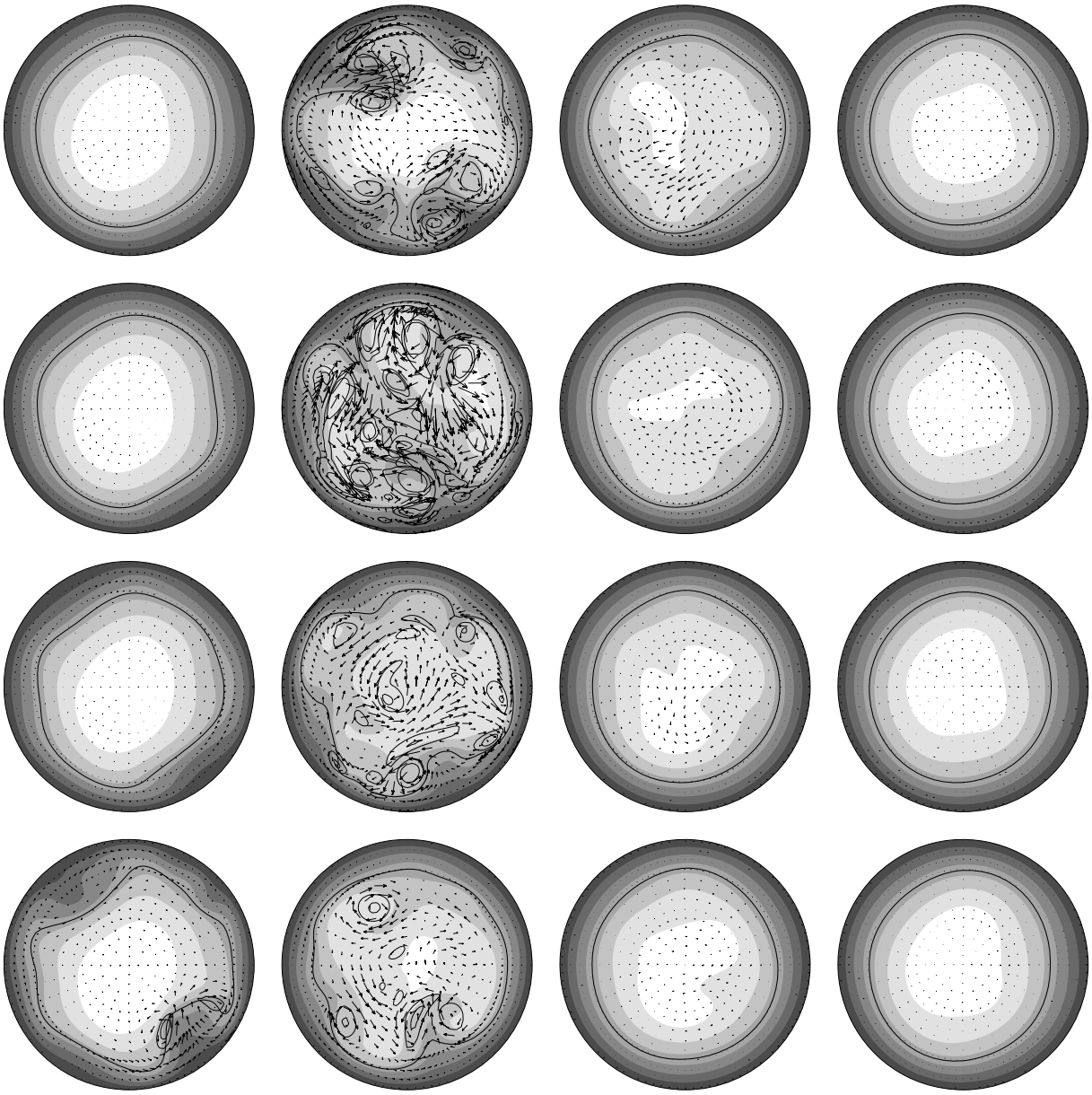

Figure 3.3: Round cuts of a turbulent puff. The velocity field is shown on 16 cross-axial planes with equal distance apart. The axial position of the planes are shifted by π downstream from the top-left to the bottom-right, first downward then rightward. The cross-axial velocity is shown by arrows with length proportional to the magnitude. The gray scale shows the axial velocity with lighter gray for larger values. The contour levels are 0, 0.1, $\cdots$, 0.6. Thick closed curves indicate the mean advection velocity $U_p = 0.355$ of the puff. The magnitude $|\omega_z|$ of axial component of vorticity is depicted by thin contours with levels of 0.5 and 1. The flow is directed out of the page. The origin of the azimuthal angle is set at the right of circles. $t = 2000$.

$$u(z) = \begin{cases} u_B + \Delta u \dfrac{z_L - z}{z_L - z_T} & (z_T \le z \le z_L), \\ u_B & (z < z_T \ \text{ or } \ z > z_L), \end{cases} \tag{3.1}$$

where z_L, z_T ($< z_L$), u_B and Δu are constants which represent the leading-edge position, the trailing-edge position, the background velocity and the velocity jump at the trailing edge, respectively. In equation (3.1) we have assumed that $z_T < z_L$. But even when $z_T > z_L$ in the computational domain, we have the same expression by an appropriate change of variables since the velocity field is periodic in z. The broken line drawn in figure 3.2 is obtained by the least-squares fit between $u_{zc}(z)$ and equation (3.1).

Figure 3.3 shows the velocity field on 16 cross-axial planes which cover the whole computational domain with equal distance apart. The location of the top-left cross-section is set at $z = 0$, and the others are shifted by π downstream, first from top to bottom, then from left to right, toward the bottom-right one. The flow is directed out of the page. The cross-axial component of velocity is shown by arrows with length being proportional to the magnitude, and

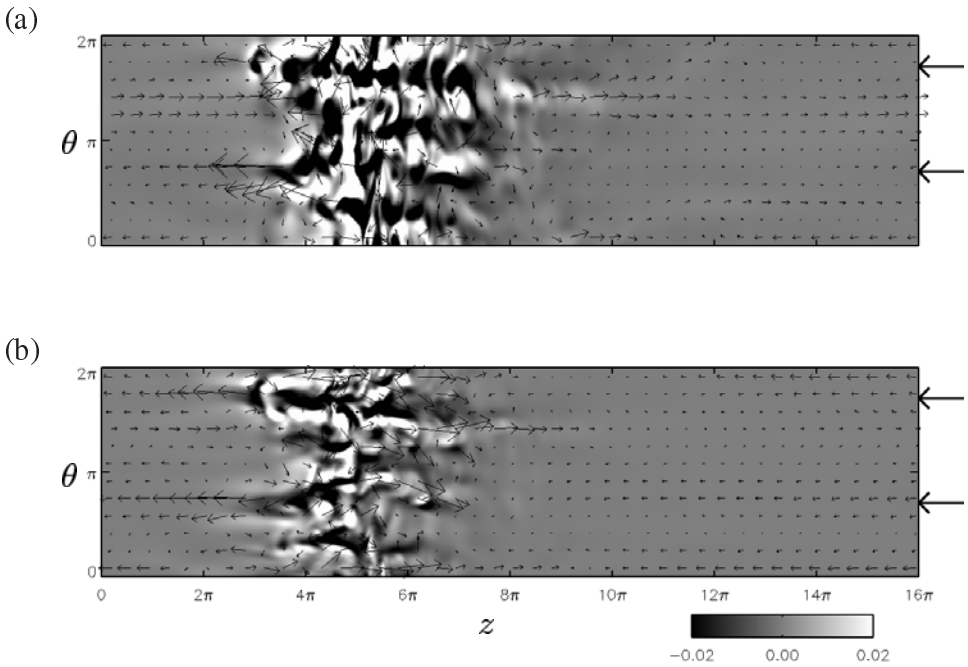

Figure 3.4: Cross-sections of a turbulent puff on cylindrical surfaces of radii (a) $r = 0.61$ and (b) 0.81. The velocity vectors subtracted the mean velocity averaged over the individual planes are represented by distributed arrows, whereas the radial velocity by the gray scale. The long arrows on the right of the panels indicate the azimuthal positions of low-speed streaks. $t = 2000$.

the axial component by gray scale with lighter gray for larger values. The magnitude $|\omega_z|$ of the axial component of vorticity is depicted by thin contours with levels 0.5 and 1. Thick closed curves indicate the mean advection velocity U_p (see section 2.3) of the puff. Several interesting characteristics of the flow are immediately recognized. Firstly, the cross-axial component of velocity takes large values only in a limited number of cross-sections, from the fourth to eighth, say. Second, the velocity variation is far from axi-symmetric, and several swirling motions of various sizes and of either sense of rotation exist. Third, several pairs of swirling motions of opposite rotations are observed near the pipe wall accompanied with low-speed streaks (represented by dark gray) between them.

Figure 3.4 shows the velocity field on cylindrical planes of (a) $r = 0.61$ and (b) 0.81. Here, distributed arrows indicate the (z, θ) component of velocity subtracted the mean value averaged over the individual planes, whereas the gray scale the r component with lighter gray for larger values. We see that the axial extent of large fluctuations is narrower near the pipe wall, that there are a couple of low-speed streaks (indicated by long arrows on the right end), which happen to be located opposite with respect to the pipe axis outside the region of large fluctuations, that the trailing edge has a wedge-shape pointed upstream along these low-streaks, and that alternate signs of u_r are aligned along the low-speed streaks.

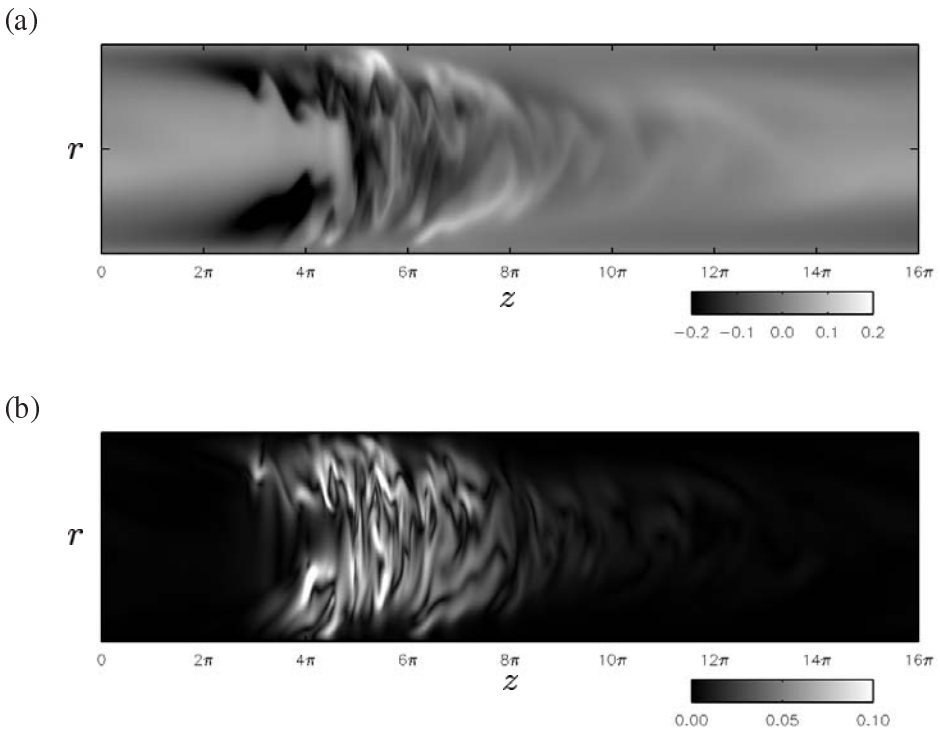

Figure 3.5: A longitudial cross-section of a turbulent puff. (a) The axial velocity $u_z - \langle u_z \rangle_{\theta z}$. (b) The cross-axial velocity $\sqrt{{u_r}^2 + {u_\theta}^2}$. The flow points from left to right. This cross-section passes through the two low-speed streaks seen in figure 3.4. $t = 2000$.

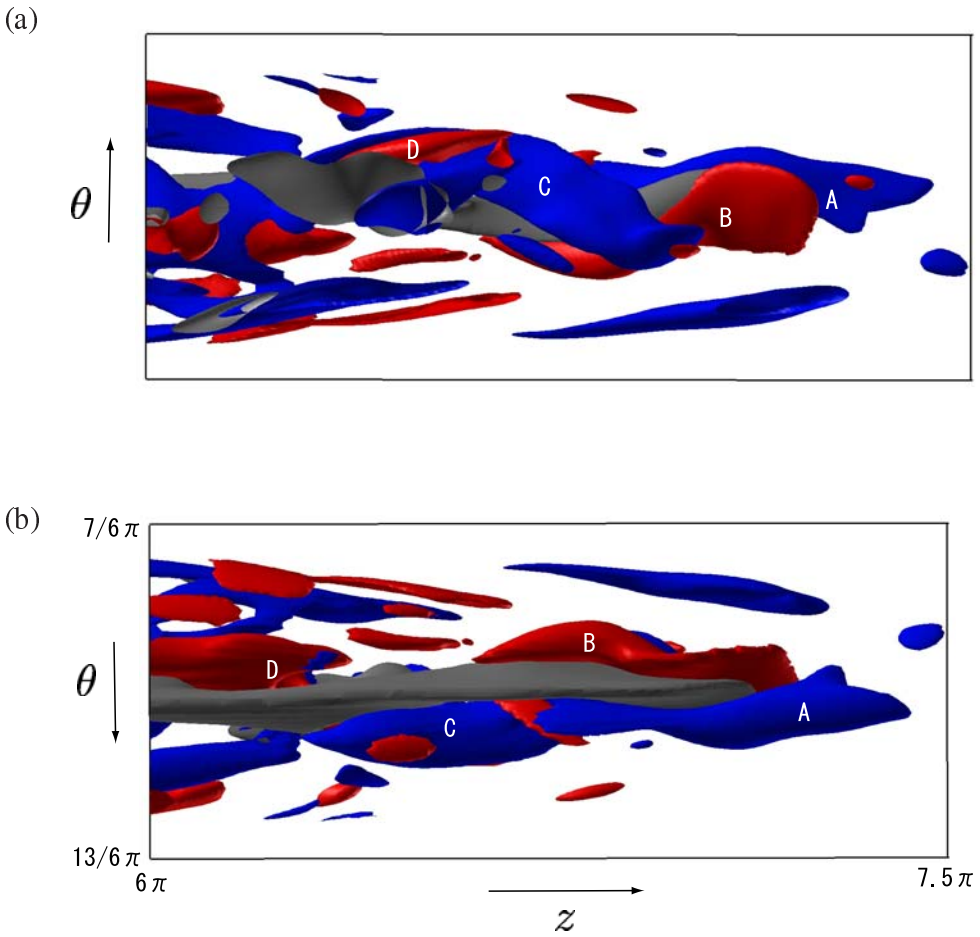

Figure 3.6: A low-speed streak and accompanied streamwise vortices. The regions of low axial velocity $u_z - \langle u_z \rangle_{\theta z} < 0.1$ are plotted with gray iso-surfaces. The red and blue iso-surfaces are the regions of high axial vorticity of positive $\omega_z > 0.5$ and of negative $\omega_z < -0.5$, respectively. The domain shown here is a semicircular cylinder, $\frac{7}{6}\pi \leq \theta \leq \frac{13}{6}\pi$ and $6\pi < z < 7.5\pi$, between the seventh and the ninth cross-sections from top-left in figure 3.3. Alphabets A, B, C and D identify the individual streamwise vortices. The flow is directed from left to right. (a) Outward view from the pipe axis. (b) Inward view from the pipe wall.

Figure 3.5 shows the velocity field of (a) the axial component and (b) the cross-axial component on the diametral plane which crosses the two low-speed streaks seen in figure 3.4. The flow is directed from left to right. It is clear that the large fluctuation in the velocity field are limited roughly between $3\pi < z < 8\pi$. The fluctuation starts earlier (or extends more upstream) near the wall, whereas decays slower (or extends more downstream) around the pipe axis. Many stripes of contrast perpendicular to the pipe axis are a prominent characteristics of the puff. They are advected downstream faster than the puff except near the pipe wall where they are slower (see figures 3.14 below). The fluctuations in the axial component u_z and the cross-axial component

$u_\perp$ are roughly the same in magnitude; they are bounded as $-0.30 < u_z < 0.18$ and $u_\perp < 0.17$ in figure 3.5.

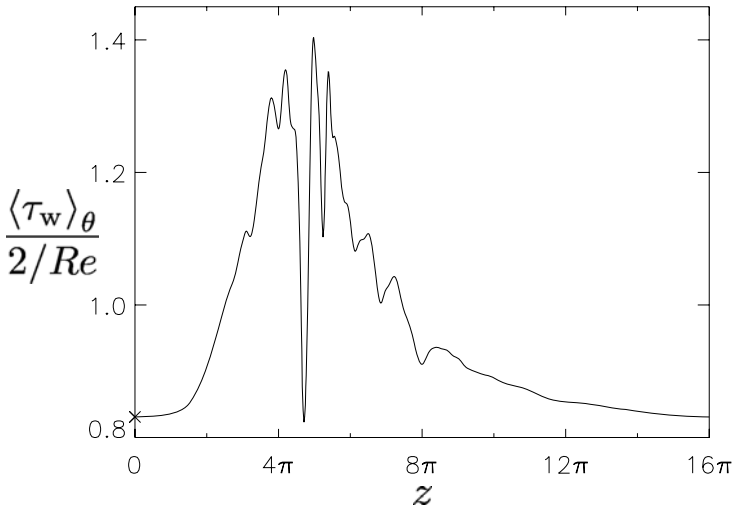

Figure 3.7: The axial distribution of the mean wall-friction $\langle \tau_w \rangle_\theta$ averaged over the azimuthal angle. The origin of the abscissa is adjusted to the local minimal point, indicated by $\times$, upstream of the trailing edge. The wall-friction is normalized by $2/Re$, the value it would take when balanced with the present external force. $t = 2000$.

It is known that a low-speed streak in wall turbulence is typically accompanied with a train of streamwise vortices elongated along the streak with alternate senses of rotation. Each vortex is slightly tilted downstream both radially (away from the pipe wall) and spanwisely (in such a way that the vorticity vector of the vortex be closer to that of the main flow) [Kim and Hussain(1993)]. In the present turbulent puff such typical structures of the low-speed streaks and the streamwise vortices are frequently observed. As an example, we take the low-speed streak sitting at the bottom of the eighth cross-section ($z = 7\pi$) of figure 3.3. The flow structure around this low-speed streak is shown in figure 3.6, where the regions of low axial velocity $u_z - \langle u_z \rangle_{\theta z} < 0.1$ is plotted by gray iso-surfaces, and those of high axial vorticity $|\omega_z| > 0.5$ by red and blue iso-surfaces for positive and negative values, respectively. Alphabets A, B, C and D identify the individual streamwise vortices. The region shown here is a semicircular cylinder of azimuthal angle between $\frac{7}{6}\pi \le \theta \le \frac{13}{6}\pi$ and axial coordinate between $6\pi \le z \le 7.5\pi$. The flow is directed from left to right. They are viewed (a) outward from the pipe axis and (b) inward from the pipe wall. Observe in (a) that the blue vortices (A and C) are inclined downward (to the negative azimuthal direction) toward downstream, whereas the red ones (B and D) inclined upward, and that the right vortex always behind the left one at their cross points. As stated above, this is the characteristics commonly observed in wall turbulence. The straight low-speed streak and accompanied streamwise vortices are more clearly seen in (b).

In figure 3.7, we plot the axial distribution of the mean friction $\langle \tau_w \rangle_\theta(z,t)$. It takes a maximum value in the puff where turbulence activity is high, and a

minimum value near upstream of the trailing edge where the low-speed streaks are well developed. This minimum position will be used as an indicator of the location of the puff (see figure 3.8 below).

3.2.3 Advection velocity of a puff

The above local region of high fluctuations of velocity is advected downstream with velocity close to the mean fluid velocity $\overline{u}_z$ throughout the computation time except for an initial transient period. Here, we estimate the advection velocity of a puff.

In figure 3.8 we plot, with + symbol, the temporal evolution of the minimal point of the mean wall-friction over $2000 \leq t \leq 3000$. The mean velocity averaged over this period is $U_P = 0.355$, which is a little smaller than the mean flow velocity $\overline{u}_z = 0.371$, so that $U_P = 0.96\overline{u}_z$. This compares with $U_P \approx \overline{u}_z$ obtained by DNS (Priymak and Miyazaki 2004) and $U_P = 0.9\overline{u}_z$ observed in experiments (Wygnanski and Champagne 1973).

The simple model (3.1) of a puff can be also used to calculate the temporal evolution of the trailing edge as well as the leading edge. In figure 3.9 we plot, in a moving frame ($z_p \equiv z - U_p t$) with the puff advection velocity U_P, the locations of the trailing edge (□) and the leading edge (△) together with the

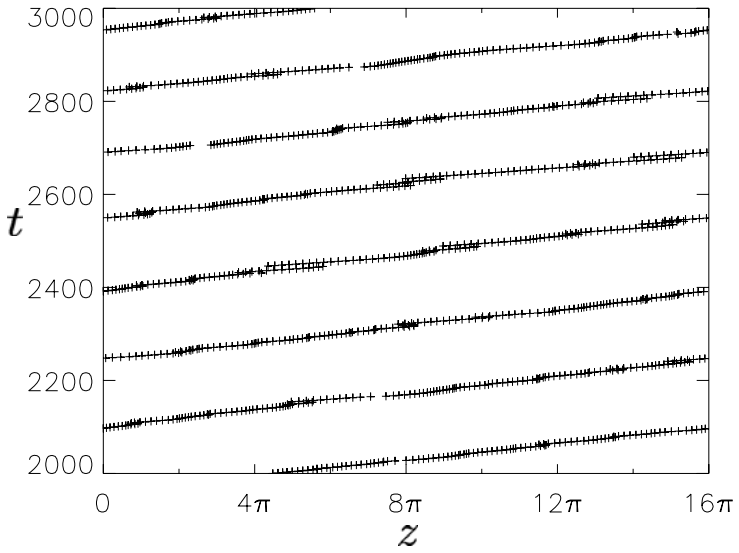

Figure 3.8: Temporal evolution of the minimal point of the mean wall-friction.

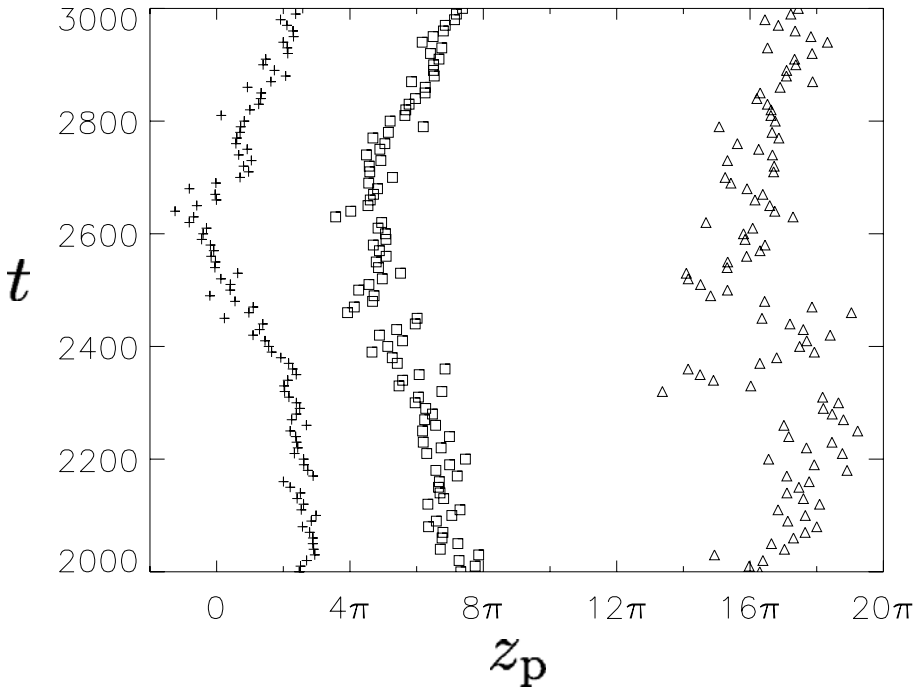

Figure 3.9: Movement of the leading edge (△), the trailing edge (□) and the friction minimal point (+).

minimal wall-friction (+) (obtained above, figure 3.8) every 10 time interval over period $2000 \leq t \leq 3000$. The friction minimal point and the trailing edge move similarly with the former being ahead of a constant distance (about 5π). Their advection speed is smaller (or larger) than the mean before (or after) $t = 2600$, synchronizing with deceleration (or acceleration) of the mean fluid velocity (see figure 3.1). Owing to the obscurity of the leading edge, the location of it is much more scattered compared with the other two. Nevertheless we may estimate the axial length of a puff as about $9\pi \sim 13\pi$.

3.2.4 Propagation velocity of fluctuation

As was shown in figure 3.2, the axial velocity $u_{zc}(z,t)$ in a puff typically exhibits a sharp drop at the upstream end (i.e. the trailing edge) and a gradual recovery toward downstream on the pipe axis. In figure 3.10 we plot three snapshots of $u_{zc}(z,t)$ with a larger time interval of 100. Observe that they are overall quite similar in height and extent as well as in the shape though the detailed variations are different among them. Such an overall similar structure is what we here call the 'puff'. As will be shown below, the advection velocity U_p of the puff can be also calculated by tracking such overall structure with neglecting the inner variations.

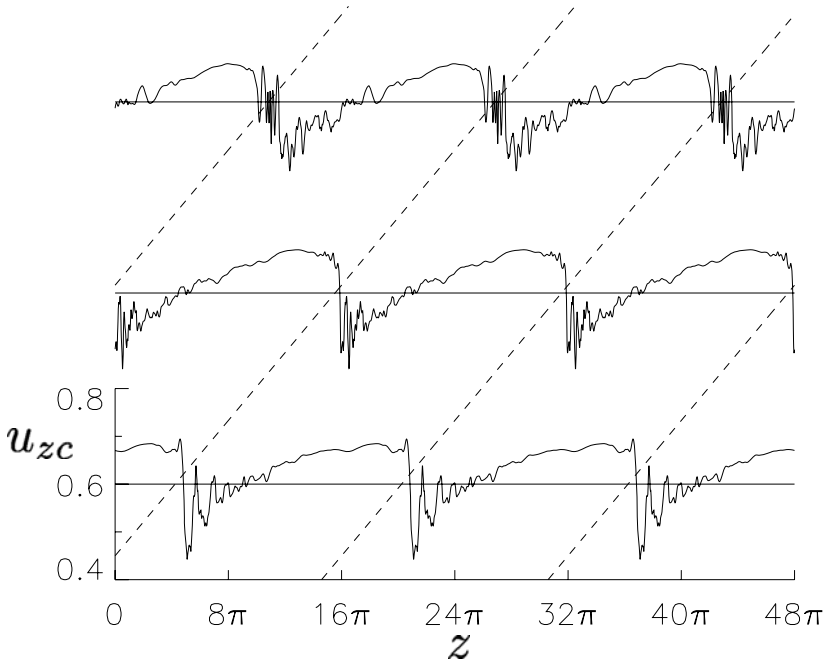

Figure 3.10: Temporal variation of the axial velocity field on the pipe axis. Three snapshots are plotted in the axial coordinate fixed to the pipe over three axial period. t = 2000, 2100, 2200 (from bottom to top). The straight lines show trajectories of the puff with mean advection velocity U_p = 0.355 of the puff

.

The motion of the inner fluctuations of the puff is visible in their short time sequence. In figure 3.11(a) we plot the contours of $u_{zc}(z,t)$ in the (z_p,t) plane. The level of gray scale varies between 0.4 and 0.8. The 0.6 level is drawn with black lines. The abscissa covers the whole computational domain. Since the puff is stationary in the mean in this moving coordinate, the contour lines are nearly vertical in the mean. Observe many stripes of slopes from right to left prominent around the puff (between the black lines, in particular). This indicates that the finer variations in $u_{zc}(z,t)$ propagate downstream relative to the puff. The slope of the stripes represents the propagation speed which is about 0.15 (compare with the slopes of two white straight lines inserted). In order to see the structure of finer fluctuation more clearly we plot, in figure 3.11(b), two consecutive snapshots of $u_{zc}(z,t)$ with small time interval of 5 in the moving frame z_p. They move as a whole to the right with changing their shape.

The temporal behaviours of the axial velocity $u_{zc}(z,t)$ on the pipe axis shown in figure 3.10 for larger time interval and in figure 3.11(b) for smaller time interval immediately suggest that both the advection velocity U_p of the puff and the propagation velocity (denoted by U_f below) of finer fluctuations may be estimated by comparing the shape of $u_{zc}(z,t)$ at two times separated by a long

time (of $O(100)$) and by a short time (of $O(10)$), respectively.

Let us consider the mean square difference in the axial velocity field $u_{zc}(z,t)$

(a)

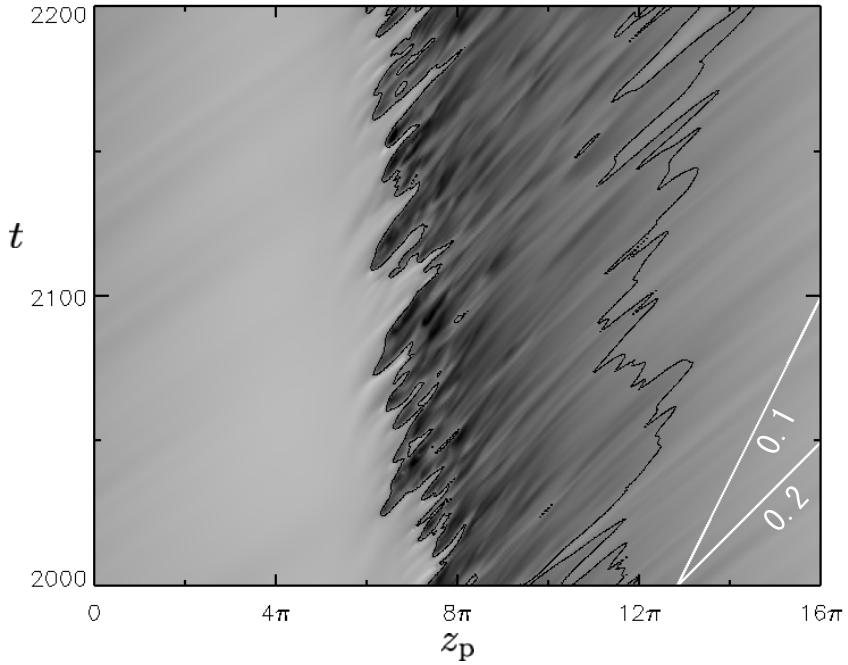

(b)

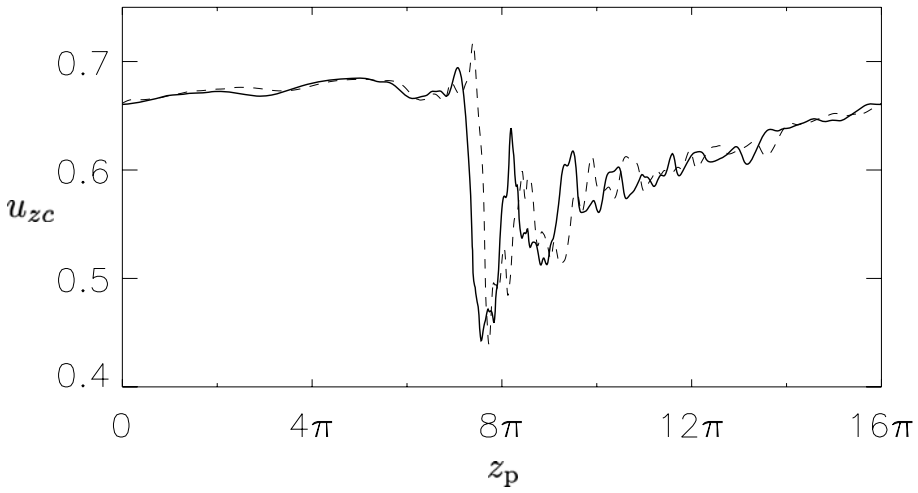

Figure 3.11: Time sequences of the axial velocity field on the pipe axis. (a) Contours of $u_{zc}(z,t)$ are plotted on (z_p,t) plane. The level of gray scale covers the range between 0.4 and 0.8. The 0.6 level is drawn with black lines. The white lines at the bottom-right corner represent slopes of trajectories of velocity 0.1 and 0.2. (b) Snapshots of $u_{zc}(z,t)$ at two consecutive times in a moving frame z_p. t = 2000 (solid line), 2005 (dashed line).

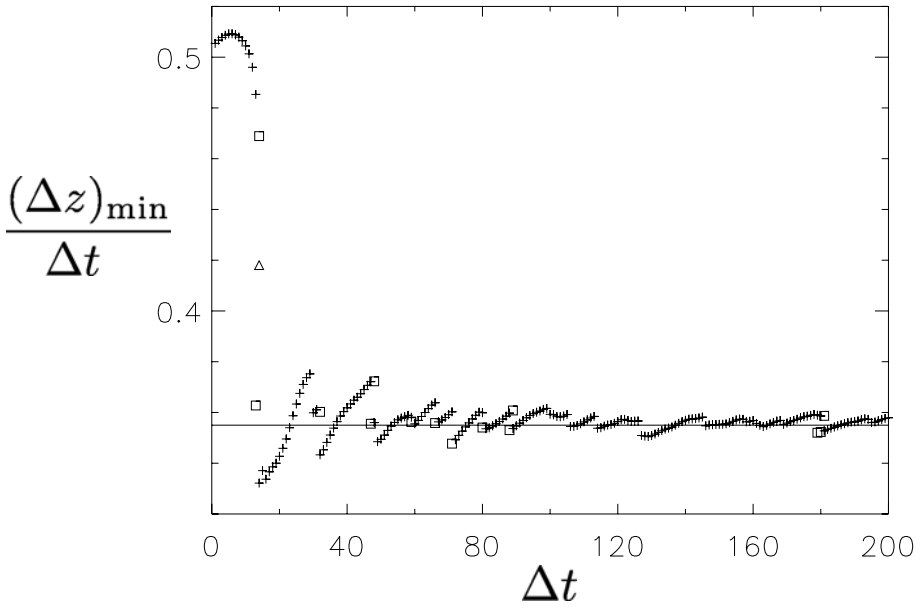

Figure 3.12: The ratio $(\Delta z)_{\min}/\Delta t$, represented by +, where $(\Delta z)_{\min}$ is the value of Δz which gives the minimum of mean square difference $D_{uc}(\Delta z, \Delta t)$ for a given Δt, changes drastically depending on the time difference Δt. For reference, the ratios estimated by the second and third minima are shown with □ and △. The propagation velocity $\langle U_f \rangle_z(0) = 0.505$ on the pipe axis of turbulent fluctuations is estimated by the ratio for smaller $\Delta t \ll (\Delta t)_c$ ($\approx 13 \sim 14$), For larger $\Delta t \gg (\Delta t)_c$, on the other hand, the ratio gives the advection velocity $U_P = 0.355$ (shown by a straight line) of the puff.

at two different space and time, separated by Δz in space and by Δt in time, namely,

$$D_{uc}(\Delta z, \Delta t) = \left\langle (u_{zc}(z,t) - u_{zc}(z+\Delta z, t+\Delta t))^2 \right\rangle_{zt}, \tag{3.2}$$

where $\langle \cdots \rangle_{zt}$ stands for the spatio-temporal average over the whole computational domain $0 \leq z < L$ for space and over the statistically steady period $2000 \leq t \leq 3000$ for time. It should be noticed here that we are assuming the smallness of the z dependence of the propagation velocity and that this assumption will be removed below (see equation (3.3)). It turns out that the variation of the propagation velocity is less than 3% (see figure 3.13 below). For a given Δt we expect that the function $D_{uc}(\Delta z, \Delta t)$ takes the minimum value for an appropriate shift Δz ($\equiv (\Delta z)_{\min}$ say). If Δt is small enough to capture the velocity fluctuations in the puff, the ratio $(\Delta z)_{\min}/\Delta t$ may yield the mean propagation velocity $\langle U_f \rangle_z(0)$ of the fluctuations. If, on the other hand, Δt is too large to see the coherent movement of finer fluctuations but small enough to capture the global structure of the puff, then the ratio may yield the puff advection velocity U_P.

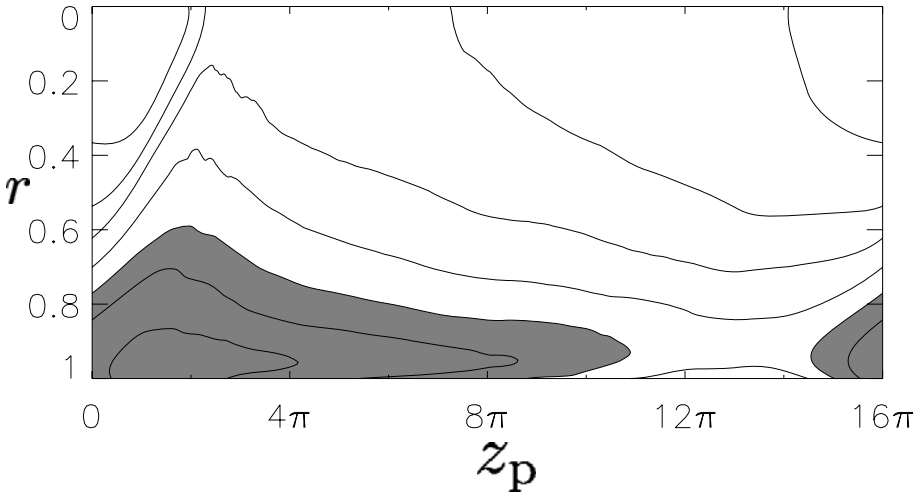

Figure 3.13: Propagation velocity $U_f(r,z) - U_P$, relative to the puff advection velocity, of turbulent fluctuations is shown by contours of levels -0.1, -0.05, 0, 0.05, 0.1, 0.15, 0.2 with negative parts shaded.

The ratio $(\Delta z)_{\min}/\Delta t$ thus obtained is plotted, in figure 3.12, with + symbol against Δt of 1, 2, $\cdots$, 200. Also shown here, for reference, with □ and △ are the ratios estimated by the second and third minimal points, respectively. The estimated velocity is a piecewise continuous function of Δt with jumps at a number of discrete points, where an exchange of the order of minimal points (i.e. + and □) takes place. The largest jump occurs at $\Delta t \equiv (\Delta t)_c$ ($= 13 \sim 14$). There are two important messages to be mentioned in this figure. Firstly, the estimated velocity are nearly constant for $\Delta t < (\Delta t)_c$ and takes the value of 0.505. This should be regarded as the mean propagation velocity $\langle U_f \rangle_z(0)$ of the turbulent fluctuations on the pipe axis. The slope of many stripes in figure 3.11(a) is therefore about 0.150 ($= \langle U_f \rangle_z(0) - U_P = 0.505 - 0.355$). Second, for $\Delta t > (\Delta t)_c$ the estimated velocity shows a complicated dependence on Δt, but it seems to converge to U_P (shown by a horizontal line) in the limit of large Δt.

Such a propagation velocity of fluctuation may be different from place to place in the cross-axial plane. The above idea for estimation of the propagation velocity of turbulent fluctuations on the pipe axis can be applied at other locations off axis as well. Although the instantaneous propagation velocity is not axi-symmetric, we focus our attention to the radial dependence by assuming that the azimuthal dependence may be averaged out in the mean over the statistically steady period $2000 \le t \le 3000$. Then, we consider the mean square difference in the axial velocity field $u_z(r,\theta,z,t)$ at two different space and time, separated by Δz in space and by Δt in time defined by

$$D_u(r,z,\Delta z,\Delta t)^{\delta z} = \left\langle (u_z(r,\theta,z,t) - u_z(r,\theta,z+\Delta z,t+\Delta t))^2 \right\rangle_{\theta t}^{\delta z}. \tag{3.3}$$

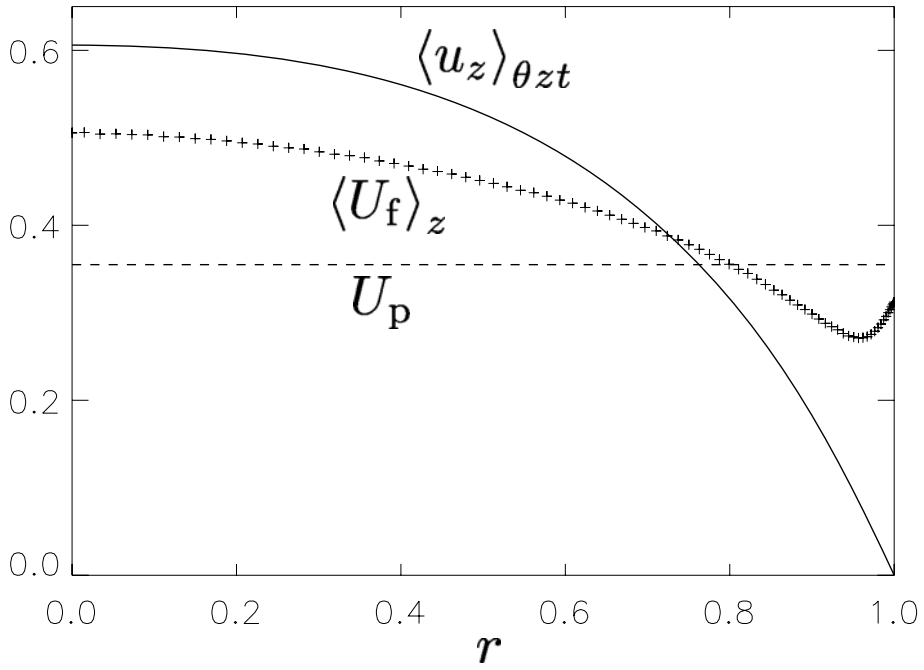

Figure 3.14: Comparison of three velocities. The mean fluid velocity $\langle u_z \rangle_{\theta,z,t}(r)$, the time-averaged advection velocity U_p of the puff and the mean propagation velocity $\langle U_f \rangle_z(r)$ of fluctuation are drawn with a thick line, a dashed line and plus symbols, respectively.

Here, $\langle \cdots \rangle_{\theta t}^{\delta z}$ stands for the spatio-temporal average over a limited axial domain between $z - \frac{1}{2}\delta z$ and $z + \frac{1}{2}\delta z$, the whole azimuthal angle $0 \le \theta < 2\pi$ and over the statistically steady period $2000 \le t \le 3000$. Smaller values of the axial band width δz is better for spatial resolution but more noisy. Here we set it as $\delta z = \pi$ by compromise.

In the same way as before the axial component of the propagation velocity $U_f(r, z)$ of turbulent fluctuations can be estimated by the ratio $(\Delta z)_{\min}/\Delta t$, where $(\Delta z)_{\min}$ is the value of Δz which gives the minimum of $D_u(r, z, \Delta z, \Delta t)^{\delta z}$ for given r, z, Δt $(= 1)$ and δt $(= \pi)$. The propagation velocity thus obtained is shown in figure 3.13(a) in the moving frame z_p by contours of gray scale with negative parts shaded. It is seen that the propagation velocity is positive in most of the interior of the puff ($6\pi \le z_p \le 17\pi$) except near the pipe wall and the trailing edge. This implies that turbulent fluctuations excited near-upstream of the trailing edge move downstream almost throughout the puff.

In figure 3.14 we compare three velocities; the mean fluid velocity $\langle u_z \rangle_{\theta zt}(r)$ (solid line), the puff advection velocity U_p (dashed line) and the mean propagation velocity $\langle U_f \rangle_z(r)$ (plus symbols) of turbulent fluctuations averaged over the axial coordinate z. It is seen that the fluctuations propagate downstream faster or slower than the puff itself in the inner region ($r < 0.81$) or near the pipe wall ($r > 0.81$), respectively. This dependence of the direction of the propagation velocity on the radial coordinate plays an important role in the self-sustenance cycle of a

puff (see the next section).

3.3 Puff dynamics

In the preceding section we have seen that an equilibrium puff is developed for $Re = 3000$. Although the size and the fluctuation magnitude are nearly stationary, the fine structure of a puff varies violently in space and in time. Here, we examine the self-sustenance cycle of a puff in terms of vortex dynamics.

3.3.1 Self-sustenance cycle

The self-sustenance cycle of an equilibrium puff we propose here is illustrated schematically in figure 3.15. Here, the turbulent region sandwiched by the leading edge and the trailing edge is an equilibrium puff which is advected to the right with nearly the mean fluid velocity hardly changing its size.

Before going into the details of the self-sustenance cycle, it may be convenient to summarize first the whole processes of it, which is:
(i) The turbulence in the puff creates low-speed streaks (accompanied with streamwise vortices) along the pipe wall in the same way as many kinds of wall turbulence, i.e. through the near-wall interaction.
(ii) These low-speed streaks move upstream relative to the puff and penetrate the trailing edge.
(iii) Near-upstream of the puff strong shear layers are created, arched over the low-speed streaks, between two counter flows, namely, the low-speed streaks and laminar flow coming down from far-upstream.
(iv) These shear layers are rolled up through the Kelvin-Helmholtz instability to create new fluctuations.
(v) The majority of these fluctuations propagate downstream faster than the puff, penetrate the trailing edge and enhance turbulent activity in the puff.
Then the process goes back to (i).

Note that the turbulence in the puff may be strong enough to make the low-speed streaks along the pipe wall, but too weak to extend the turbulent region because the Reynolds number is not large enough. Thus, an equilibrium puff results. In the following sections we consider the individual precesses in more detail.

3.3.2 Low-speed streaks

As commonly observed in wall-turbulence, there are many low-speed streaks accompanied with streamwise vortices (see figure 3.6 for an example) excited along the pipe wall. As discussed below, such low-speed streaks play a key role in the self-sustenance cycle of the puff. Since it is cyclic, we can start considering the self-sustenance cycle from any stage. Here, we tentatively assume the existence of turbulence together with low-speed streaks in the puff, leaving the driving mechanism of the turbulence (stage (iv) in self-sustenance cycle) in the next subsection.

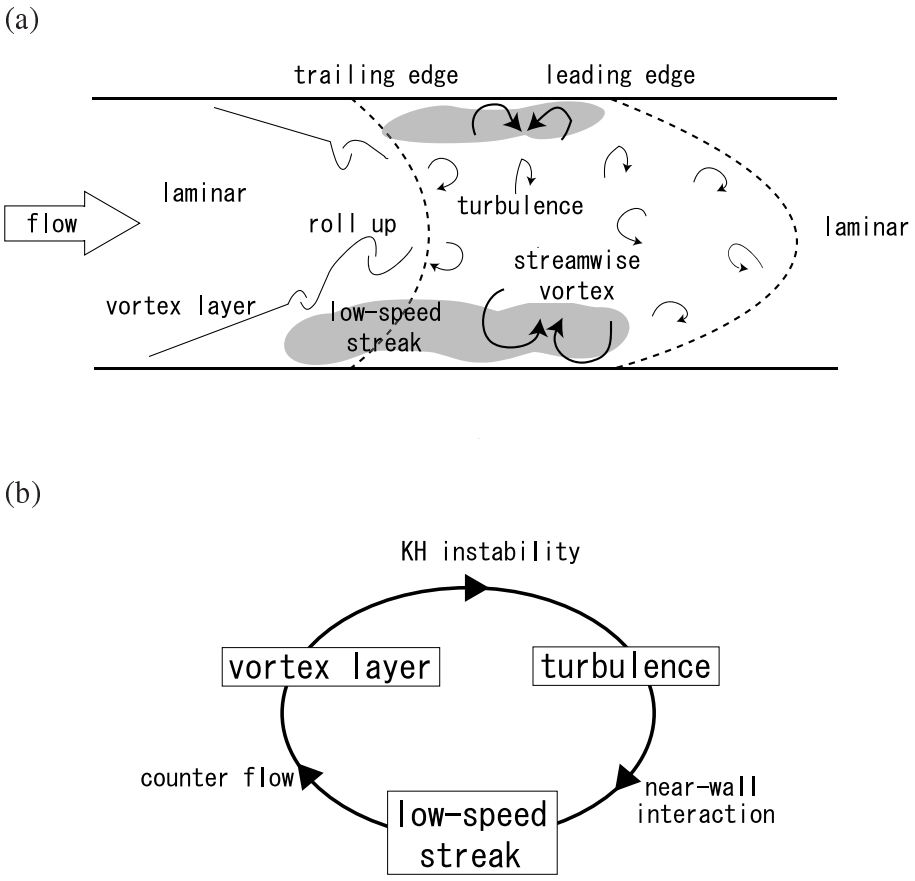

Figure 3.15: Self-sustenance cycle of an equilibrium puff. (a) Schematic of an equilibrium puff in pipe flow. The puff sandwiched by the leading edge and the trailing edge is advected with nearly the mean fluid velocity. The turbulent activity and the low-speed streaks in the puff as well as the vortex layer near-upstream of the trailing edge constitute a self-sustenance cycle together. (b) Key ingredients and actions in a self-sustenance cycle.

As will be discussed in the next subsection, the velocity fluctuations are created by roll-ups of vortex layers near-upstream of the trailing edge. In order to see how the fluctuations propagate in the puff we show in figure 3.16 the axial velocity field u_z on a (z_p, θ)-plane near the wall ($r = 0.81$). Here, the deviation of the axial velocity from the mean $u_z - \langle u_z \rangle_{\theta z}$ is shown by contours of gray scale with darker regions indicating the smaller values, i.e. the low-speed streaks. Time elapses from the top panel to the bottom by 10 time interval. The white lines, either thin solid or dotted, represent the minimal lines of the axial velocity field with respect to θ or z, respectively. Lowercase alphabets attached to some of the lines identify the individual ones at different times.

The movement of the flow pattern may be followed more easily with these discrete lines than with the continuous gray scale of contours. It is seen that the patterns upstream (resp. downstream) of the trailing edge ($z_p \approx 6\pi$) move upstream (resp. downstream). This is consistent with the propagation velocity shown in figure 3.13, where we see the velocity at $r = 0.81$ is positive for $10\pi < z_p < 15\pi$ and negative otherwise. This implies that the fluctuations created near-upstream of the trailing edge propagate both upstream and downstream relative to the puff.

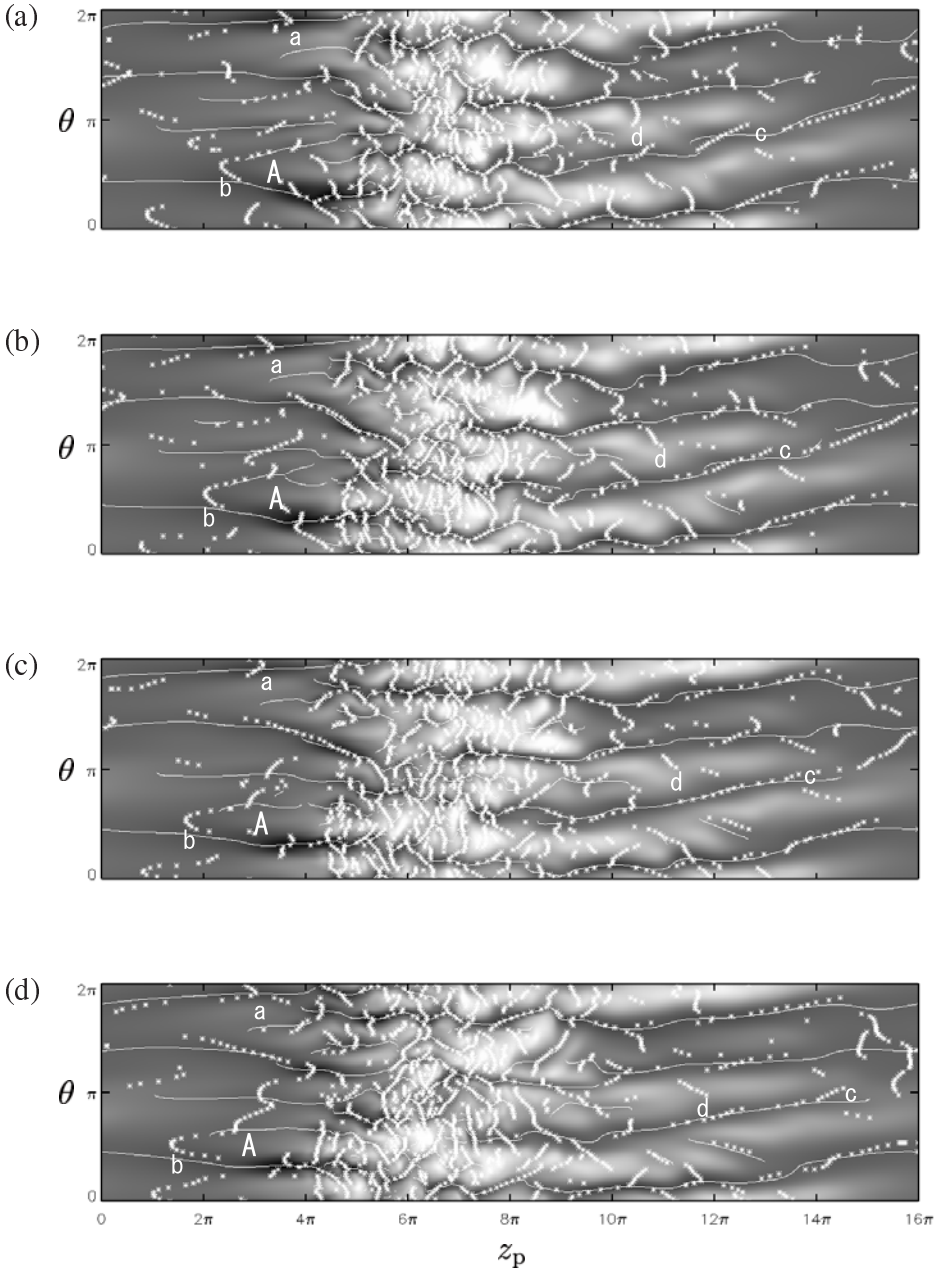

Figure 3.16: Propagation of flow pattern. The axial velocity $u_z - \langle u_z \rangle_{\theta z}$ is shown with contours of gray scale on the (z_p, θ)-plane near the wall (at $r = 0.81$). The velocity is smaller in darker areas, indicating the low-speed streaks. White thin solid and dotted lines represent the minimal lines with respect to θ and u_z, respectively. Lowercase alphabets identify some of the individual lines at different times. Capital A indicates a typical low-speed streak which is referred to in figure 3.17. (a) $t = 2260$, (b) 2270, (c) 2280 and (d) 2290.

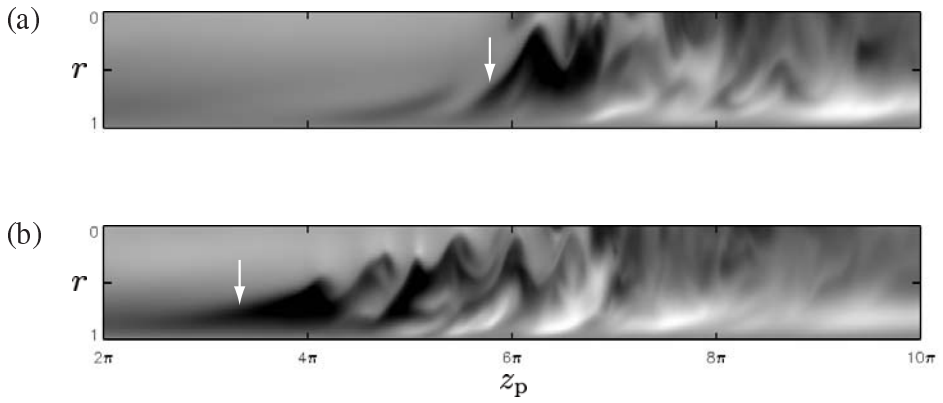

Figure 3.17: Generation of a vortex layer by counter flows. The axial velocity $u_z - \langle u_z \rangle_{\theta z}$ is shown with contours of gray scale on the (z_p, r)-plane of $\theta = \frac{5}{16}\pi$, which crosses the low-speed streak A in figure 3.16. The velocity is smaller in darker areas. The domain $(2\pi \leq z_p \leq 10\pi)$ shown is upstream of the trailing edge. Observe that the low-speed streak (dark gray area under the arrows) moves upstream (to the left) and encounter a laminar flow coming from far-upstream to make a vortex layer (a line of sharp contrast of gray) between them. (a) $t = 2200$ and (b) 2290.

Since the velocity of a low-speed streak is small by definition, it can easily leave out from a puff to upstream through the trailing edge. We show, in figure 3.17, two successive snapshots of the axial velocity on a (z_p, r)-plane which crosses the low-speed streak A in figure 3.16. The domain $(2\pi \leq z_p \leq 10\pi)$ shown here is upstream of the trailing edge. There are many wavy lines of the sharp contrast of gray which represent thin vortex layers created by two counter flows, i.e. the low-speed streak (darker area) from downstream and the laminar flow (lighter area) from far-upstream. Observe, in particular, that the dark region under arrows move upstream to make a strong vortex layer at the interface with the laminar flow.

It is known in a variety of wall turbulence that the low-speed streaks are generated along the wall with spanwise distance being about 100 times wall-friction length l_τ. Since the circumference of the pipe is $487 l_\tau$ in the present turbulent puff (see section 3.2.1), we may expect about 5 low-speed streaks near the pipe wall. The minimal lines of the axial velocity with respect to θ (the white thin solid lines in figure3.16) are an indicator of low-speed streaks. The number of the minimal lines near the pipe wall ($r = 0.81$) is counted at every z_p over the period $2000 \leq t \leq 3000$. In figure 3.18 we plot the relative population of the number of minimal lines against z_p. The numbers in the respective bands represent the number of minimal lines. Similar histograms are observed near the pipe wall ($0.81 \leq r \leq 0.999$) (figures omitted). Except the vicinity ($4\pi < z_p < 8\pi$) of the trailing edge there exist $2 \sim 6$ minimal lines. This suggests that the turbulence in the puff may be similar to the wall turbulence. Incidentally, the rapid increases in number of axial velocity between $4\pi < z_p < 8\pi$ reflect the violent motion generated by roll-ups of vortex layers discussed in the next section.

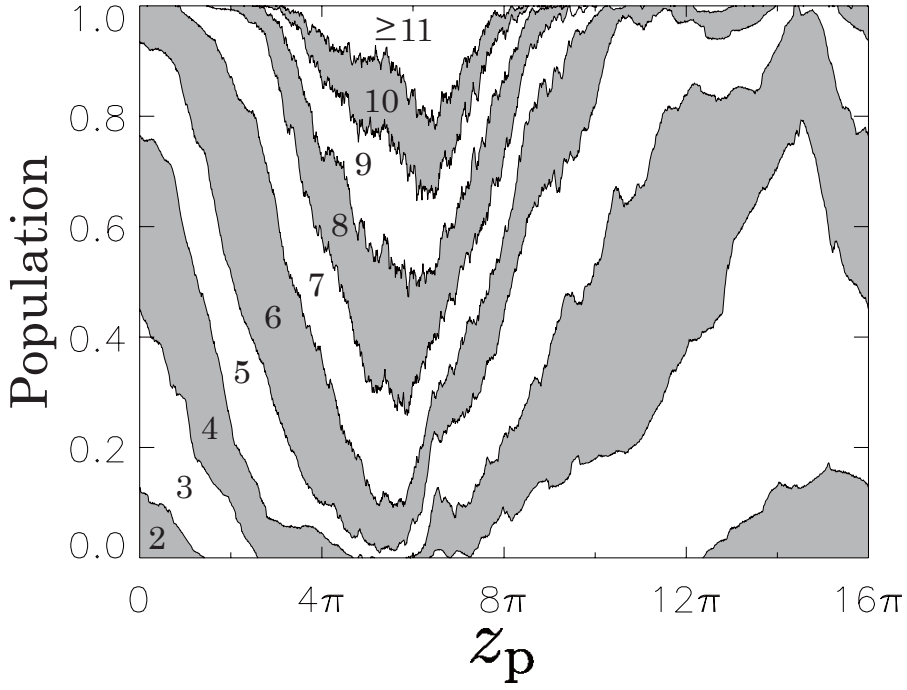

Figure 3.18: Relative population of minimal lines of axial velocity near the pipe wall ($r = 0.81$). The abscissa represents the axial coordinate z_p moving with the puff and the ordinate the relative population of the lateral numbers of the minimal lines of the axial velocity.

3.3.3 Roll-up of vortex layer

As seen in the preceding section, the low-speed streaks, which are generated in the puff, move upstream relative to the puff, cross the trailing edge, and leave out of the puff. The low-speed streak going up from downstream and the fast fluid flow coming down from upstream create strong thin vortex layers between them, arched over the streaks. These vortex layers are unstable to small disturbances, and easily roll up to generate stronger fluctuations in velocity.

Such roll-ups of vortex layers are taking place quite frequently near upstream of the trailing edge. As examples, we show, in figures 3.19 and 3.20, the vorticity field near the trailing edge in two arbitrary time periods, $2278 \leq t \leq 2290$ and $2450 \leq t \leq 2462$, respectively. Time elapses downward by 4 time interval. The fluid flows rightward. Here, the radial, the azimuthal and the axial components of vorticity field are plotted, on a cylinder of radius $r = 0.61$, with contours in the left, the center and the right columns, respectively. Light gray shows larger values. The ordinate covers the whole azimuthal coordinate, whereas the abscissa a part of the axial coordinate which moves with puff velocity U_P.

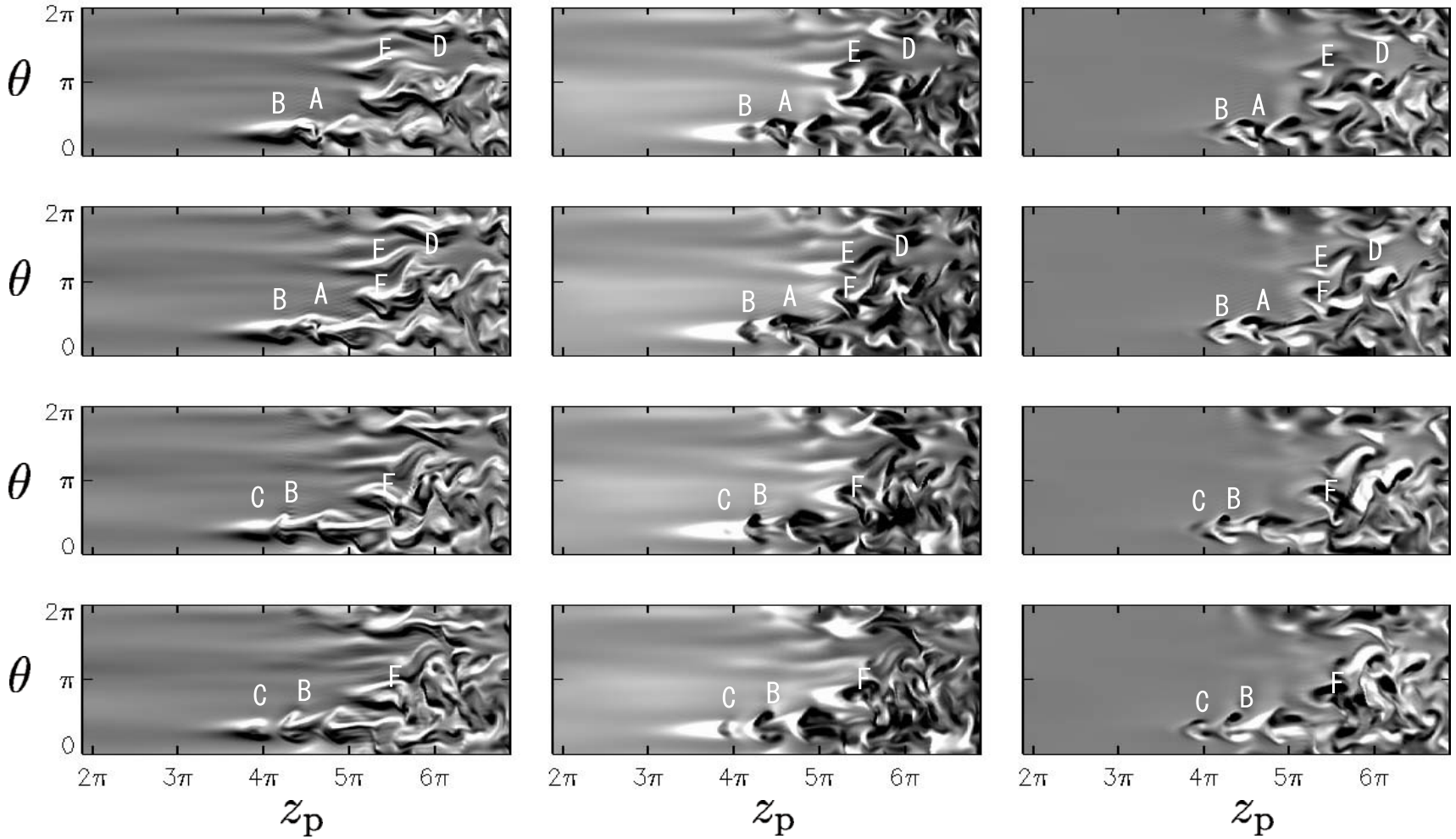

Figure 3.19: Vorticity field near-upstream of the trailing edge of a puff. The vorticity field is shown with gray scale on a cylinder of radius $r = 0.61$ for ω_r, ω_θ and ω_z in the left, the center and the right columns respectively. The abscissa and ordinate represent the axial and azimuthal coordinates, respectively. Flow is directed from left to right. Time elapses downward by 4 time interval from $t = 2278$ to 2290. Alphabets identify the individual roll-ups of vortex layers. See figure 3.20 for the scale bar.

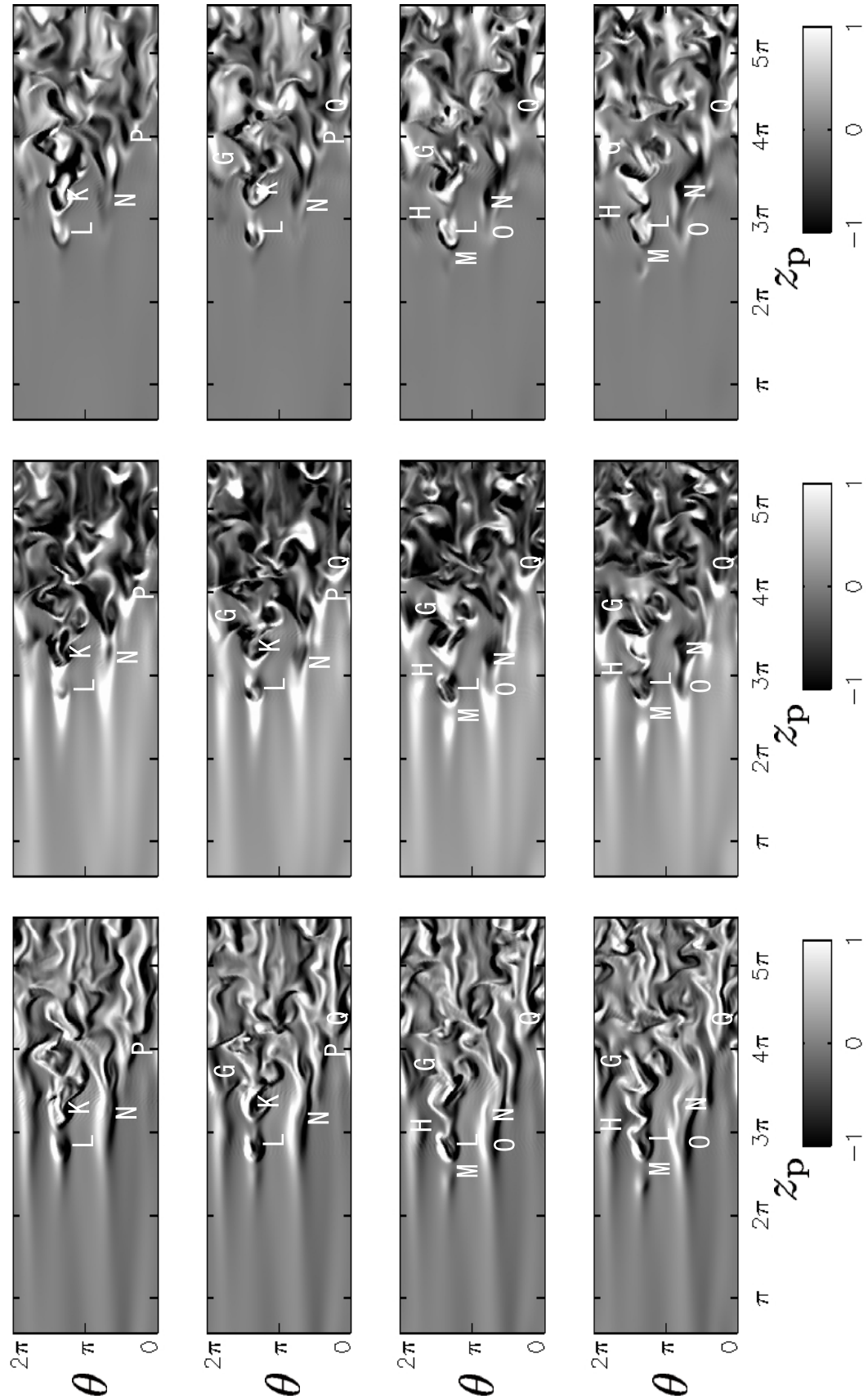

Figure 3.20: Same as figure 3.19 but for time period $2450 \leq t \leq 2462$.

At first glance we may recognize the following characteristics in these rather complicated contours. First, the trailing edge of the puff, i.e. the boundary between the laminar (gently fluctuating) region (in the left part of each panel) and the turbulent (violently fluctuating) region (in the right part) are clear and sharp though the shape is complicated and convoluted. Second, many contours have the form of left-facing wedges of various apex angles. Third, large variation of contour levels is aligned in parallel to the axial direction, and the number of stripes is roughly between 3 and 5. Fourth, there are repetitions of similar contour patters in the axial direction. Finally, although it is hard to identify in these still pictures, the most important (in the present study) events, which are the roll-ups of vortex layers, are taking place frequently here and there. By close observation of animations of these pictures, we identified a number of roll-up events as attached with alphabets A – F in figure 3.19 and G – Q in figure 3.20.

Among many events of roll-ups, we take the one attached with A, B and C in figure 3.19 as a typical example in the following discussion. As will be shown below, they constitute a sequence of vortex-layer roll-ups. They can be traced back easily to the top panel at $t = 2278$. Observe the similarity in a sequence of three roll-ups; A and B in the top panel correspond to B and C in the bottom respectively. The interval 12 (= 2290 – 2278) is roughly the roll-up period. The locations of successive roll-ups are shifted slightly to upstream relative to the puff and the size also decreases slightly. By comparing the corresponding contours in ω_r (left panel) and in ω_z (right panel) we find that this pattern has a symmetry with respect to a line parallel to the axial direction. More precisely, ω_r and ω_z are anti-symmetric, whereas ω_θ is symmetric. There are many examples of similar repetition events seen in these figures.

In figure 3.21, we show the temporal evolution of the azimuthal component $\omega_\theta(r, \theta, z; t)$ associated with roll-ups, A, B and C, in figure 3.19 on a diametral plane of $\theta = \frac{5}{16}\pi$ over time period $2270 \leq t \leq 2290$. This plane crosses a low-speed streak. The gray scale indicates the contours of ω_θ with lighter parts for larger values. The ordinate is the radial coordinate r, where the bottom line corresponds to the pipe wall. The abscissa is the axial coordinate z_p viewed in a moving frame with the mean puff velocity U_p. The flow is directed from left to right. Time elapses from (a) to (f) every 4 time interval. Many bright thin stripes are conspicuous which are vortex layers of positive ω_θ, or blobs of clockwise rotation. The slightly curved stripe upstream side hardly changes in time, whereas the complicated stripe pattern in the downstream changes rather violently. Alphabets A, B and C, which are the same as those in figure 3.19, identify the individual roll-ups of vortex sheets.

Let us compare these three roll-ups at their earlier stage of development, e.g. A in (a) and B in (d), and B in (c) and C in (f). It is impressive that the respective pairs are extremely similar in shape with each other. To be noted,

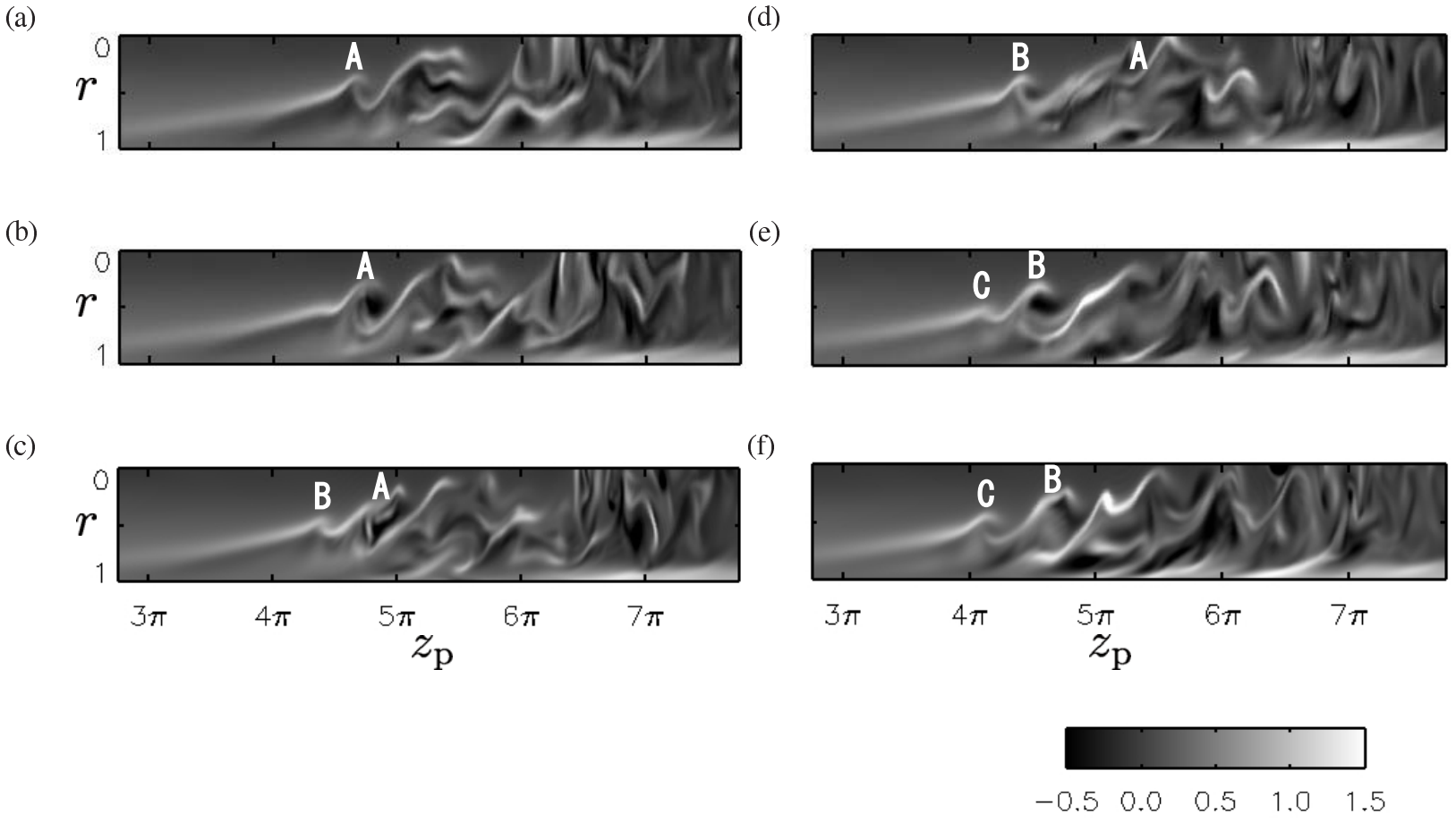

Figure 3.21: Roll-ups of vortex layer. The temporal variation of the azimuthal component ω_θ of vorticity is shown on a diametral plane passing through low-speed streak A in figure 3.16. The darkness of gray represents the value of ω_θ in the range $[-0.5 : 1.5]$ as shown in the scale bar. Time elapses from (a) to (f) by 4 time interval over the period $2270 \leq t \leq 2290$. The ordinate is the radial coordinate, whereas the abscissa is the axial z_p coordinate which moves with the puff. Alphabets A, B and C (same as in figure 3.19) identify the individual roll-ups of vortex layer. $\theta = \frac{5}{16}\pi$.

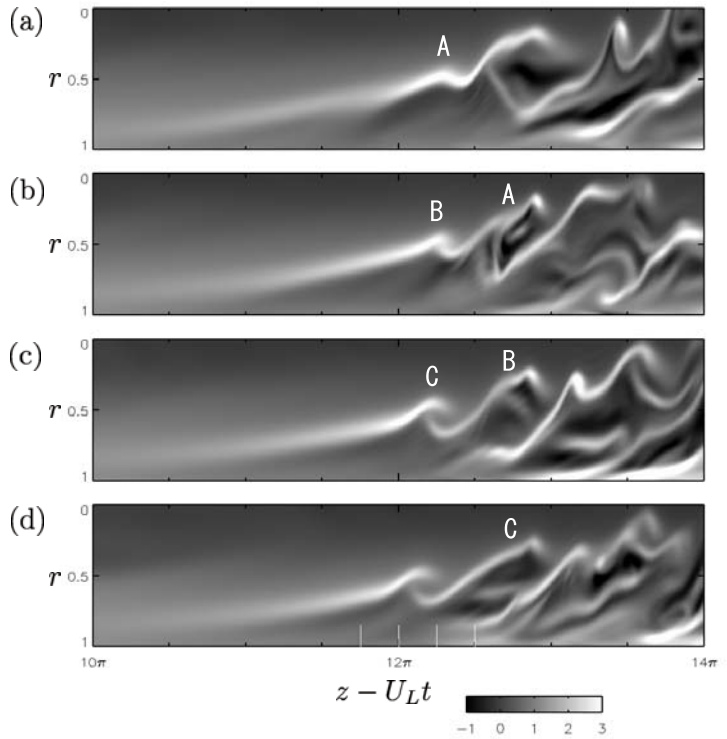

Figure 3.22: Four successive roll-ups of a vortex layer. The azimuthal component ω_θ of vorticity is plotted in the same manner as in figure 3.21 except for the abscissa being a moving coordinate, $z - U_L t$, on which the vortex layer in the upstream side is nearly stationary. $U_L = 0.3$. (a) $t = 2266$, (b) 2278, (c) 2290, (d) 2302.

however, is that a later roll-up occurs at more upstream and closer to the wall than an earlier one. This means that the roll-up process is not exactly periodic, but the period, which is about 12 between A and B, may get shorter one after another and that the roll-up process associated a low-speed streak should terminate after a finite time. The wavelength of the fluctuation, or the distance between the centers of successive roll-ups. is about 0.5π as seen in figure 3.21 as well as in contours A, B and C for ω_θ and ω_z in figure 3.19.

In order to see the quasi-periodic roll-ups over a longer period of time we show, in figure 3.22, four snapshots of ω_θ-field at nearly the same phase of the period, namely, every 12 time interval. The ordinate is the same radial coordinate r as figure 3.21 but the abscissa moves with velocity U_L so that the nearly straight stripe of the vortex layer in the upstream may be as stationary as possible. Note that although the roll-up pattern is similar, the fluctuation pattern is quite different from period to period even only a few wavelengths downstream. This suggests that the flow field is quite random in the puff.

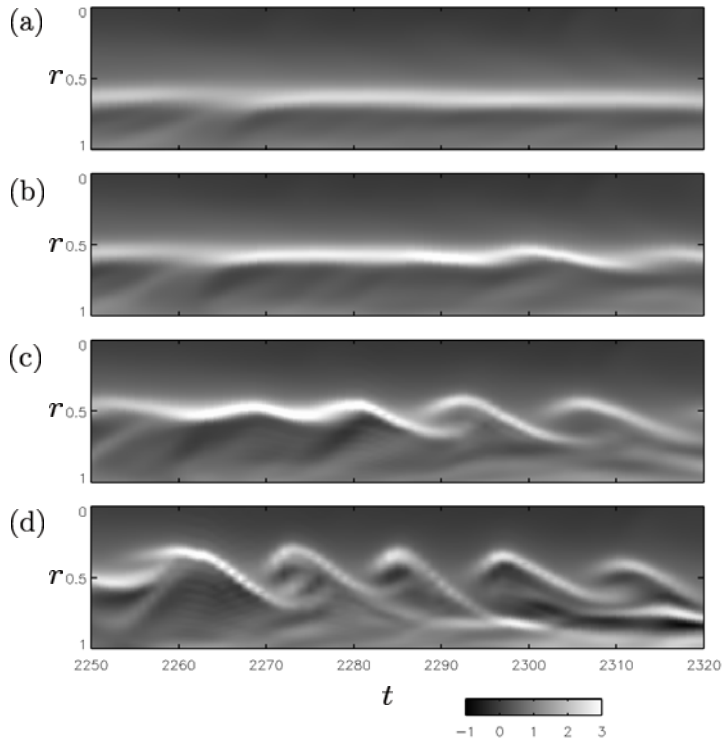

Figure 3.23: Oscillation of vortex layer. Temporal variation of the azimuthal component ω_θ of vorticity is shown in the (r, t) plane at (a) $z - U_L t = 11.75\pi$, (b) 12.00π, (c) 12.25π, (d) 12.50π. $U_L = 0.3$.

By construction, the shape of ω_θ in the upstream part is seen invariant in time in the coordinate adopted in the left column of figure 3.22. We show, in figure 3.23, the ω_θ-field on the (r, t)-plane at four axial positions; (a) $z - U_L t = 11.75\pi$, (b) 12π, (c) 12.25π, (d) 12.5π (see white lines in figure 3.22 (d)). The contours in (a) are almost horizontal, meaning that the vortex layer is hardly disturbed at this upstream location. Oscillations in contours are recognized in (b), (c) and (d), and the amplitude increases in this order. This indicates that the vortex roll-ups take place close to the location of panel (b). The time period of oscillation is estimated by inspection, from figure 3.23(d), as about 12.

We have seen in figures 3.22–3.23 a series of roll-ups of the longitudinal cross-section of a vortex layer arched over a low-speed streak. In order to see the three-dimensional structure we show in figure 3.24 the temporal evolution of the round-cut as well as the longitudinal cross-section over the same time-period as figures 3.21(c)-(f). Here, the vorticity magnitude is shown with grayscale, brighter parts being larger values. Alphabets A, B and C identify the corresponding roll-ups. Vertical white lines in the longitudinal cross-sections indicate the axial position of the round-cuts. The vertical line in the round-cuts, on the other hand, indicates the cross-section of the upper panel. As seen in the left-most round-cut, a thin vortex layer of finite width sits over the low-speed streak. We observe the strong vorticity along the wall except for

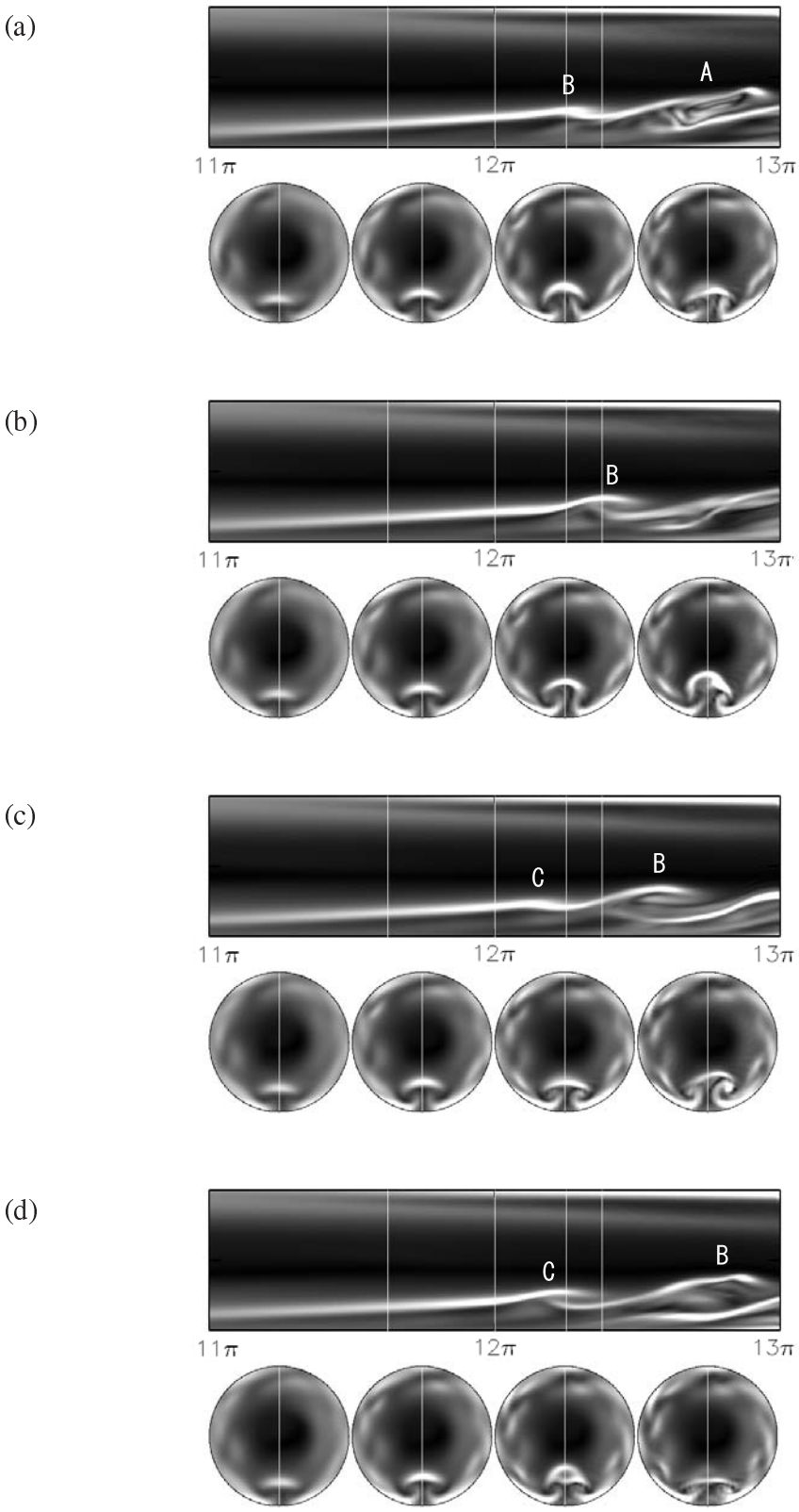

Figure 3.24: Temporal evolution of a vortex layer arched over a low-speed streak is shown in a longitudinal cross-section through the streak (upper panel) and in four round-cuts (lower panel). Vertical white lines in the upper panel indicate the axial positions of the round cuts, whereas those in the round cuts indicate the azimuthal position of the longitudinal cross-section. t = (a) 2278, (b) 2282, (c) 2286, (d) 2290.

the low-speed streak region. The roll-up of vortex layer takes place at the position of the third round-cuts from the left. The roll-up is thought as to be essentially the Kelvin-Helmholtz instability because the thichness of the vortex layer is several times smaller than the width. We do believe that this periodic roll-up is essentially the same as the periodic phenomenon observed experimentally, and named as wake-like structure, by Bandyopadhyay (1986).

The above vortex-layer roll-up may be reasonably understood as the Kelvin-Helmholtz instability. In order to examine it we show, in figure 3.25, the temporal evolution of the undisturbed part of the concerned vortex layer (roughly the left half of each panel in figure 3.22). Here, (a) the axial velocity u_z and (b) the azimuthal vorticity ω_θ against the radial coordinate are plotted with solid lines at $z - U_L t = 10\pi, 10.25\pi, \cdots, 12\pi$ from right to left, respectively. Each curve is obtained by taking an arithmetic average over $2260 \leq t \leq 2310$ (about four time period of the roll-ups). It is seen in (a) that as we move downstream (from right to left curves), a parabolic velocity profile changes into the one having a dent. It is locally approximated by a tanh profile which is shown with a line of pluses (at $z - U_L = 11.5\pi$) and of crosses (at $z - U_L = 12\pi$). Correspondingly, we see in (b) that a small bump at the most-upstream in the azimuthal vorticity distribution becomes narrower and higher downstream and that the vorticity profile locally approximated by a $\cosh^{-2}$ function (a line of pluses and crosses).

The linear stability of a tanh type of velocity profile was studied by Betchov and Szewczyk (1963). For a two-dimensional flow of an incompressible viscous fluid ($u(x,y)$, $v(x,y)$) with $u = U_0 \tanh(y/L_0)$ and $v = 0$, where U_0 and L_0 are constants they performed the linear stability analysis and obtained the neutral curves as functions of the Reynolds number $R_0 = U_0 L_0/\nu$ (see figure 1 in Betchov and Szewczyk (1963)). The phase velocity for the critical mode is identically zero. For the present data we find $U_0 = 0.2$ and $L_0 = 0.1$ (see figure 3.25), then $R_0 = 60$ because $\nu = 1/3000$ in this scaling. According to Betchov and Szewczyk (1963), around $R_0 = 60$, the wavenumber α of the most unstable mode multiplied by L_0 is about 0.4, and therefore the wavelength $\lambda = 2\pi/\alpha \approx 0.5\pi$. This agrees excellently with the value estimated from the roll-up sequence in figure 3.19. Concerning the phase velocity of fluctuation we read it as 0.32 in figure 3.25. On the other hand, the time period of fluctuation is about 12 in figure 3.23, implying that the fluctuation propagates with velocity $0.5\pi/12 = 0.13$ in this coordinate system because the wavelength is 0.5π. Since this coordinate system is moving with velocity of 0.3 relative to the pipe, the phase velocity of fluctuation is estimated as $0.13 + 0.3 = 0.43$, which is a bit smaller than 0.32.

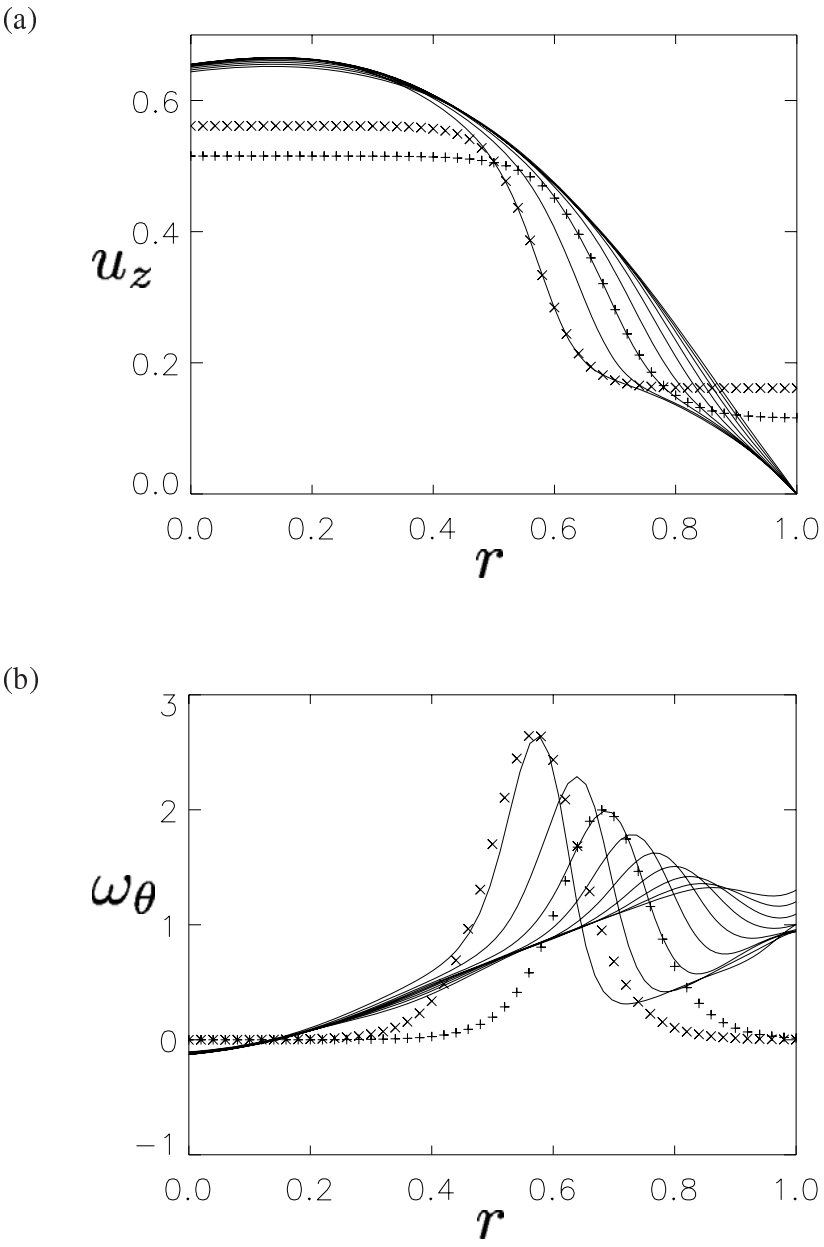

Figure 3.25: Mean profile of (a) the axial velocity u_z and (b) the azimuthal vorticity ω_θ near-upstream of vortex-layer roll-up. Nine solid curves in each panel represent the profiles at $z - U_L t = 10\pi, 10.25\pi, \cdots, 12\pi$ from right to left, respectively, where $U_L = 0.3$. Each curve is obtained by taking an arithmetic average over $2260 \le t \le 2310$ (about four time period). A model profile, $U_0 \tanh((r - r_0)/L_0) + u_0$ for velocity and the minus of its derivative $-(U_0/L_0)\cosh^{-2}((r - r_0)/L_0)$ for vorticity, are shown with cross and plus points. Here, $(r_0, u_0) = (0.68, 0.32)$ is an inflexion point of the velocity profile and $L_0 = 0.1$ at $z - U_L t = 11.5\pi$ (plus points), whereas $(r_0, u_0) = (0.57, 0.361)$ and $L_0 = 0.075$ at $z - U_L t = 12\pi$ (cross points). $U_0 = 0.2$ is common for the two curves.

3.4 Concluding remarks

We have investigated a turbulent puff in pipe flow driven by a constant uniform external force. The Navier-Stokes equation was solved numerically as the initial value problem starting with the Hagen-Poiseuille flow superposed by a perturbation of finite amplitude. The periodic boundary condition with period $16\pi a$, where a is the pipe radius, was imposed in the axial direction and the non-slip boundary condition on the pipe wall. An equilibrium puff was realized, and the flow characteristics, such as the spatial structure and the advection velocity of the puff as well as the propagation velocity of turbulent fluctuations, were analyzed in detail. The self-sustenance cycle of the puff was identified, in which the Kelvin-Helmholtz instability of vortex layers, arched over low-speed streaks, near-upstream of the trailing edge play an important role in enhancing the activity of the puff.

The turbulence puff in pipe flow has at least two important aspects in the fluid dynamics phenomena. One is related with the laminar/turbulent transition of pipe flows. As stated in the introduction, it is the existence of non-trivial solutions, such as the travelling-wave solutions and the unstable periodic flows, other than the Hagen-Poiseuille flow that determines the lower critical Reynolds number. The turbulent puff is one of plausible candidates for such non-trivial solutions. The other is connected with the turbulence dynamics in pipe flow. Since the generation mechanism of turbulent activity near the wall is common to many kinds of wall turbulence, the self-sustenance cycle revealed in the present paper may serve as a prototype of it. A comparison study with the fully developed turbulence in pipe flows is waited for.

In the present numerical simulation the axial period was taken as $16\pi a$, close to the minimal length required for the existence of a puff. Indeed an equilibrium puff of axial length of about $11\pi a$ was realized in this period, but it is necessary to examine the effects of the periodic boundary condition by increasing the period. Since a turbulent puff depends sensitively on the control parameters, such as the initial condition, the axial period, the numerical scheme, etc., it is not guaranteed that the puff we have observed in this paper survives for ever. A careful consideration on this aspect is necessary. The external forcing is another matter to be examined. In the present numerical simulation the flow is driven by a constant external force, and so the mean axial velocity changes in time. If, on the other hand, an external force is adjusted in such a way that the mean flux be invariant in time, do we observe a different behaviour of the flow ? These fundamental questions are left for our next targets of research.

Chapter 4

Numerical method

In this chapter we present the spectral sover for pipe flow which we use for the numerical simullations in preceding chapters. In using cylindrical coordinate, the difficulty is the treatment of the coordinate singularity along z axis. However we overcome this difficulty by using the Zernike circular polynomials. With the use of those polynomials, the spectral representations remain analytic along the z axis.

4.1 Basic equations

As mentioned in preceeding chapter, we recall here the equations for motion of fluid in a pipe driven by constant external force. The fluid is assumed imcompressible Newtorian fluid. The boundary conditions at the wall are non-slip conditions and these for z direction are periodic conditions of period L. Then the equations become

$$\frac{\partial \boldsymbol{u}}{\partial t} + (\boldsymbol{u} \cdot \nabla)\boldsymbol{u} = -\nabla p + \frac{1}{Re}\nabla^2 \boldsymbol{u} + \frac{4}{Re}\widehat{\boldsymbol{z}}, \tag{4.1}$$

$$\nabla \cdot \boldsymbol{u} = 0, \tag{4.2}$$

$$\boldsymbol{u}(1, \theta, z) = 0, \tag{4.3}$$

$$\boldsymbol{u}(r, \theta, z + L) = \boldsymbol{u}(r, \theta, z). \tag{4.4}$$

The curl of eq.(4.1) leads to the vorticity equation

$$\frac{\partial \omega}{\partial t} = \nabla \times (\boldsymbol{u} \times \omega) + \frac{1}{Re}\nabla^2 \omega. \tag{4.5}$$

From the solenoidal condition, $\boldsymbol{u}$ can be represented by two scalar functions as

$$\boldsymbol{u} = \nabla \times (\psi\widehat{\boldsymbol{z}}) + \nabla \times (\nabla \times (\phi\widehat{\boldsymbol{z}})), \tag{4.6}$$

where ψ and ϕ are called toroidal and poloidal functions respectively. These scalar functions have gauge freedom, so we take the following gauge to define these functions uniquely as

$$\int_0^{2\pi} \psi|_{r=1} d\theta = 0, \tag{4.7}$$

$$\phi|_{r=1} = 0. \tag{4.8}$$

The non-slip boundary conditions (4.3) are written as

$$\left.\frac{\partial\psi}{\partial\theta}\right|_{r=1} + \mathcal{D}\left.\frac{\partial\phi}{\partial z}\right|_{r=1} = 0, \tag{4.9a}$$

$$\left.\mathcal{D}\psi\right|_{r=1} = 0, \tag{4.9b}$$

$$\left.\mathcal{D}^2\phi\right|_{r=1} = 0, \tag{4.9c}$$

where $\mathcal{D} = r\frac{\partial}{\partial r}$, and the periodic conditions (4.4) are

$$\psi(\boldsymbol{r} + L\widehat{z}) = \psi(\boldsymbol{r}), \tag{4.10a}$$

$$\phi(\boldsymbol{r} + L\widehat{z}) = \phi(\boldsymbol{r}). \tag{4.10b}$$

By taking the z component of eq.(4.5) and the z component of the curl of it, we can obtain the evolution equations for ψ and ϕ

$$\nabla_\perp^2\left(\nabla^2 - Re\frac{\partial}{\partial t}\right)\psi = Re(\nabla\times\boldsymbol{N})\cdot\widehat{z}, \tag{4.11}$$

$$\nabla_\perp^2\left(\nabla^2 - Re\frac{\partial}{\partial t}\right)\nabla^2\phi = -Re\,(\nabla\times(\nabla\times\boldsymbol{N}))\cdot\widehat{z}, \tag{4.12}$$

where $\nabla_\perp^2 = \nabla^2 - \frac{\partial^2}{\partial z^2}$ and $N = \boldsymbol{u}\times\boldsymbol{\omega}$. Furthermore by imposing additionnal boundary condition, the radial component of eq.(4.5) at the wall,

$$\mathcal{D}\frac{\partial}{\partial z}\nabla_\perp^2\psi\Big|_{r=1} - \mathcal{D}^2\frac{\partial}{\partial\theta}\nabla_\perp^2\phi\Big|_{r=1} = 0, \tag{4.13}$$

the equations (4.11) and (4.12) become equivalent to the vorticity equation (4.5) [Marqués (1990)].

The equation for the mean velocity is written as

$$-\frac{1}{\pi L}\int_0^L\int_0^{2\pi}\frac{\partial}{\partial t}\mathcal{D}\phi|_{r=1}\mathrm{d}\theta\mathrm{d}z = -\frac{1}{\pi LRe}\int_0^L\int_0^{2\pi}\mathcal{D}^3\phi|_{r=1}\mathrm{d}\theta\mathrm{d}z + \frac{4}{Re}. \tag{4.14}$$

Then the governing equations (4.11) and (4.12) with the boundary conditions (4.9), (4.10), (4.5) and (4.14) are equivalent to the equations (4.1)-(4.4).

4.2 Spectral expansion

If we assume $f(r,\theta,z)$ is C^∞ function, f is represented as a Fourier series in the periodic directions, θ and z,

$$f(r,\theta,z) = \sum_{k=-\infty}^{\infty}\sum_{m=-\infty}^{\infty}\widetilde{f}_{mk}(r)e^{im\theta}e^{i(2\pi k/L)z}. \tag{4.15}$$

In Cartesian coordinate system, such that $x = r\cos\theta$ and $y = r\sin\theta$, f can be expanded in Taylor series along the z axis,

$$f(r,\theta,z) = \sum_{k=-\infty}^{\infty}\sum_{a=-\infty}^{\infty}\sum_{b=-\infty}^{\infty} \check{f}_{abk} x^a y^b e^{i(2\pi k/L)z} \tag{4.16}$$

$$= \sum_{k=-\infty}^{\infty}\sum_{m=-\infty}^{\infty}\sum_{\substack{p=0 \\ p=\text{even}}}^{\infty} \check{f}_{pmk} r^{|m|+p} e^{im\theta} e^{i(2\pi k/L)z}. \tag{4.17}$$

As a convenient expansion set in r direction , a orthogonal relation is desired. Then orthogonal sets of polynomials are constructed as followings. Let $\Phi_n^m(r)$ be a polynomial which consists of $r^{|m|}, r^{|m|+2}, \ldots, r^n$ terms:

$$\Phi_n^m(r) = \sum_{\substack{p=0 \\ p=\text{even}}}^{n-|m|} c_{np} r^{|m|+p} \quad (n \geq |m|, n+|m| = \text{even}). \tag{4.18}$$

We request the orthogonal relationships with respect to the weight function

$$w(r) = \frac{r^\beta}{(1-r^2)^{1-\alpha}}, \tag{4.19}$$

where $0 < \alpha \leq 1$ and β is a positive integer. Then the orthogonal relationships are written as

$$\int_0^1 \Phi_n^m \Phi_{n'}^m w dr = \delta_{nn'}. \tag{4.20}$$

If $\alpha = \beta = 1$, the weight function become $w = r$ and it seem to be suitable to the cylindrical coordinate. In this particular case Φ_n^m are called Zernike circular polynomials [Bhatia and Born (1954), Matsushima and Marcus (1995), Verkley (1997)]. So we take $\alpha = \beta = 1$ for the numerical simulation of pipe flow.

These sets of polynomials satisfy the singular Sturm-Liouville equation,

$$\frac{(1-r^2)^{1-\alpha}}{r^\beta}\frac{d}{dr}\left((1-r^2)^\alpha r^\beta \frac{d}{dr}\right)\Phi_n^m - \frac{|m|(|m|+\beta-1)}{r^2}\Phi_n^m + n(n+2\alpha+\beta-1)\Phi_n^m = 0. \tag{4.21}$$

Using these polynomials, eq.(4.17) can be written as

$$f(r,\theta,z) = \sum_{k=-\infty}^{\infty}\sum_{m=-\infty}^{\infty}\sum_{\substack{n=|m| \\ n+m=\text{even}}}^{\infty} \hat{f}_{nmk} \Phi_n^m e^{im\theta} e^{i(2\pi k/L)z}. \tag{4.22}$$

The coefficients f_n^{mk} are represented as

$$\hat{f}_{nmk} = \frac{1}{2\pi}\int_0^L \int_0^{2\pi} \int_0^1 f \Phi_n^m e^{-im\theta} e^{-i(2\pi k/L)z} dr d\theta dz. \tag{4.23}$$

Repeating the integration by parts with respect to r, θ and z respectively, we obtain

$$\hat{f}_{nmk} = \frac{1}{2\pi n^a (n+2\alpha+\beta-1)^a (im)^b (i(2\pi k/L))^c}\int_0^L \int_0^{2\pi} \int_0^1 \left(\mathcal{L}\frac{\partial^b}{\partial\theta^b}\frac{\partial^c}{\partial z^c} f\right)\Phi_n^m e^{-im\theta} e^{-i(2\pi k/L)z} dr d\theta dz, \tag{4.24}$$

where $2a$,$2b$ and $2c$ represent the freqency of the integration by parts with respect to r, θ and z respectively, and

$$\mathcal{L} \equiv \frac{(1-r^2)^{1-\alpha}}{r^\beta}\frac{d}{dr}\left((1-r^2)^\alpha r^\beta \frac{d}{dr}\right) - \frac{|m|(|m|+\beta-1)}{r^2}. \tag{4.25}$$

Then we can prove that for arbitrary integer a, b abd c,

$$\hat{f}_{nmk} = O(n^{-2a}m^{-b}k^{-c}). \tag{4.26}$$

Thus the convergence of this expansion is faster than any algebraic.

For numerical simulation the partial sum approximation to f is adopted:

$$f(r,\theta,z) = \sum_{k=-K}^{K}\sum_{m=-M}^{M}\sum_{\substack{n=|m| \\ n+m=\text{even}}}^{N} \hat{f}_{nmk}\Phi_n^m e^{im\theta}e^{i(2\pi k/L)z}, \tag{4.27}$$

where N,M and K are maximum wave numbers of r,θ and z directions respectively.

4.3 Method of integration

The toroidal and poloidal function are represented in Fourier series as

$$\begin{pmatrix}\psi(r,\theta,z)\\ \phi(r,\theta,z)\end{pmatrix} = \sum_{k=-K}^{K}\sum_{m=-M}^{M}\begin{pmatrix}\widetilde{\psi}_{mk}(r)\\ \widetilde{\phi}_{mk}(r)\end{pmatrix}\exp[\mathrm{i}(m\theta+(2\pi/L)kz)]. \tag{4.28}$$

Substitution of this form to eq.(4.11) and (4.12), we can obtain the evolution equations of Fourier coefficients,

$$\mathcal{H}_{m0}\left(\mathcal{H}_{mk} - Re\frac{\partial}{\partial t}\right)\widetilde{\psi}_{mk} = \frac{Re}{r^2}\left(\mathcal{D}(r\widetilde{N}_{\theta,mk}) - \mathrm{i}m(r\widetilde{N}_{r,mk})\right), \tag{4.29}$$

$$\begin{aligned}\mathcal{H}_{m0}\left(\mathcal{H}_{mk} - Re\frac{\partial}{\partial t}\right)\mathcal{H}_{mk}\widetilde{\phi}_{mk} &= \frac{Re}{r^2}\left(\mathcal{D}^2 - m^2\right)\widetilde{N}_{z,mk} \\ &\quad -\frac{Re}{r^2}\frac{2\pi\mathrm{i}k}{L}\left(\mathcal{D}(r\widetilde{N}_{r,mk}) + \mathrm{i}m(r\widetilde{N}_{\theta,mk})\right),\end{aligned} \tag{4.30}$$

where $\widetilde{N}_{r,mk}$, $\widetilde{N}_{\theta,mk}$, $\widetilde{N}_{z,mk}$ are the coefficient of

$$N(r,\theta,z) = \sum_{m=-M}^{M}\sum_{k=-K}^{K}\widetilde{N}_{mk}(r)\exp\left[\mathrm{i}\left(m\theta+\frac{2\pi k}{L}z\right)\right], \tag{4.31}$$

r, θ and z component of $\widetilde{N}_{mk}(r)$, respectively, and

$$\mathcal{H}_{mk} = \frac{1}{r^2}\left(\mathcal{D}^2 - m^2\right) - \left(\frac{2\pi k}{L}\right)^2 \tag{4.32}$$

represtnts the Laplace operator in Fourier space. For simplicity we set the right hand of eq.(4.30) as,

$$\widetilde{Y}_{mk} = \frac{Re}{r^2}\left(\mathcal{D}(r\widetilde{F}_{\theta,mk}) - \mathrm{i}m(r\widetilde{F}_{r,mk})\right), \tag{4.33}$$

$$\widetilde{Z}_{mk} = \frac{Re}{r^2}\left(\mathcal{D}^2 - m^2\right)\widetilde{F}_{z,mk} - \frac{Re}{r^2}\frac{2\pi \mathrm{i}k}{L}\left(\mathcal{D}(r\widetilde{F}_{r,mk}) + \mathrm{i}m(r\widetilde{F}_{\theta,mk})\right). \tag{4.34}$$

Using Crank-Nicolson method for viscos terms and second order Adams-Bashforth method for nonliner term, we can obtain

$$\mathcal{H}_{m0}\left(\mathcal{H}_{mk} - \frac{2Re}{\Delta t}\right)\widetilde{\psi}_{mk}^{t+\Delta t} = -\mathcal{H}_{m0}\left(\mathcal{H}_{mk} + \frac{2Re}{\Delta t}\right)\widetilde{\psi}_{mk}^{t} + 3\widetilde{Z}_{mk}^{t} - \widetilde{Y}_{mk}^{t-\Delta t}, \tag{4.35}$$

$$\mathcal{H}_{m0}\left(\mathcal{H}_{mk} - \frac{2Re}{\Delta t}\right)\mathcal{H}_{mk}\widetilde{\phi}_{mk}^{t+\Delta t} = -\mathcal{H}_{m0}\left(\mathcal{H}_{mk} + \frac{2Re}{\Delta t}\right)\mathcal{H}_{mk}\widetilde{\phi}_{mk}^{t} + 3\widetilde{Z}_{mk}^{t} - \widetilde{Z}_{mk}^{t-\Delta t}, \tag{4.36}$$

where Δt represent the interval of time integration. From given $\widetilde{\psi}_{mk}$ and $\widetilde{\phi}_{mk}$ at t and $t - \Delta t$ we can get these function at $t + \Delta t$ under following boundary conditions.

For $m \neq 0$,

$$\widetilde{\phi}_{mk}^{t+\Delta t} = 0 \qquad (\text{at } r = 1), \tag{4.37a}$$

$$\mathcal{D}\widetilde{\psi}_{mk}^{t+\Delta t} = 0 \qquad (\text{at } r = 1), \tag{4.37b}$$

$$\mathcal{D}^2\widetilde{\phi}_{mk}^{t+\Delta t} = 0 \qquad (\text{at } r = 1), \tag{4.37c}$$

$$m\widetilde{\psi}_{mk}^{t+\Delta t} + \frac{2\pi k}{L}\mathcal{D}\widetilde{\phi}_{mk}^{t+\Delta t} = 0 \qquad (\text{at } r = 1), \tag{4.37d}$$

$$\frac{2\pi k}{L}\left[\mathcal{D}^3 - 2\mathcal{D}^2 + 2m^2\right]\widetilde{\psi}_{mk}^{t+\Delta t} - m\left[\mathcal{D}^4 - 4\mathcal{D}^3 + 4m^2\mathcal{D}\right]\widetilde{\phi}_{mk}^{t+\Delta t} = 0 \qquad (\text{at } r = 1). \tag{4.37e}$$

For $m = 0$ and $k \neq 0$,

$$\widetilde{\psi}_{0k}^{t+\Delta t} = 0 \qquad (\text{at } r = 1), \tag{4.38a}$$

$$\mathcal{D}\widetilde{\psi}_{0k}^{t+\Delta t} = 0 \qquad (\text{at } r = 1), \tag{4.38b}$$

$$\widetilde{\phi}_{0k}^{t+\Delta t} = 0 \qquad (\text{at } r = 1), \tag{4.38c}$$

$$\mathcal{D}\widetilde{\phi}_{0k}^{t+\Delta t} = 0 \qquad (\text{at } r = 1), \tag{4.38d}$$

$$\mathcal{D}^2\widetilde{\phi}_{0k}^{t+\Delta t} = 0 \qquad (\text{at } r = 1). \tag{4.38e}$$

For $m = 0$ and $k = 0$,

$$\widetilde{\psi}_{00}^{t+\Delta t} = 0 \qquad (\text{at } r = 1), \tag{4.39a}$$

$$\mathcal{D}\widetilde{\psi}_{00}^{t+\Delta t} = 0 \qquad (\text{at } r = 1), \tag{4.39b}$$

$$\widetilde{\phi}_{00}^{t+\Delta t} = 0 \qquad (\text{at } r = 1), \tag{4.39c}$$

$$\mathcal{D}^2\widetilde{\phi}_{00}^{t+\Delta t} = 0 \qquad (\text{at } r = 1), \tag{4.39d}$$

$$\left[\mathcal{D}^3 - \frac{2R}{\Delta t}\mathcal{D}\right]\widetilde{\phi}_{00}^{t+\Delta t} = -\left[\mathcal{D}^3 + \frac{2R}{\Delta t}\mathcal{D}\right]\widetilde{\phi}_{00}^{t} + 4 \qquad (\text{at } r = 1). \tag{4.39e}$$

where eq.(4.39e) is from eq.(4.14) using Crank-Nicolson method.

From here we present how to solve equation (4.35) and (4.36). Eq.(4.35) is solved with two boundary conditions, $\widetilde{\psi}_{mk}^{t+\Delta t}|_{r=1} = d_0$ and $\mathcal{D}\widetilde{\psi}_{mk}^{t+\Delta t}|_{r=1} = d_1$. Let $\boldsymbol{T}$ be the column vector of coefficients of $\widetilde{\psi}_{mk}^{t+\Delta t}$, $\boldsymbol{Y}$ be those of right hand side of eq.(4.35),

$$\mathcal{L}\boldsymbol{T} = \boldsymbol{Y}, \tag{4.40}$$

where $\mathcal{L}$ represents the matrix form of the operator $H_{m0}(H_{mk} - \frac{2Re}{\Delta t})$. Let the number of components of $\boldsymbol{T}$ or $\boldsymbol{Y}$ be I. We represent the two boundary conditions above as

$$\boldsymbol{c}_0 \cdot \boldsymbol{T} = d_0, \tag{4.41a}$$

$$\boldsymbol{c}_1 \cdot \boldsymbol{T} = d_1. \tag{4.41b}$$

Using a tau method we solve eq.(4.40)-(4.41).

$$\mathcal{L}^{'}\boldsymbol{T} = \boldsymbol{Y}^{'} \tag{4.42}$$

$$\mathcal{L}^{'}_{ij} = \begin{cases} \mathcal{L}_{ij} & (1 \le i \le I-2) \\ c_{0j} & (i = I-1) \\ c_{1j} & (i = I) \end{cases} \tag{4.43}$$

$$Y^{'}_{i} = \begin{cases} Y_i & (1 \le i \le I-2) \\ s_0 & (i = I-1) \\ s_1 & (i = I) \end{cases} \tag{4.44}$$

For eq.(4.36), Let $\boldsymbol{P}$ be the column vector of coefficients of $\widetilde{\phi}_{mk}^{t+\Delta t}$, $\boldsymbol{Z}$ be those of right hand side of eq.(4.36), the form to solve become

$$\mathcal{L}_2\mathcal{L}_1\boldsymbol{P} = \boldsymbol{Z}, \tag{4.45}$$

where $\mathcal{L}_1$ is $\mathcal{L}$, and $\mathcal{L}_2$ represents the operator H_{mk}. The three boundary conditions is represented as

$$\boldsymbol{c}_0 \cdot \boldsymbol{P} = e_0, \tag{4.46a}$$

$$\boldsymbol{c}_1 \cdot \boldsymbol{P} = e_1, \tag{4.46b}$$

$$\boldsymbol{c}_2 \cdot \boldsymbol{P} = e_2. \tag{4.46c}$$

We solve eq.(4.45)-(4.46) by folling steps. At first we seek the homogeneous solution of eq.(4.45). Next equations are solved by τ method with given boundary conditions:

$$\mathcal{L}_2 \boldsymbol{P}' = 0 \quad (\boldsymbol{c}_0 \cdot \boldsymbol{P}' = 1), \tag{4.47}$$

$$\mathcal{L}_1 \boldsymbol{P}^{\mathrm{h}} = \boldsymbol{P}' \quad (\boldsymbol{c}_0 \cdot \boldsymbol{P}^{\mathrm{h}} = \boldsymbol{c}_1 \cdot \boldsymbol{P}^{\mathrm{h}} = 0). \tag{4.48}$$

Then we seek also the particular solution of eq.(4.45).

$$\mathcal{L}_2 \boldsymbol{P}'' = \boldsymbol{Z} \quad (\boldsymbol{c}_0 \cdot \boldsymbol{P}'' = 0), \tag{4.49}$$

$$\mathcal{L}_1 \boldsymbol{P}^{\mathrm{p}} = \boldsymbol{P}'' \quad (\boldsymbol{c}_0 \cdot \boldsymbol{P}^{\mathrm{p}} = e_0, \boldsymbol{c}_1 \cdot \boldsymbol{P}^{\mathrm{p}} = e_1). \tag{4.50}$$

Using $\boldsymbol{P}^{\mathrm{h}}$ and $\boldsymbol{P}^{\mathrm{p}}$, we can seek the solution which satisfy the boundary conditions (4.46a)-(4.46c):

$$\boldsymbol{P} = \frac{e_2 - \boldsymbol{c}_2 \cdot \boldsymbol{P}^{\mathrm{p}}}{\boldsymbol{c}_2 \cdot \boldsymbol{P}^{\mathrm{h}}} \boldsymbol{P}^{\mathrm{h}} + \boldsymbol{P}^{\mathrm{p}}. \tag{4.51}$$

Now we see how to solve equation (4.35) and (4.36) with the boundary conditions (4.41) and (4.46). Next we present how to solve those in the cases of boundary conditions (4.37) and (4.39). In the case of (4.37), we seek the homogeneous solution for the toroidal function with the following boundary conditions

$$\mathcal{L}_1 \boldsymbol{T}^{\mathrm{h}} = 0, \tag{4.52a}$$

$$\boldsymbol{c}_0 \cdot \boldsymbol{T}^{\mathrm{h}} = 1, \tag{4.52b}$$

$$\boldsymbol{c}_1 \cdot \boldsymbol{T}^{\mathrm{h}} = 0, \tag{4.52c}$$

and the specific solution with the following boundary conditions

$$\mathcal{L}_1 \boldsymbol{T}^{\mathrm{p}} = \boldsymbol{Y}, \tag{4.53a}$$

$$\boldsymbol{c}_0 \cdot \boldsymbol{T}^{\mathrm{p}} = 0, \tag{4.53b}$$

$$\boldsymbol{c}_1 \cdot \boldsymbol{T}^{\mathrm{p}} = 0. \tag{4.53c}$$

Then we set the general solution

$$\boldsymbol{T} = \boldsymbol{T}^{\mathrm{p}} + a\boldsymbol{T}^{\mathrm{h}}, \tag{4.54}$$

where a is undecided number. For the poloidal function, we construct similarly the general solution by the following solutions:

$$\mathcal{L}_2 \mathcal{L}_1 \boldsymbol{P}^{\mathrm{h}} = 0, \tag{4.55a}$$

$$\boldsymbol{c}_0 \cdot \boldsymbol{P}^{\mathrm{h}} = 0, \tag{4.55b}$$

$$\boldsymbol{c}_1 \cdot \boldsymbol{P}^{\mathrm{h}} = 1, \tag{4.55c}$$

$$\boldsymbol{c}_2 \cdot \boldsymbol{P}^{\mathrm{h}} = 0, \tag{4.55d}$$

$$\mathcal{L}_2 \mathcal{L}_1 \boldsymbol{P}^{\mathrm{p}} = \boldsymbol{Z}, \tag{4.56a}$$

$$\boldsymbol{c}_0 \cdot \boldsymbol{P}^{\mathrm{p}} = 0, \tag{4.56b}$$

$$\boldsymbol{c}_1 \cdot \boldsymbol{P}^{\mathrm{p}} = 0, \tag{4.56c}$$

$$\boldsymbol{c}_2 \cdot \boldsymbol{P}^{\mathrm{p}} = 0. \tag{4.56d}$$

Then we set the general solution

$$\boldsymbol{P} = \boldsymbol{P}^{\mathrm{p}} + b\boldsymbol{P}^{\mathrm{h}}, \tag{4.57}$$

where b is undecided number. Substituting eq.(4.54) and (4.57) to (4.37d) and (4.37e), a and b are decided as

$$a = (2\pi k/L)\frac{m\left(\boldsymbol{c}_4 \cdot \boldsymbol{P}^{\mathrm{p}} - 4\boldsymbol{c}_3 \cdot \boldsymbol{P}^{\mathrm{p}}\right) - (2\pi k/L)\left(\boldsymbol{c}_3 \cdot \boldsymbol{T}^{\mathrm{p}} - 2\boldsymbol{c}_2 \cdot \boldsymbol{T}^{\mathrm{p}}\right)}{a^2\left(\boldsymbol{c}_4 \cdot \boldsymbol{P}^{\mathrm{h}} - 4\boldsymbol{c}_3 \cdot \boldsymbol{P}^{\mathrm{h}} + 4m^2\right) + (2\pi k/L)^2\left(\boldsymbol{c}_3 \cdot \boldsymbol{T}^{\mathrm{h}} - 2\boldsymbol{c}_2 \cdot \boldsymbol{T}^{\mathrm{h}} + 2m^2\right)}, \tag{4.58}$$

$$b = -a\frac{m\left(\boldsymbol{c}_4 \cdot \boldsymbol{P}^{\mathrm{p}} - 4\boldsymbol{c}_3 \cdot \boldsymbol{P}^{\mathrm{p}}\right) - (2\pi k/L)\left(\boldsymbol{c}_3 \cdot \boldsymbol{T}^{\mathrm{p}} - 2\boldsymbol{c}_2 \cdot \boldsymbol{T}^{\mathrm{p}}\right)}{a^2\left(\boldsymbol{c}_4 \cdot \boldsymbol{P}^{\mathrm{h}} - 4\boldsymbol{c}_3 \cdot \boldsymbol{P}^{\mathrm{h}} + 4m^2\right) + (2\pi k/L)^2\left(\boldsymbol{c}_3 \cdot \boldsymbol{T}^{\mathrm{h}} - 2\boldsymbol{c}_2 \cdot \boldsymbol{T}^{\mathrm{h}} + 2m^2\right)}, \tag{4.59}$$

where $\boldsymbol{c}_3$ and $\boldsymbol{c}_4$ are the vectors which represent the operator $\mathcal{D}^3$ and $\mathcal{D}^4$ at $r = 1$. In the case of (4.39), the toroidal function is solved by preceeiding τ method and the poloidal function is solved as following. As well as in the case of (4.37), we set the solution as

$$\boldsymbol{P} = \boldsymbol{P}^{\mathrm{p}} + c\boldsymbol{P}^{\mathrm{h}}, \tag{4.60}$$

where $\boldsymbol{P}^{\mathrm{h}}$ and $\boldsymbol{P}^{\mathrm{p}}$ are the same avobe, and c is undecided number. Substituting eq.(4.60) to (4.39e), c is decided as

$$c = \frac{2Re\boldsymbol{c}_1 \cdot \boldsymbol{P}^t + \Delta t(\boldsymbol{c}_3 \cdot \boldsymbol{P}^{\mathrm{p}} + \boldsymbol{c}_3 \cdot \boldsymbol{P}^t - 4)}{2Re - \Delta t\boldsymbol{c}_3 \cdot \boldsymbol{P}^{\mathrm{h}}}, \tag{4.61}$$

where $\boldsymbol{P}^t$ represents the coefficients of $\widetilde{\phi}^t_{00}$.

Bibliography

[Azuma and Araga (2001)] Azuma, K. and Araga, T., 2001, Generation and growth of puff and slug in initial stage of a transitional pipe flow, Trans. Jpn. Soc. Mech. Eng. B, **67**, 117-125.

[Bandyopadhyay (1986)] Bandyopadhyay, P.R., 1986, Aspects of the equilibrium puff in transitional pipe flow, J. Fluid Mech., **163**, 439-458.

[Betchov and Szewczyk (1963)] Betchov, R. and Szewczyk, A., 1963, Stability of a shear layer between parallel streams, Phys. Fluids, **6**, 1391-1396.

[Bhatia and Born (1954)] Bhatia, A. B. and Born, M., 1954, On the circle polynomials of Zernike and related orthogonal sets, in Proc. Cambridge Phil. Soc., **50**, 40-53.

[Darbyshire and Mullin (1995)] Darbyshire, A.G. and Mullin, T., 1995, Transition to turbulence in constant-mass-flux pipe flow, J. Fluid Mech., **289**, 83-114.

[Eggels *et al.* (1994)] Eggels, J. G. M., Unger, F., Weiss, M. H., Westerweel, J., Adrian, R. J., Friedrich, R., and Nieuwstadt, F. T. M., 1994, Fully developed turbulent pipe flow: a comparison between direct numerical simulation and experiment, J. Fluid Mech., **268**, 175-209.

[Faisst and Eckhardt (2003)] Faisst, H. and Eckhardt, B., 2003, Travelling waves in pipe flow, Phys. Rev. Lett., **91**, 224502.

[Faisst and Eckhardt (2004)] Faisst, H. and Eckhardt, B., 2004, Sensitive dependence on initial conditions in transition to turbulence in pipe flow, J. Fluid Mech., **504**, 343-352.

[Hof *et al.* (2006)] Hof, B., Westerweel, J., Schneider, T. M., and Eckhardt, B., 2006, Finite lifetime of turbulence in shear flows, Nature, **443**, 59-62.

[Hamilton *et al.* (1995)] Hamilton, J. M., Kim, J. and Waleffe, F, 1995, Regeneration mechanisms of near-wall turbulence structures, J. Fluid Mech., **287**, 317-348.

[Joseph and Carmi (1969)] Joseph, D. D. and Carmi, S., 1969, Stability of poiseuille flow in pipes annuli and channels, Q. Appl. Math., **26**, 575-599.

[Kawahara and Kida (2001)] Kawahara, G. and Kida, S., 2001, Periodic motion embedded in plane Couette turbulence: regeneration cycle and burst, J. Fluid Mech., **449**, 291-300.

[Kerswell (2005)] Kerswell, R. R., 2005. Recent progress in understanding the transition to turbulence in a pipe, Nonlinearity, **18**, R17-R44.

[Kim and Hussain(1993)] Kim, J. and Hussain, F., 1993, Propagation velocity of perturbations in turbulent channel flow, Phys. Fluids, **A5**, 695-706.

[Marqués (1990)] Marqués, M., 1990, On boundary conditions for velocity scalars in confined flows: application to Couette flow, Phys. Fluids A, **2**, 729-737.

[Matsushima and Marcus (1995)] Matsushima, T. and Marcus, P. S., 1995, A spectral method for polar coordinates, J. Comp. Phys., **120**, 365-374.

[Nagata (1997)] Nagata, M., 1997, Three-dimensional traveling-wave solutions in plane Couette flow, Phys. Rev. E, **55**, 2023-2025

[Nikitin (1994)] Nikitin, N. V., 1994, Direct numerical modeling of three-dimensional turbulent flows in pipes of circular cross section, Fluid Dyn., **29**, 749-758

[O 'Sullivan and Breuer (1994)] O 'Sullivan, P. L. and Breuer, K. S., 1994, Transient growth in circular pipe flow. I. Linear disturbances, Phys. Fluids, **6**, 3643-3664

[Pfenninger (1961)] Pfenninger, W., 1961. Transition in the inlet length of tubes at high Reynolds numbers. In Boundary Layer and Flow Control (ed. G.V. Lachman), pp.970-980, Pergamon.

[Priymak and Miyazaki (1994)] Priymak, V.G. and Miyazaki, T., 1994, Long-wave motions in turbulent shear flows, Phys. Fluids, **6**, 3454-3464.

[Priymak and Miyazaki (2004)] Priymak, V. G. and Miyazaki, T., 2004, Direct numerical simulation of equilibrium spatially localized structures in pipe flow, Phys. Fluids, **16**, 4221-4234.

[Reuter and Rempfer (2004)] Reuter, J. and Rempfer, D., 2004, Analysis of pipe flow transition. Part 1. Direct numerical simulation, Theor. Comput.Fluid Dyn., **17**, 273-292

[Reynolds (1883)] Reynolds, O., 1883, An experimental investigation of the circumstances which determine whether the motion of the water shall be direct or sinuous, and of the law of resistance in parallel channels, Phil. Trans. R. Soc. Lond., **A 174**, 935-982.

[Rubin *et al.* (1980)] Rubin, Y., Wygnanski, I. J. and Haritonidis, J. H., 1980, Further observations on transition in a pipe, Proc. IUTAM Symp. on Laminar-Turbulent Transition (Stuttgart, FRG 1979), 17-26.

[Salwen *et al.* (1980)] Salwen, H., Cotton, F.W. and Grosch, C.E., 1980, Linear stability of Poiseuille flow in a circular pipe, J. Fluid Mech., **98**, 273-284.

[Shan *et al.* (1999)] Shan, H., Ma, B., Zhang, Z. and Nieuwstadt, F. T .M,. 1999, Direct numerical simulation of a puff and a slug in transitional cylindrical pipe flow, J. Fluid Mech., **387**, 39-60.

[Shimizu and Kida (2008)] Shimizu, M. and Kida, S., 2008, Structure of a turbulent puff in pipe flow, J. Phys. Soc. Jpn., **77**, 114401.

[Tatsumi (1952)] Tatsumi, T., 1952, Stability of the laminar inlet-flow prior to the formation of poiseuille regime 2., J. Phys. Soc. Japan, **7**, 495-502.

[Verkley (1997)] Verkley,W. T. M., 1997, A Spectral model in two-dimensional incompressible fluid flow in a circular basin, J. Comp. Phys., **136**, 100-114.

[Viswanath(2007)] Viswanath, D., 2007, Recurrent motions within plane Couette turbulence, J. Fluid Mech., **580**, 339-358.

[Waleffe (1997)] Waleffe, F., 1997, On a self-sustaining process in shear flows. Phys. Fluids, **9**, 883-900.

[Wedin and Kerswell (2004)] Wedin, H. and Kerswell, R. R., 2004, Exact coherent structures in pipe flow: travelling wave solutions, J. Fluid Mech., **508**, 333-371.

[Willis and Kerswell (2007)] Willis, A. P. and Kerswell, R. R., 2007, Critical behavior in the relaminalization of localized turbulence in pipe flow, Phys. Rev. Lett., **98**, 014501.

[Willis and Kerswell (2007)] Willis, A. P. and Kerswell, R. R., 2008, Coherent structures in localised and global pipe turbulence, Phys. Rev. Lett., **100**, 124501

[Wygnanski and Champagne (1973)] Wygnanski, I. J. and Champagne, F. H., 1973, On transition in a pipe. Part 1. The origin of puffs and slugs and the flow in a turbulent slug, J. Fluid Mech., **59**, 281-335.

[Wygnanski *et al.* (1975)] Wygnanski, I. J., Sokolov, M. and Friedman, D., 1975, On transition in a pipe. Part 2. The equilibrium puff, J. Fluid Mech., **69**, 283-304.

Acknowledgements

This doctoral thesis is the summary of my studies with professor S. Kida at Kida laboratory, Graduate School of Engineering, Kyoto University. The author most grateful to him for his coach. The author would like to express their cordial gratitude to Professor M. Nishioka and Dr. S. Goto for fruitful discussions during the present study and M. Nagata and R. Inamuro, who are examiners of this thesis, for their useful comments and corrections.

Masaki Shimizu
February, 2009